University of Nevada, Reno

Theoretical studies at the interface of atomic physics and precision measurements

A dissertation submitted in partial fulfillment of the requirements for the degree of Doctor of Philosophy in Physics

by

Di Xiao

Dr.Andrei Derevianko/Dissertation Advisor

May, 2023

THE GRADUATE SCHOOL

We recommend that the dissertation
prepared under our supervision by

Di Xiao

entitled

Theoretical studies at the interface of atomic physics and precision measurements

be accepted in partial fulfillment of the
requirements for the degree of

Doctor of Philosophy

Andrei Derevianko, Ph.D.
Advisor

Jonathan D. Weinstein, Ph.D.
Committee Member

Timur Tscherbul, Ph.D.
Committee Member

Joshua Williams, Ph.D.
Committee Member

Sergey A. Varganov, Ph.D.
Graduate School Representative

Markus Kemmelmeier, Ph.D., Dean
Graduate School

May, 2023

Abstract

Hyperfine structure (HFS) of atomic energy levels arises due to interactions of atomic electrons with a hierarchy of nuclear multipole moments, including magnetic dipole, electric quadrupole, and higher-rank moments. Recently, a determination of the magnetic octupole moment of the ^{173}Yb nucleus was reported from HFS measurements in neutral ^{173}Yb [PRA 87, 012512 (2013)], and is four orders of magnitude larger than the nuclear theory prediction. Considering this substantial discrepancy between the spectroscopically extracted value and nuclear theory, here we propose to use an alternative system to resolve this tension, a singly charged ion of the same ^{173}Yb isotope. Utilizing the substantial suite of tools developed around Yb^+ for quantum information applications, we propose to extract nuclear octupole and hexadecapole moments from measuring hyperfine splittings in the extremely long-lived first excited state ($4f^{13}(^2F^o)6s^2$, $J = 7/2$) of $^{173}Yb^+$. We present the results of atomic structure calculations in support of the proposed measurements.

The next study investigates the hyperfine-induced effects in a series of experiments related to atomic parity violation (APV). The Stark interference technique, used in APV experiments, requires accurate knowledge of transition polarizability. In Cesium, the $6S_{1/2} \rightarrow 7S_{1/2}$ APV amplitude, $\mathrm{Im}(\mathrm{E_{PNC}})$

is deduced from the measured ratio $\mathrm{Im}(\mathrm{E_{PNC}})/\beta$ of the APV amplitude to the vector transition polarizability, β. The ratio was measured with a 0.35% accuracy by the Boulder group [Science **275**, 1759 (1997)]. Currently, there is tension in different determinations of β. The most recent value [Phys. Rev. Lett. **123**, 073002 (2019)] of β, $27.139\,(42)\ a_0^3$ was deduced from the semi-empirical determination of the scalar transition polarizability α and the measured ratio between the scalar and vector polarizability α/β . This value, however, differs by $\sim 0.7\%$ from a previous determination of β [Phys. Rev. A. **62**, 052101 (2000)] based on the measured ratio of magnetic-dipole $6S_{1/2} \rightarrow 7S_{1/2}$ matrix element to β. Here, we recompute the E1-dipole matrix elements associated with $\alpha^{[2]}$ using the state-of-art coupled-cluster technique and $\alpha^{[2]}$ evaluates to $-262.26\,(48)\,a_0^3$. The resulting determination for β is $27.083\,(57)\,a_0^3$ based on the reported ratio α/β of 9.905(11) [Phys. Rev. A. **55**, 2 (1997)]. We also quantitatively evaluate the effect of additional third-order hyperfine-induced corrections to the $6S_{1/2} \rightarrow 7S_{1/2}$ transition polarizability. We show that a new "tensor" contribution to transition polarizability appears in the analysis and investigate nuclear spin-dependent-polarizability effects on the nuclear anapole moment and the ratio between the scalar and vector polarizabilities.

Acknowledgment

The work on $^{173}Yb^{+}$ computations was supported in part by the U.S. National Science Foundation (Award Numbers 1912555 and 1912465). The work on polarizabilities was supported in part by the U.S. National Science Foundation grants PHY-1912465 and PHY-2207546, by the Sara Louise Hartman endowed professorship in Physics, and by the Center for Fundamental Physics at Northwestern University.

Table of Contents

List of Tables

List of Figures

Preface

Much of the content of this dissertation was published in the following scientific journal articles:

Hyperfine structure of $^{173}Yb^{+}$: Toward resolving the ^{173}Yb nuclear-octupole-moment puzzle. Di Xiao, Jiguang Li, Wesley C.Campbell, Thomas Dellaert, Patrick McMillin, Anthony Ransford, Conrad Roman, and Andrei Derevianko, Phys. Rev. A. **102**, 022810 (2020)

Hyperfine corrections to the Stark-induced transition polarizability in Cesium and their implications for atomic parity violation. Di Xiao, H. B. Tran Tan, and Andrei Derevianko, to be published.

I have also published the following papers during my Ph.D. studies:

Parity-mixed coupled-cluster formalism for computing parity-violating amplitudes. H. B. Tran Tan, Di Xiao, and A. Derevianko Phys. Rev. A. **105**, 022803 (2022)

Shaped nozzles for cryogenic buffer-gas beam sources. Di Xiao, David M. Lancaster, Cameron H. Allen, Mckenzie J. Taylor, Thomas A. Lancaster, Gage Shaw, Nicholas R. Hutzler, and Jonathan D. Weinstein. Phys. Rev. A. **99**, 013603 (2019)

Electrostatic guiding of the methylidyne radical at cryogenic temperatures.

David M. Lancaster, Cameron H. Allen, Kylan Jersey, Thomas A. Lancaster, Gage Shaw, Mckenzie J. Taylor, Di Xiao, and Jonathan D. Weinstein. The European Physical Journal D volume 74, 132 (2020) sections/Preface

Chapter 1

Introduction

The intersection of atomic physics and precision measurements plays a crucial role in testing fundamental physics. Advanced computational techniques such as the multiconfiguration Hartree-Fock (MCHF) approach, coupled-cluster (CC) method, and B-spline approach with random-phase and Bruckner-order corrections, along with high-performance computing tools, enable atomic-structure calculations to obtain theoretical results in a reasonable timeframe. These theoretical computations not only aid in predicting measurements but also help identify possible systematic errors that may exist in experiments. In this dissertation, we review the hyperfine interaction and propose measurements of hyperfine splitting in $^{173}Yb^{+}$ to address a discrepancy observed [12] in the magnetic octupole moment measurement in ^{173}Yb compared to nuclear theory. To achieve this goal, the use of singly charged $^{173}Yb^{+}$ ions is suggested to extract nuclear octupole and hexadecapole moments from hyperfine splittings in the $J = 7/2$ state. Chapter 2 provides a comprehensive review of atomic parity violation (APV) and its correlation with transition polarizabili-

ties. Theoretical groundwork for hyperfine-induced transition polarizability is formally established, followed by a discussion on its impact on APV measurements.

Chapter 2

Computations on hyperfine splittings and the nuclear octupole moment in Yb^+

2.1 Introduction

The size of an atomic nucleus is too small to be observed directly with a microscope. However, when electrons are bound to an atomic nucleus, they leave hyperfine structures (HFS) that indicate the size and shape of the nucleus on the resulting atom. In particular, P and T symmetries dictate that the distribution of protons leads to even-rank ($k = 0, 2, 4...$) electric 2^k-pole moments (e.g., monopole, quadrupole, and hexadecapole) and the distribution of currents and magnetic moments leads to odd-rank ($k = 1, 3, 5...$) magnetic moments (e.g. dipole, octupole, and 32-pole) that interact with the electrons to shift their energies. This enables a measurement of the HFS of an atom,

when combined with accurate atomic structure calculations, to be used as an electron scattering experiment on the nucleus that allows us to observe how well-characterized electrons scatter from the nucleus and see how its nucleons are distributed.

It has been observed that (nuclear) magnetic dipoles and electric quadrupoles contribute the most to HFS. In compilation [2], the nuclear magnetic dipole (μ) and electric quadrupole (Q) moments of most nuclei are well-established mainly because the HFS signatures of higher-order moments only appear on states with sufficiently high multiplicity ($2J \geq k$), and the magnitude of the energy shift decreases with rank k. Therefore, to measure the HFS signature of multipoles with high rank ($k \geq 3$), a well-controlled atom in a high angular momentum state and state-of-the-art atomic structure theory are needed.

Here, we focus on the potential for measuring the rarely observed nuclear octupole ($\Omega, k=3$) and hexadecapole ($\Pi, k=4$) moments. These moments have been deduced for only a handful of nuclei and, in most cases, are in tension with nuclear theory (see Table 2.1). For example, in ^{133}Cs, the extracted [13] nuclear octupole moment is 40 times larger that the nuclear theory value. This paper is motivated by the even more substantial disagreement for ^{173}Yb. Recently, Singh et al. [12] reported a measurement of the nuclear octupole moment from their measurements of HFS in the $^3P_2$ state of neutral ^{173}Yb. However, this value $\Omega = -34.4\,\mathrm{b}\mu_\mathrm{N}$ is 10^4 times larger than the nuclear theory prediction, $\Omega = 0.003\,\mathrm{b}\mu_\mathrm{N}$ [14]. This striking four orders of magnitude-disagreement calls for independent measurement and analysis. Here, we investigate the prospects for extracting Ω and higher rank nuclear multipole moments of ytterbium-173 by a combined theoretical and experimental investigation of the hyperfine level

splittings in the first excited state ($4f^{13}(^2F^o)6s^2$, $J = 7/2$) of the $^{173}Yb^+$ ion. This $^2F^o_{7/2}$ state is metastable, contains six $m_F = 0$ states that will be first-order insensitive to magnetic fields and easily state-selectively coupled to the ground state for precision spectroscopy.

Table 2.1: Compilation of spectroscopic determinations of nuclear octupole moments. $\Omega^{\rm emp}$ are the empirical moments derived from the combination of spectroscopic HFS measurements and electronic structure calculations. $\Omega^{\rm SP}$ are octupole moments predicted by the single-particle model [1]. All octupole moments are in units barn $\times$ nuclear magneton(b $\times$ $\mu_{\rm N}$). All listed isotopes are stable except for ^{115}In and ^{87}Rb with half-lives of 4.4×10^{14} and 4×10^{10} years, respectively [2]. Values of Ω have also been reported for about 20 additional nuclei from nuclear scattering experiments [3].

Isotope	I^π	Valence nucleon	Atomic state	$\Omega^{\rm emp}$	$\Omega^{\rm SP}$
^{87}Rb [15]	$\frac{3}{2}^-$	$p_{3/2}$, proton	$^2P_{3/2}$	-0.58	0.30
^{113}In [16]	$\frac{9}{2}^+$	$g_{9/2}$, proton	$^2P_{3/2}$	0.574	0.99
^{115}In [16]	$\frac{9}{2}^+$	$g_{9/2}$, proton	$^2P_{3/2}$	0.565	1.00
^{133}Cs [13]	$\frac{7}{2}^+$	$g_{7/2}$, proton	$^2P_{3/2}$	0.82	0.022
$^{137}Ba^+$ [17]	$\frac{3}{2}^+$	$d_{3/2}$, neutron	$^2D_{3/2}$	-0.0629	0.039
^{155}Gd [18]	$\frac{3}{2}^-$	$p_{3/2}$, neutron	$^9D_3$	-1.66	-0.29
^{165}Ho [19]	$\frac{7}{2}^-$	$f_{7/2}$, proton	$^4I_{15/2}$	0.75	1.0
^{173}Yb [12]	$\frac{5}{2}^-$	$f_{5/2}$, neutron	$^3P_2$	-34.4	0.15

Most of the previous spectroscopic determinations of high-order moments of nuclei focused on the extraction of octupole moments, and are compiled in Table 2.1. This Table also lists the nuclear single-particle model [1] values for the nuclear octupole moments. In addition to the listed spectroscopic determinations, the experiments were carried out in Eu [20] and Hf [21]. However, due to the complexity of electronic structure calculations, these experiments only determined ratios of nuclear octupole moments between different isotopes, $\Omega(^{151}\text{Eu})/\Omega(^{153}\text{Eu})$ and $\Omega(^{177}\text{Hf})/\Omega(^{179}\text{Hf})$.

Beyond octupole order, the hexadecapole moment Π has been spectroscopically determined for only one species: ^{165}Ho [19]. Access to the hexadecapole moments requires $J \geq 2$ and $I \geq 2$. For example, although ^{133}Cs nucleus has $I = 7/2$ and thereby possesses hexadecapole moment, this moment can not be determined from the measured HFS of the $6\,p_{3/2}$ state [13]. This argument prohibits the extraction of nuclear hexadecapole moments from the structure of the states used to measure magnetic octupole moments for all but two exceptions in Table 2.1: ^{165}Ho and ^{173}Yb. The value for Π that was extracted from spectroscopic measurements in ^{165}Ho was found to be larger than the nuclear theory value by an order of magnitude [19]. In principle, one could extract Π from the measurements made by Singh *et al.* in neutral ^{173}Yb [12], but its contribution was neglected in that work. Here, in order to leverage the considerable experimental toolbox built around Yb^+ for quantum information applications, we evaluate the necessary electronic structure factors for $^{173}Yb^+$ needed to enable extraction of the hexadecapole moment of this isotope from future spectroscopic measurements.

The Yb^+ ground state hyperfine structure is among the most precisely measured and easiest to control of all the HFS in atomic physics owing to its $m_F = 0$ "clock states" and its readily available state preparation and readout schemes. The $^2S_{1/2}$ HFS of $^{171}Yb^+$ has been used for decades for frequency standards and quantum information processors and its splitting has been known to mHz precision for many years [22]. The long coherence time of clock-state qubits defined on this hyperfine splitting (recently shown to exceed 10 minutes [23]) has made $^{171}Yb^+$ a premier qubit host for quantum computing and quantum simulation [24–28]. Likewise, the metastable $^2F^o_{7/2}$ electronic

state of $^{171}Yb^+$ lives for years, and the E3 transition on $^2S_{1/2} \leftrightarrow {}^2F^o_{7/2}$ is used as an optical frequency standard [29], where hyperfine structure within these states allows control of systematics. Some of the current best limits on the time variation of fundamental constants are based on precision measurements between specific hyperfine components of this E3 transition [30, 31].

As the experimental progress with this species continues to achieve higher accuracy and precision [29, 32], theoretical work is needed in parallel with these improvements to understand contributions to systematics. Ref. [33] has shown how to calculate the second-order energy correction due to hyperfine interaction for the alkali-atoms in the first excited state, and gives the theoretical basis for higher-order terms calculated in this paper. The values of hyperfine constants A and B for $^{171}Yb^+$ and $^{173}Yb^+$ in the $^2F^o_{7/2}$ state are also given in Ref. [34], and are used as a comparison to our values.

The chapter is organized as follows. In Sec. 2.2, we review the theory of hyperfine structure. Based on this general theory, we derive the first- and second-order corrections to the HFS of $^{173}Yb^+$ in the first excited state. In Sec. 2.4.1, we compute $^{173}Yb^+$ electronic-structure factors required for extracting nuclear moments. Finally, we estimate theoretical accuracy and consider its implications on the extraction of octupole and hexadecapole moments in Sec. 2.5. Unless specified otherwise, atomic units are used throughout.

2.2 Review of the theory of hyperfine structure

The hyperfine interaction can be decomposed into the magnetic dipole (M1), electric quadrupole (E2), magnetic octupole (M3), electric hexadecapole (E4), and higher rank contributions. We start by expressing the hyperfine Hamiltonian in irreducible tensor form [1, 35]

$$H_{\rm HFI} = \sum_{k,\mu} (-1)^{\mu} T^e_{k,\mu} T^n_{k,-\mu}\,, \tag{2.1}$$

where rank-k tensors $T^e_{k,\mu}$ act in the electron space, and $T^n_{k,-\mu}$ — in the nuclear space. The many-electron operators are $T^e_{k,\mu} = \sum\limits_i t^e_{k,\mu}(i)$, where the summation is over all the atomic electrons. The single-electron operators $t^e_{k,\mu}(i)$ can be divided into two groups [35],

$$t^e_{k,\mu}(i) = \begin{cases} -\frac{1}{r^{k+1}} C_{k,\mu}(\hat{r}), & \text{electric (even } k)\,, \\ -\frac{i}{r^{k+1}} \sqrt{\frac{k+1}{k}}\, \boldsymbol{\alpha}\cdot \boldsymbol{C}^{(0)}_{k,\mu}(\hat{r}), & \text{magnetic (odd } k). \end{cases} \tag{2.2}$$

Here, $\boldsymbol{\alpha}$ is the Dirac matrix, r is the radial coordinate, $C_{k,\mu}$ are normalized spherical harmonics, and $\boldsymbol{C}^{(0)}_{k,\mu}$ are normalized vector spherical harmonics.

The first-order energy correction due to hyperfine interaction, Eq. (3.44),

in the basis of coupled nuclear and atomic states is [33]

$$W_F^{(1)} = \langle \gamma I J F M_F | H_{\rm HFI} | \gamma I J F M_F \rangle = (-1)^{I+J+F} \times \sum_k \begin{Bmatrix} F & J & I \\ k & I & J \end{Bmatrix} \langle \gamma J || T_k^e || \gamma J \rangle \langle I || T_k^n || I \rangle \,, \tag{2.3}$$

where I is the nuclear spin, J is the total electronic angular momentum, F is the grand total angular momentum $\boldsymbol{F} = \boldsymbol{J} + \boldsymbol{I}$, and γ stands for remaining quantum numbers.

The first-order energy corrections are conventionally expressed as linear combinations of HFS constants A, B, C, D...(k=1,2,3,4...). The first four constants are defined as [33]

$$\begin{aligned} A &= \frac{1}{IJ} \langle T_1^n \rangle_I \langle T_1^e \rangle_J = \frac{1}{IJ} \mu \langle T_1^e \rangle_J \,, \\ B &= 4 \langle T_2^n \rangle_I \langle T_2^e \rangle_J = 2Q \langle T_2^e \rangle_J \,, \\ C &= \langle T_3^n \rangle_I \langle T_3^e \rangle_J = -\Omega \langle T_3^e \rangle_J \,, \\ D &= \langle T_4^n \rangle_I \langle T_4^e \rangle_J = \Pi \langle T_4^e \rangle_J \,. \end{aligned} \tag{2.4}$$

Here, the stretched matrix element $\langle T_k^e \rangle_J$ is defined as

$$\langle T_k^e \rangle_J = \begin{pmatrix} J & k & J \\ -J & 0 & J \end{pmatrix} \langle \gamma J || T_k^e || \gamma J \rangle \tag{2.5}$$

Nuclear stretched matrix elements are proportional to the nuclear moments: $\langle T_1^n \rangle_I = \mu$, $\langle T_2^n \rangle_I = Q/2$, $\langle T_3^n \rangle_I = -\Omega$, and $\langle T_4^n \rangle_I = \Pi$.

The second-order energy correction due to hyperfine interaction reads

$$W_F^{(2)} = \sum_{\gamma' J'} \frac{\langle \gamma I J F M_F | H_{\rm HFI} | \gamma' I J' F M_F \rangle \langle \gamma' I J' F M_F | H_{\rm HFI} | \gamma I J F M_F \rangle}{E_{\gamma J} - E_{\gamma' J'}}. \quad (2.6)$$

This equation reduces to

$$W_F^{(2)} = \sum_{\gamma' J'} \frac{1}{E_{\gamma J} - E_{\gamma' J'}} \sum_{k_1, k2} \begin{Bmatrix} I & J & F \\ J' & I & k_1 \end{Bmatrix} \begin{Bmatrix} I & J & F \\ J' & I & k_2 \end{Bmatrix} \times \quad (2.7)$$
$$\langle I || T^n_{k_1} || I \rangle \langle I || T^n_{k_2} || I \rangle \langle \gamma J || T^e_{k_1} || \gamma' J' \rangle \langle \gamma J || T^e_{k_2} || \gamma' J' \rangle,$$

where primed quantities refer to intermediate states; $E_{\gamma J}$ and $E_{\gamma' J'}$ are the HFI-unperturbed energy levels.

Based on the general theory, in the next section we investigate the hyperfine structure of $^{173}\mathrm{Yb}^+$ in the first excited state.

2.3 Hyperfine structure of Yb^+ in the first excited state

The first excited state of Yb^+ has the electronic configuration $4f^{13}(^2F^o)6s^2$ with electronic angular momentum J equal to 7/2. Since ^{173}Yb has nuclear spin of 5/2, the grand total angular momentum F is an integer in the interval $[1, 6]$. The ^{173}Yb isotope possesses five distinct nuclear electromagnetic moments. The nucleus has an unpaired valence neutron in the $f_{5/2}$ state. The observed [2] nuclear magnetic dipole μ and electric quadrupole moments Q are equal to $-0.680\,\mu_{\rm N}$ and $2.80\,\mathrm{b}^2$, respectively. The nuclear single-particle

shell model is not adequate for this isotope as it predicts zero value for the quadrupole moment (the valence nucleon is a neutron for this isotope, whereas the electric moments arise from the distribution of protons in the core). This discrepancy points to a strong nuclear deformation of ^{173}Yb. Following the theoretical proposal [36], the value for the octupole moment was deduced [12] from the HFS in neutral ^{173}Yb atom in the metastable $6s6p\,^3P_2$ state. However, the deduced value, $\Omega = -34.4\,\mathrm{b} \times \mu_\mathrm{N}$, is ~ 200 times larger and of opposite sign compared to the prediction of the single-particle nuclear shell model [1]. A more sophisticated nuclear structure calculation [14] (axially-symmetric collective model in strong coupling) yields $\Omega = 0.003\,\mathrm{b} \times \mu_\mathrm{N}$, bringing the discrepancy with the spectroscopic determination in neutral Yb to four orders of magnitudes. As to the electric hexadecapole moment Π, the single-particle nuclear shell model again predicts zero (similar to Q) because the valence nucleon is electrically neutral. We are not aware of any nuclear structure calculations for Π of ^{173}Yb. We estimate $\Pi \approx Q^2 \approx 9\,\mathrm{b}^2$ as both Q and Π arise due to nuclear deformation; we will take this value as fiducial in further computations.

From Eqs. (2.3,2.4), we obtain the following first-order energy corrections,

$$\begin{aligned}
W_6^{(1)} &= \frac{35}{4}A + \frac{1}{4}B + C + D\,, \\
W_5^{(1)} &= \frac{11}{4}A - \frac{37}{140}B - \frac{109}{35}C - \frac{41}{7}D\,, \\
W_4^{(1)} &= -\frac{9}{4}A - \frac{3}{10}B + \frac{46}{35}C + 12D\,, \\
W_3^{(1)} &= -\frac{25}{4}A - \frac{1}{14}B + \frac{22}{7}C - \frac{44}{7}D\,, \\
W_2^{(1)} &= -\frac{37}{4}A + \frac{1}{4}B + \frac{11}{35}C - 11D\,, \\
W_1^{(1)} &= -\frac{45}{4}A + \frac{15}{28}B - \frac{33}{7}C + \frac{99}{7}D\,.
\end{aligned} \tag{2.8}$$

The second-order corrections are computed from Eqs. (2.6,2.7), where we keep magnetic dipole and electric quadrupole contributions. To streamline the notation, we introduce dipole-dipole, dipole-quadrupole, and quadrupole-quadrupole constants. These are defined for individual intermediate states $|\gamma' J'\rangle$,

$$\begin{aligned}
\eta_{\mu\mu}[\gamma' J'] &= \frac{(I+1)(2I+1)}{I} \frac{\mu^2 \langle \gamma J||T_1^e||\gamma' J'\rangle^2}{E_{\gamma J} - E_{\gamma' J'}}\,, \\
\eta_{\mu Q}[\gamma' J'] &= \frac{(I+1)(2I+1)}{I} \sqrt{\frac{2I+3}{2I-1}} \times \frac{\mu Q \langle \gamma J||T_1^e||\gamma' J'\rangle \langle \gamma J||T_2^e||\gamma' J'\rangle}{E_{\gamma J} - E_{\gamma' J'}}\,, \\
\eta_{QQ}[\gamma' J'] &= \frac{(2I+1)(I+1)(2I+3)}{4I(2I-1)} \frac{Q^2 \langle \gamma J||T_2^e||\gamma' J'\rangle^2}{E_{\gamma J} - E_{\gamma' J'}}\,.
\end{aligned} \tag{2.9}$$

Eq. (2.7) shows that we need to sum over all possible intermediate states obeying both the parity and the angular selection rules - that is, the parity of the $|\gamma J\rangle$ and $|\gamma' J'\rangle$ states has to be the same and $|J + J'| \geq k \geq |J - J'|$. Thus, for dipole-dipole and dipole-quadrupole terms, there are three possible J' values, while for quadrupole-quadrupole term, there are five possible J' values. Among the $|\gamma' J'\rangle$ intermediate states, the dominant contribution comes from the configuration $4f^{13}(^2F^o)6s^2$ with $J = 5/2$. The electronic matrix elements of other possible intermediate states are small enough to be neglected, or the energy denominators are large. With the single intermediate state fixed,

we rewrite Eq. (2.7) as

$$\begin{aligned} W_F^{(2)} &\approx C_{\mu\mu}[J',F] \times \eta_{\mu\mu}[\gamma' J'] + \\ & \quad C_{\mu Q}[J',F] \times \eta_{\mu Q}[\gamma' J'] + \\ & \quad C_{QQ}[J',F] \times \eta_{QQ}[\gamma' J'] \,, \end{aligned} \tag{2.10}$$

where the angular factors are

$$\begin{aligned} C_{\mu\mu}[J',F] &= \begin{Bmatrix} I & J & F \\ J' & I & 1 \end{Bmatrix}^2 \,, \\ C_{\mu Q}[J',F] &= \begin{Bmatrix} I & J & F \\ J' & I & 1 \end{Bmatrix} \begin{Bmatrix} I & J & F \\ J' & I & 2 \end{Bmatrix} \,, \\ C_{QQ}[J',F] &= \begin{Bmatrix} I & J & F \\ J' & I & 2 \end{Bmatrix}^2 \,. \end{aligned} \tag{2.11}$$

Adding the first-order, Eq. (2.8) and second-order, Eq (2.10), corrections for

individual hyperfine levels, we arrive at

$$\begin{aligned}
W_6^{(1+2)} &= W_6^{(1)} + 0\times\eta_{\mu\mu} + 0\times\eta_{\mu Q} + 0\times\eta_{QQ}\,,\\
W_5^{(1+2)} &= W_5^{(1)} + \frac{1}{98}\eta_{\mu\mu} + \frac{\sqrt{\frac{5}{6}}}{98}\eta_{\mu Q} + \frac{5}{588}\eta_{QQ}\,,\\
W_4^{(1+2)} &= W_4^{(1)} + \frac{11}{882}\eta_{\mu\mu} + 0\times\eta_{\mu Q} + 0\times\eta_{QQ}\,,\\
W_3^{(1+2)} &= W_3^{(1)} + \frac{1}{98}\eta_{\mu\mu} - \frac{\sqrt{\frac{2}{15}}}{49}\eta_{\mu Q} + \frac{4}{735}\eta_{QQ}\,,\\
W_2^{(1+2)} &= W_2^{(1)} + \frac{3}{490}\eta_{\mu\mu} - \frac{\sqrt{\frac{3}{10}}}{70}\eta_{\mu Q} + \frac{1}{100}\eta_{QQ}\,,\\
W_1^{(1+2)} &= W_1^{(1)} + \frac{1}{441}\eta_{\mu\mu} - \frac{1}{49\sqrt{30}}\eta_{\mu Q} + \frac{3}{490}\eta_{QQ}\,.
\end{aligned} \tag{2.12}$$

Experimentally relevant quantities are the HFS energy intervals $\Delta W_F = W_{F+1} - W_F$. Explicitly,

$$\begin{aligned}
\Delta W_5^{(1+2)} &= 6A + \frac{18}{35}B + \frac{144}{35}C + \frac{48}{7}D - \frac{1}{98}\eta_{\mu\mu} - \frac{1}{98}\sqrt{\frac{5}{6}}\eta_{\mu Q} - \frac{5}{588}\eta_{QQ}\,,\\
\Delta W_4^{(1+2)} &= 5A + \frac{1}{28}B - \frac{31}{7}C - \frac{125}{7}D - \frac{\eta_{\mu\mu}}{441} + \frac{1}{98}\sqrt{\frac{5}{6}}\eta_{\mu Q} + \frac{5}{588}\eta_{QQ}\,,\\
\Delta W_3^{(1+2)} &= 4A - \frac{8}{35}B - \frac{64}{35}C + \frac{128}{7}D + \frac{\eta_{\mu\mu}}{441} + \frac{1}{49}\sqrt{\frac{2}{15}}\eta_{\mu Q} - \frac{4}{735}\eta_{QQ}\,,
\end{aligned} \tag{2.13}$$

$$\begin{aligned}
\Delta W_2^{(1+2)} &= 3A - \frac{9}{28}B + \frac{99}{35}C + \frac{33}{7}D + \frac{1}{245}\eta_{\mu\mu}\\
&\quad + (\frac{1}{70}\sqrt{\frac{3}{10}} - \frac{1}{49}\sqrt{\frac{2}{15}})\eta_{\mu Q} - \frac{67}{14700}\eta_{QQ}\,,\\
\Delta W_1^{(1+2)} &= 2A - \frac{2}{7}B + \frac{176}{35}C - \frac{176}{7}D + \frac{17}{4410}\eta_{\mu\mu}\\
&\quad + (\frac{1}{49\sqrt{30}} - \frac{1}{70}\sqrt{\frac{3}{10}})\eta_{\mu Q} + \frac{19}{4900}\eta_{QQ}\,.
\end{aligned}$$

To determine the HFS constants A, B, C, and D from experimental measurements of ΔW_F, in Sec. 2.4 we compute the second-order corrections. Further, to find the values of nuclear octupole and hexadecapole moments from C and D we need electronic form-factors; these are also computed in Sec. 2.4. We neglect contributions of one remaining HFS constant E arising from the 2^5-pole nuclear magnetic moment. This contribution is expected to be strongly suppressed compared to the contribution of the octupole moment (see Sec. 2.5).

2.4 Calculations of electronic structure factors

2.4.1 Dirac-Hartree-Fock calculations

Yb^+ ion in the first excited state contains thirteen $4f$ electrons and two $6s$ electrons. In this section, we start our calculation of the electronic wave functions by employing the frozen core Dirac-Hartree-Fock (DHF) approximation. In this approximation, we compute the DHF orbitals of the YbIII ($[Xe]4f^{14}$) core. Then the valence (outside the $[Xe]4f^{14}$ core) orbitals are computed using the DHF potential of the core. The many-body wave function $\psi_{J,M}$ can be approximated as

$$|\psi_{J,M}\rangle \simeq \frac{1}{2}(-1)^{7/2-M} \times \\ (\sum_m (-1)^{m-1/2} a^\dagger_{6s_{1/2,m}} a^\dagger_{6s_{1/2,-m}})\, a_{4f_{7/2,-M}} |0_c\rangle\,, \tag{2.14}$$

where $a^\dagger_{6s_{1/2},m}$ are creation operators with magnetic quantum number m equal to either $-1/2$ or $1/2$, $a_{4f_{7/2,M}}$ is an annihilation operator for the $4f_{7/2}$ orbital,

and $|0_c\rangle$ represents the [Xe]$4f^{14}$ core. The phase factor $(-1)^{7/2-M}$ is generated after moving the hole operator from the core state [35]. The two $6s_{1/2}$ orbitals are coupled so that the $6s^2$ valence shell has zero value of angular momentum. Using Wick's theorem, we write the matrix element (2.2) in the multi-electron state as an expectation value in the hole orbital (see Appendix 5.1 for derivation)

$$\langle\psi_{J,M}|T^e_{k,\mu}|\psi_{J,M}\rangle = -\langle\phi_{J,-M}|t^e_{k,\mu}|\phi_{J,-M}\rangle, \tag{2.15}$$

where $|\phi_{J,-M}\rangle$ represents the $4f_{7/2}$ hole orbital with J and $-M$ being the electron's angular momentum and magnetic quantum number. The electronic tensors $T^e_{k,\mu}$ are given by Eq. (3.44). In Appendix 5.1, we show that the reduced matrix elements are related as

$$\langle\psi_J||T^e_{k,\mu}||\psi_J\rangle = (-1)^{k+1}\langle\phi_J||t^e_k||\phi_J\rangle\,, \tag{2.16}$$

with reduced matrix elements specified in Appendix 5.2. The transition from a multi-electron state to the single-electron hole orbital greatly simplifies our calculation since it only requires the one-electron $4f_{7/2}$ orbital, which can be easily obtained self-consistently with the DHF method. Our computed values of the first- and second-order hyperfine constants are listed in the first row of Table 2.2.

2.4.2 Evaluation of theoretical uncertainties

We start with a comparison of our computed values for A and B HFS constants with the previously published results and then assess our theoretical accuracy.

Table 2.2: First-order and dominant second-order hyperfine constants (in MHz) for the $4f^{13}5s^2\ {}^2F_{7/2}$ state of $^{173}Yb^+$. C/Ω is in MHz/(b $\times\ \mu_N$) and D/Π is in MHz/b^2. We used the values [2] for the nuclear magnetic dipole and electric quadrupole moments, $\mu = -0.68\,\mu_N$ and $Q = 2.80(4)$ b.

Method	A	B	C/Ω	D/Π	$\eta_{\mu\mu}$	$\eta_{\mu Q}$	η_{QQ}
This work							
DHF	-239	-5330	4.53×10^{-4}	2.00×10^{-4}	-1.50×10^{-2}	-0.112	-0.209
DHF (GRASP)	-252	-5622	4.83×10^{-4}	2.25×10^{-4}	-1.91×10^{-2}	-0.124	-0.200
MCDHF	-241	-5061	-6×10^{-4}	2.35×10^{-4}			
Prior work							
CI+MBPT, Ref. [34]	-240	-4762					
MCDHF, Ref [37]	-304	-3680					

Comparing our computed values (see Table 2.2) with theoretical values by Dzuba and Flambaum [34], we observe that our A values match, while there is a roughly 10% discrepancy in values of B. Itano (cited in Ref. [37]) has previously computed the A and B constants for the $4f^{13}6s^2$ ($J = 7/2$) state in $^{171}Yb^+$ and $^{173}Yb^+$. Itano has also used the MCDHF method, but his results are markedly different from ours. Since there are no details of calculations given in Ref. [37], it is difficult to assess the reasons for this difference. We, however, point out that our MCDHF results are in a better agreement with experimental values. For example, the deviation is about 20% between his result and the experimental value $A(^{171}\mathrm{Yb}) = 905$ MHz [38]. Multiplying our A constant for ^{173}Yb by the ratio $\mu(^{171}\mathrm{Yb})I(^{173}\mathrm{Yb})/\mu(^{173}\mathrm{Yb})I(^{171}\mathrm{Yb})$, we obtained $A = 882$ MHz for ^{171}Yb, which differs from the measurement [38] by only 3%.

Based on these comparisons we conservatively estimate the uncertainty of our MCDHF calculations to be $\sim$ 10% for the magnetic dipole and electric quadrupole hyperfine interaction constants. This estimate is also consistent with that of Ref. [34], where they claimed a similar 10% theoretical uncer-

tainty for these two constants using a different computational method. We assign a 10% theoretical uncertainty to the D constant due to its stable convergence trend with the increasing size of the virtual orbital set. However, it is difficult to evaluate the theoretical uncertainty for the C/Ω constant since it strongly depends on the computational model, as discussed below. We are, however, confident in the sign and order of magnitude of this octupole constant. The magnetic octupole HFS constant has proven to be sensitive to the

Table 2.3: Values of C/Ω (in units of kHz/(b $\times$ $\mu_{\rm N}$)) as a function of the MCDHF computational model space. The columns present the trend with opening successively deeper core subshells: the first row has no core subshells opened, while the last row lists results with the $3s3p3d4s4p4d5p5s$ core subshells opened. The rows compile values obtained by increasing numbers of virtual orbitals. $N^{\rm th}$ layer includes N virtual orbitals for each of the s, p, d, f, g, h, i angular symmetries. For example, the 1st layer includes one virtual orbitals for each $l \in [0, 6]$, i.e. 7 orbitals in total. The value marked in bold was obtained with the largest model space.

	1st layer	2nd layer	3rd layer	4th layer	5th layer
no opened subshells	0.578	0.630	0.649	0.652	0.652
$5s$	1.692	2.857	2.625	2.708	2.646
$+5p$	2.453	3.633	3.360	3.439	3.366
$+4d$	1.986	3.072	2.778	2.822	2.749
$+4p$	2.014	2.823	2.148	1.904	1.685
$+4s$	2.239	3.126	2.380	2.058	1.792
$+3d$	2.131	2.956	2.173	1.822	1.541
$+3p$	2.007	2.208	0.941	0.276	-0.198
$+3s$	1.932	2.037	0.688	-0.040	**-0.558**

electron correlations, as they flip the sign of the DHF result. We systematically investigated the dependence of the calculated C/Ω values on the size of computational model space, see Table 2.3. For example, in this table, the results in the "no opened subshells" row demonstrate the effect of correlation between electrons in the valence subshells. Because the octupole coupling op-

erator has high multiplicity (tensor of rank 3) and we are interested in the properties of the $l = 3$ f-state hole, we include up to $l = 6$ virtual orbitals in each layer. The results including the valence-valence correlation show a good convergence pattern (first row of Table 2.3). However, the convergence pattern worsens when we start including core-valence correlations by opening core subshells (columns of Table 2.3). While the results show some degree of convergence, results from an even larger model space would have been more conclusive. Unfortunately, the largest computation model that we employed already pushes the limits of computational power at our disposal. Considering the convergence trends of Table 2.3, we believe that the sign and the order of magnitude of the computed C/Ω constant would not change with increasing model space. We carried out additional convergence tests that support this conclusion. For example, trends in Table 2.3 indicate that opening the $3p$ and $4p$ subshells substantially modify the result; so it is plausible that opening the subshell of the same angular momentum, $2p$ subshell, might modify the result further. To test this hypothesis, we opened the $2p$ subshell for a small model space and found this effect to be negligible. We take the result obtained with the largest model space as our final value, $C/\Omega = -6 \times 10^{-4}\,\mathrm{MHz}/(\mathrm{b} \times \mu_\mathrm{N})$.

As to the second-order corrections η_X, these are proportional to various products of electronic matrix elements of magnetic-dipole and electric-quadrupole hyperfine interactions. Based on our accuracy estimates for A and B, we conservatively assign $\sim 10\%$ theoretical uncertainty to such matrix elements. Thereby, we expect a $\sim 10\%$ theoretical uncertainty in the second-order HFS constants. In addition, the second-corrections contain summation over intermediate states; in our calculations we truncated the entire sum to a

single contribution from the lowest-energy $F_{5/2}$ state. We examined contributions from other 12 lowest-energy intermediate states and found that $\eta_{\mu\mu}$, $\eta_{\mu Q}$, η_{QQ} are modified by less than 4%, 8%, and 20%, respectively. Thus the overall theoretical uncertainty in second-order corrections is in the order of 10%.

2.5 Discussion

Because the experimental uncertainty can reach $\sim 1\,\mathrm{Hz}$, we expect that the dominant error in extracting first-order HFS constants is due to theoretical uncertainty in the second-order corrections η_X (see Sec. 2.4.2). One of the possibilities is to determine the second-order corrections directly from the experimental data, but the system of effectively 4 equations and 5 unknowns here will not allow unambiguous extraction of all 5 unknown parameters.

Instead, we solve Eqs. (2.13) for the first four HFS splittings ΔW_F for the HFS constants, A, B, C, and D. Each of the resulting equations contains a contribution from the second-order corrections. In particular, the induced variation in D is $\delta D \approx 3.4 \times 10^{-4}\,\delta\eta_{QQ}$. As discussed in Sec. 2.3, the fiducial value of the hexadecapole moment $\Pi \sim 9\,\mathrm{b}^2$, leading, in combination with results in Table 2.2, to the expected value of $D \approx 2\,\mathrm{kHz}$. Since $\eta_{QQ} \approx -200\,\mathrm{kHz}$, even a 100% error in η_{QQ} would lead to only 3% error in the extracted value of D. Estimating the induced uncertainty in C is more involved: $\delta C = -1.6 \times 10^{-3}\,\delta\eta_{\mu Q} + 8.9 \times 10^{-4}\,\delta\eta_{QQ}$. If we assume a 10% error in both $\eta_{\mu Q}$ and η_{QQ} per Sec. 2.4.2, then the induced uncertainty in C is 30 Hz. Meanwhile, the expected values of C depend substantially on the assumed value of the octupole moment Ω. If we take Ω from the spectroscopic

determination [12] in neutral Yb, the resulting value of $C \approx 21\,\mathrm{kHz}$; the nuclear shell model value of Ω (see Table 2.1) yields $C \approx 90\,\mathrm{Hz}$, and the more sophisticated nuclear model [14] reduces C to $2\,\mathrm{Hz}$. It is clear that for the latter case the uncertainties in the second order correction would mask the contribution of C to the hyperfine splittings and only an upper limit on Ω can be placed. In such a scenario, one could still determine D and extract the hexadecapole moment, as the value of D is several orders of magnitude larger than C.

Given that the well-controlled electronic structure of the ${}^2F^o_{7/2}$ state of Yb^+ should allow for the extraction of measurable, high-order spectroscopic multipole moments, it is possible that even finer detail may be possible. While nuclear theory suggests that the magnetic multipole moments may be difficult to discern, the electric moments from deformed cores appear straightforward to measure. In particular, the radioactive ^{169}Yb nuclide has spin $I = 7/2$ and a half-life of $\approx$32 days, suggesting that precision spectroscopy of the ${}^2F^o_{7/2}$ state of $^{169}Yb^+$ may reveal signatures of its electric 64-pole moment. The calculation of more 2nd-order correction terms as well as 3rd-order corrections would be required to extract this moment from the data, but we see no fundamental barriers to future studies along these lines.

Chapter 3

Hyperfine corrections to the Stark-induced transition polarizability in Cesium and their implications for atomic parity violation

3.1 Introduction

Atomic parity violation (APV) probes the electroweak sector of the Standard Model (SM) of elementary particles. At early ages, the parity-non-conservation (PNC) effect in atoms was found at the level of 10^{-11} considered too small to be detected, as discussed by Zel'dovich [39]. In 1974, the Bouchaits [40] showed that the APV effect in heavy atoms with the atomic number Z is boosted by

a factor of Z^3, opening the APV field. Since then, several experimental and theoretical works have been done, and the accuracy of PNC measurements and calculations has been improved significantly. The first APV signal was observed in 1978 by the Novosibirsk group [41] in bismuth (Bi, $Z = 83$). In 1988, a Boulder experiment [42] provided the first evidence of the nuclear-spin-dependent PNC interactions in Cesium, which later led to the discovery [43] of the nuclear anapole moment.

The APV Hamiltonian can be decomposed into the nuclear-spin-independent and nuclear-spin-dependent parts. The nuclear-spin-independent part dominates and the relevant Hamiltonian reads

$$H_W = Q_W \frac{G_F}{\sqrt{8}} \gamma_5 \rho(r) \,, \tag{3.1}$$

if we neglect the relativistic effects for nucleons and the difference between proton and neutron distributions. Here, $\rho(r)$ is the charge density, Q_W is the weak charge and γ_5 is the products of Dirac-matrices $\gamma_5 = i\gamma_0\gamma_1\gamma_2\gamma_3$. To the leading order, weak charge Q_W can be expressed as a linear combination of the numbers of protons and neutrons, Z and N. Since the electron-neutron coupling is dominant, Q_W satisfies $Q_W \approx -N$. The value of Q_W can be extracted from APV measurements and atomic-structure calculations, and the extracted value can be compared with the SM calculated value to test new physics beyond SM.

The operator H_{W} is pseudoscalar allowing states with opposite parity to survive in its matrix elements, yet the total angular momentum J is preserved. The dominant contributions to its matrix element are between the $s_{1/2}$ and

$p_{1/2}$ orbitals. Due to the exceptionally small value of Fermi constant $G_F \approx 2.22 \times 10^{-14}$ a.u., APV effects in atoms are typically small.

The nuclear-spin-dependent (NSD) effects can be reduced to the effective Hamiltonian in the electron sector [44]

$$H_{\rm NSD} = \frac{G_{\rm F}}{\sqrt{2}} \left(\eta_{\rm axial} + \eta_{\rm NAM} + \eta_{\rm hf}\right) \left(\boldsymbol{\alpha} \cdot \boldsymbol{I}\right) \rho\left(r\right) , \tag{3.2}$$

where $\rho(r)$ is the nuclear distribution, $\boldsymbol{\alpha} = \gamma_0 \boldsymbol{\gamma}$ is the velocity operator for atomic electrons and I is the nuclear spin. Here, the coefficient $\eta_{\rm axial}$ is associated with the Z exchange interaction between nucleon-axial and electron-vector ($A_n V_e$) currents, $\eta_{\rm NAM}$ parametrizes the nuclear anapole moment (NAM) contribution, and $\eta_{\rm hf}$ is due to the combined action of the hyperfine interaction and the spin-independent Z-exchange interaction between nucleon-vector and electron-axial ($V_n A_e$) currents [44]. Among the three contributions to the NSD Hamiltonian in ^{133}Cs, the anapole moment dominates [45]. The NSD contribution, being proportional to $(\boldsymbol{\alpha} \cdot \boldsymbol{I})$, is only present for the $I \neq 0$ isotopes and open-shell atoms, such as ^{133}Cs.

^{133}Cs atom has a nuclear spin of $I = 7/2$, an atomic number of $Z = 55$, and it has a single valence electron outside the [Xe]-like core. As a result of its large atomic number and relatively straightforward calculation of its atomic structure, Cs is the most commonly used element for APV measurements and calculations. In particular, the Boulder group [43] used the Cs $6S_{1/2} \rightarrow 7S_{1/2}$ E1-forbidden transition. Nominally, for this transition, the E1 transition amplitude vanishes due to the parity selection rule. However, if we include the APV Hamiltonia, these states are no longer eigenstates of the parity operator

as H_W and $H_{\rm NSD}$ admix P-states to the S-states. This opens the parity-violating transitions between the parity-mixed multi-electron states $|6S'_{1/2}\rangle$ and $|7S'_{1/2}\rangle$. The resulting APV transition amplitude reads

$$A^{\rm PNC}_{i\to f} = \langle 7S'_{1/2},\, F_f M_{F_f}| - \boldsymbol{\mathcal{E}}_L \cdot \boldsymbol{D}|6S'_{1/2},\, F_i M_{F_i}\rangle\,, \tag{3.3}$$

where $\boldsymbol{\mathcal{E}}_L$ stands for the laser electric field driving the E1 transition, $\boldsymbol{D}$ is the electric dipole operator, and the initial and final states are in the hyperfine basis. Using the perturbation theory, the APV amplitude in Eq. (3.3) can be expressed as [46]

$$\begin{aligned}
&A^{\rm PNC}_{i\to f} = \\
&\sum_n \left[\frac{\langle 7S_{1/2}, F_f M_{F_f}|H_W + H_{\rm NSD}|nP_{1/2}, F_f M_{F_f}\rangle\langle nP_{1/2}, F_f M_{F_f}|\boldsymbol{\mathcal{E}}_L\cdot\boldsymbol{D}|6S_{1/2}, F_i M_{F_i}\rangle}{E_{7S_{1/2}} - E_{nP_{1/2}}} \right. \\
&\left. + \frac{\langle 7S_{1/2}, F_f M_{F_f}|\boldsymbol{\mathcal{E}}_L\cdot\boldsymbol{D}|nP_{1/2}, F_i M_{F_i}\rangle\langle nP_{1/2}, F_i M_{F_i}|H_{\rm W} + H_{\rm NSD}|6S_{1/2}, F_i M_{F_i}\rangle}{E_{6S_{1/2}} - E_{nP_{1/2}}} \right] \\
&= i{\rm Im}(E1_{\rm PNC})\boldsymbol{\mathcal{E}}_L\langle F_f M_{F_f}|\boldsymbol{\sigma}|F_i M_{F_i}\rangle\,,
\end{aligned} \tag{3.4}$$

where $E1_{\rm PNC}$ is a pure imaginary number, and contains both the nuclear-dependent and nuclear-independent contributions and $\boldsymbol{\sigma}$ is the Pauli matrix. The size of $E1_{\rm PNC}$ is $\sim 10^{-11}$ in atomic units, which is small and difficult to detect. To this end, the Paris group [40] pioneered the Stark-interference technique, which brings in the dependence of the APV signal on transition polarizability, the focus of our paper. The Boulder group started similar research a few years later, and both groups made improvements in accuracy.

Ultimately, the Boulder group achieved an accuracy of 0.35% [46],

$$\frac{\mathrm{Im}(E1_{\mathrm{PNC}})}{\beta} = \begin{cases} -1.6349(80)\,\mathrm{mV/cm}\,, & 6S_{1/2},\, F_i = 4 \rightarrow 7S_{1/2},\, F_f = 3 \\ -1.5576(77)\,\mathrm{mV/cm}\,, & 6S_{1/2},\, F_i = 3 \rightarrow 7S_{1/2},\, F_f = 4 \end{cases} . \quad (3.5)$$

where β is the vector transition polarizability. A weighted average of the two measurements yields the nuclear-spin-independent observable (weak charge), while their difference – the nuclear-spin-dependent effect (nuclear anapole moment). This is because the only difference between the two transitions is the direction of nuclear spin [47].

It should be pointed out that the extracted nuclear anapole moment from the APV measurement [43] deviates from the nuclear-physics determination. The nuclear physics approach is to characterize weak meson-nucleon couplings in terms of parameters of Desplanques, Donoghue and Holstein (DDH) [48], who deduced SM estimates of their values. These six hadronic PNC parameters are f_π, $h_\rho^{0,1,2}$, $h_\omega^{0,1}$, where the subscript (π, ρ, w) indicates meson type and the superscript stands for isoscalar (0), isovector (1), or isotensor (2). We refer the reader to Ref. [47] for a detailed review of nuclear structure calculations of NAMs within the DDH parameterization. The constraints from a scattering of polarized protons on unpolarized proton and ^{4}He targets and emission of circularly polarized photons from ^{18}F and ^{19}F nuclei form the intersection of nuclear experimental bands, which constraints the size of the nuclear anapole moment. The derived bounds of the extracted Cs anapole moment from APV measurements lie outside the intersection region. Furthermore, a more recent review [49] omits the Cs result. These authors explain the omission by the fact that the accuracy of the constraints on the nucleon-nucleon PNC interaction derived from the NAM determinations is somewhat difficult to assess due to nuclear polarizability complications.

In addition to the above anapole moment issues, one must also consider that the value of transition polarizability determines the extracted anapole moment. Thereby, accurate knowledge of transition polarizability is required for the interpretation in terms of electroweak observables. The conventional parameterization of the Stark-induced transition amplitude $a_{i\to f}$ reads

$$a_{i\to f} = -\alpha\sqrt{3}(\hat{\boldsymbol{\varepsilon}}\otimes\hat{\boldsymbol{e}})^{(0)}\delta_{F_i,F_f}\delta_{M_i,M_f} - \beta\sqrt{2}(\hat{\boldsymbol{\varepsilon}}\otimes\hat{\boldsymbol{e}})^{(1)}\cdot\langle F_f M_f|\boldsymbol{\sigma}|F_i M_i\rangle\,. \tag{3.6}$$

Here, the two electronic-structure-dependent quantities α and β are the scalar and the vector transition polarizabilities. Unit vectors $\hat{\boldsymbol{\varepsilon}}$ and $\hat{\boldsymbol{e}}$ characterize polarization of the laser and static electric fields, respectively. States i and f are hyperfine basis states, e.g, $|i\rangle = |n_i(IJ_i)F_iM_i\rangle$ is a state obtained by the conventional coupling of the electron J and the nuclear I angular momenta, so that $\mathbf{F} = \boldsymbol{J} + \boldsymbol{I}$. The compound tensors of rank Q for two vectors $\boldsymbol{A}$ and $\boldsymbol{B}$ are understood as $(\boldsymbol{A}\otimes\boldsymbol{B})^{(Q)}_{M_Q} = \sum\limits_{\mu\nu} C^{Q\,M_Q}_{1\mu,1\nu}A^{(1)}_{\mu}B^{(1)}_{\nu}$, and the scalar product of two rank-Q tensors as $(C^{(Q)}\cdot D^{(Q)}) = \sum\limits_{\mu}(-1)^{\mu}C^{(Q)}_{\mu}D^{(Q)}_{-\mu}$. $(\hat{\boldsymbol{\varepsilon}}\otimes\hat{\boldsymbol{e}})^{(0)} = -\frac{1}{\sqrt{3}}(\hat{\boldsymbol{\varepsilon}}\cdot\hat{\boldsymbol{e}})$ and $(\hat{\boldsymbol{\varepsilon}}\otimes\hat{\boldsymbol{e}})^{(1)} = \frac{i}{\sqrt{2}}(\hat{\boldsymbol{\varepsilon}}\times\hat{\boldsymbol{e}})$.

So far, all the previous analyses of transition polarizability in Cs have neglected the tensor contribution. As we show below, the tensor contribution to Eq. (3.6) can be parameterized as

$$a_{i\to f} = ... + \gamma\langle F_f M_{F_f}|\{I\otimes I\}^{(2)}|F_i M_{F_i}\rangle(\hat{\boldsymbol{\varepsilon}}\otimes\hat{\boldsymbol{e}})^{(2)}\,, \tag{3.7}$$

where our newly-introduced tensor transition polarizability γ depends on the electronic structure. Combined with this tensor term, Eq. (3.6) is the most general parameterization of transition polarizability as long as we only keep interactions linear in the static and laser fields.

The tensor transition polarizability between $S_{1/2}$ states, γ, requires hyperfine

mixing. Similar to the formalism of the hyperfine-mediate static polarizabilities [50], the calculation of γ requires third-order analysis and involves a combination of the hyperfine interaction (HFI), $V_{\rm HFI}$ and two electric dipole interactions $-\boldsymbol{\mathcal{E}}_L \cdot \boldsymbol{D}$, and $-\boldsymbol{\mathcal{E}}_S \cdot \boldsymbol{D}$, which are due to the laser field, $\boldsymbol{\mathcal{E}}_L$ and the external static electric field, $\boldsymbol{\mathcal{E}}_S$, respectively. Various third-order HFI-mediated effects arise from combining two $E1$ perturbations with the hyperfine interaction. The most relevant research includes the hyperfine-mediated spin-dependent APV effect [45] and the computation of black body radiation (BBR) shift in Cs microwave clocks [51]. As discussed earlier, the hyperfine-mediated spin-dependent APV effect accounts for one of the three spin-dependent APV (see $\eta_{\rm hf}$ in Eq. (3.2)) effects and arises from a combination of the hyperfine interaction and the coherent, spin-independent PNC interaction from Z exchange [45]. For the BBR shift [51], the BBR coefficient can be related to the differential scalar polarizability for the hyperfine manifold of the Cs $6S_{1/2}$ ground state. The overall BBR shift of the clock frequency is the difference between the individual shifts for the $F = 4$ and $F = 3$ hyperfine levels involved in the transition. While taking the difference, the leading order polarizability of the $6S_{1/2}$ level cancels out, and one needs to evaluate the third-order spin-dependent polarizability. Other examples include hyperfine quenching of THE otherwise E1-forbidden transitions [52–54], differential AC Stark shifts in ground states of alkali atoms [50], electron bridge in nuclear transitions [55], BBR shift in atomic clocks [56, 57], "magic" trapping of hyperfine qubits [58], non-vanishing quadrupole moment of ground states of alkali atoms [59], etc.

In this paper, we re-examine the conventional computations of transition polarizabilities, and further include the contribution from the tensor polarizability in calculating the Stark-induced amplitude. As shown in Eq. (3.5), β plays an important role in extracting weak charge and the anapole moment, and substan-

tial attention has been paid over the years to determining its value. Since 2000, the most precise value of β has been determined based upon the measurements of magnetic-dipole matrix elements M1 along with the ratio M1/β [11, 60]. Another approach to obtain β is based on determinations of the scalar polarizability α along with the measurements of ratio α/β [61]. The latest most accurate determination of β was published by the Purdue group [4] who adopted the most accurate value of $\alpha/\beta = 9.905(11)$ [61] and used the sum-over-state method to calculate α. Calculations of α were performed using experimentally and theoretically determined matrix elements and energies. The uncertainties of the two approaches [4, 11] are comparable, both approximately at a level of 0.2%. However, their central values differ by $\sim 0.7\%$, limiting the accuracy in extracting electroweak observables from the Boulder APV experiment [46].

The paper is organized as follows, in Sec. 3.2, we review the Stark-interference technique and derive the second-order transition polarizabilities. In Sec. 3.3, we reproduce and compare the results with past determinations of the second-order transition polarizabilities. The third-order hyperfine-mediated transition polarizabilities are discussed in Sec. 3.5 and we focus on the tensor polarizability, γ, and discuss how the extracted anapole moment is affected by the additional contribution to the Stark-induced amplitude in Sec. 3.6.

3.2 Stark-induced E1 transition

In the presence of a DC electric field, the initial and final states of Cs mix states of opposite parity enabling the otherwise forbidden E1 transition between the $6S$ and $7S$ states. The transition rate R between these states combines the Stark-induced,

M1 and the PNC amplitudes [46]

$$R = |A^{\text{Stark}}_{i\to f} + A^{\text{M1}}_{i\to f} + A^{\text{PNC}}_{i\to f}|^2 \,. \tag{3.8}$$

Expanding Eq. (3.8) yields the Stark-PNC interference term, $2\text{Re}\{A^{\text{Stark}}_{i\to f}(A^{\text{PNC}}_{i\to f})^*\}$. The sign of the Stark-PNC interference term is a subject to the handedness of experiments when measuring the rate R. Thus, the PNC amplitude $A^{\text{PNC}}_{i\to f}$ can be extracted from the Stark-PNC interference term when measuring changes in the rate R under parity reversals. In the Boulder experiment, the DC electric field vector $\mathcal{E}^x_S\hat{e}_x$ points along the x-axis, the elliptically-polarized laser field with components along the x- and z-axis, $i\mathcal{E}^I_L\hat{e}_x + \mathcal{E}^z_L\hat{e}_z$, and the static magnetic field along the z-axis. Then the extracted PNC amplitude reads [46]

$$\frac{R_+ - R_-}{R_+ + R_-} = 2\frac{\text{Im}(E1_{\text{PNC}})\mathcal{E}^I_L}{\beta\mathcal{E}^x_S\mathcal{E}^z_L}\,, \tag{3.9}$$

where β is the vector transition polarizability. Here, the "+" and "−" signs indicate the handedness of the experimental setup when taking the measurements of R. A parity reversal occurs when flipping the direction of the applied DC electric field $\mathcal{E}^x_S$, flipping polarization direction of the laser driving the Stark-induced transition or changing the sign of the magnetic quantum numbers.

To derive the Stark-induced $E1$ transition amplitude, we start by introducing the hyperfine basis

$$|n\,(IJ)FM_F\rangle = \sum_{M_J M_I} C^{FM_F}_{n\,JM_JIM_I}|JM_J\rangle|IM_I\rangle\,, \tag{3.10}$$

where I is the nuclear spin, J is the total electronic angular momentum, and F is the grand total angular momentum, $\boldsymbol{F} = \boldsymbol{J} + \boldsymbol{I}$. Further, $M_F\,, M_J\,, M_I$ are

the magnetic quantum numbers and n stands for the remaining quantum numbers, such as the principal quantum number of the electronic state. In the hyperfine basis, Eq. (3.10), the zeroth-order initial and final states, $|i^{[0]}\rangle$ and $|f^{[0]}\rangle$ involved in the $i \to f$ transition read

$$|i\rangle = |n_i(IJ_i)F_iM_i\rangle \equiv |i^{[0]}\rangle\,, \tag{3.11a}$$

$$|f\rangle = |n_f(IJ_f)F_fM_f\rangle \equiv |f^{[0]}\rangle\,. \tag{3.11b}$$

Here and below, the superscripts in square brackets indicate the order of perturbation theory. In the presence of an externally applied static electric field $\boldsymbol{\mathcal{E}}_S$, the initial and final states acquire admixtures

$$|i^{[1]}\rangle = \sum_a |a\rangle \frac{-\boldsymbol{\mathcal{E}}_S \cdot \boldsymbol{D}_{ai}}{\Delta E_{ia}}\,, \tag{3.12a}$$

$$|f^{[1]}\rangle = \sum_a |a\rangle \frac{-\boldsymbol{\mathcal{E}}_S \cdot \boldsymbol{D}_{af}}{\Delta E_{fa}}\,, \tag{3.12b}$$

where $\Delta E_{ab} \equiv E_a - E_b$ is the energy difference, and $\boldsymbol{D}_{ab} \equiv \langle a|\boldsymbol{D}|b\rangle$ is the electric dipole matrix element. For a laser-driven transition $i \to f$, the Stark-induced transition amplitude in the E1 approximation then reads

$$\begin{aligned} A^{[2]}_{i\to f} &= \langle i^{[0]}| - \boldsymbol{\mathcal{E}}_L \cdot \boldsymbol{D}|f^{[1]}\rangle \\ &+ \langle i^{[1]}| - \boldsymbol{\mathcal{E}}_L \cdot \boldsymbol{D}|f^{[0]}\rangle \equiv \mathcal{E}_L \mathcal{E}_s a^{[2]}_{i\to f}\,, \end{aligned} \tag{3.13}$$

where in the last step, we have factored out the amplitudes of electric fields $\boldsymbol{\mathcal{E}}_L = \mathcal{E}_L\hat{\boldsymbol{\varepsilon}}$ and $\boldsymbol{\mathcal{E}}_s = \mathcal{E}_s\hat{\boldsymbol{e}}$, introducing $a^{[2]}_{i\to f}$ which still depends on the polarization vectors $\hat{\boldsymbol{\varepsilon}}$,

and $\hat{\boldsymbol{e}}$. Explicitly,

$$\begin{aligned} a^{[2]}_{i\to f} &= \sum_a \frac{\langle i^{[0]}| - \hat{\boldsymbol{\varepsilon}}\cdot\boldsymbol{D}|a\rangle\langle a| - \hat{\boldsymbol{e}}\cdot\boldsymbol{D}|f^{[0]}\rangle}{\Delta E_{fa}} \\ &+ \frac{\langle i^{[0]}| - \hat{\boldsymbol{e}}\cdot\boldsymbol{D}|a\rangle\langle a| - \hat{\boldsymbol{\varepsilon}}\cdot\boldsymbol{D}|f^{[0]}\rangle}{\Delta E_{ia}}\,. \end{aligned} \tag{3.14}$$

This expression can be decomposed into a sum over irreducible tensor operators (ITOs) using angular momenta algebra with the help of the recoupling identity [62]

$$\begin{aligned} &(P^{(k_1)}\cdot Q^{(k_1)})(R^{(k_2)}\cdot S^{(k_2)}) = \\ &\sum_Q (-1)^{Q-k_1-k_2}\{P^{(k_1)}\otimes R^{(k_2)}\}^{(Q)}\cdot\{Q^{(k_1)}\otimes S^{(k_2)}\}^{(Q)}\,, \end{aligned} \tag{3.15}$$

where operators $P^{(k_1)}$, $Q^{(k_1)}$,$R^{(k_2)}$,$S^{(k_2)}$ are ITOs, with k_1 and k_2 being their ranks. A scalar product of two rank-k ITOs is understood as the following sum over their spherical components $(P^{(k)}\cdot Q^{(k)}) = \sum_q (-1)^q P^{(k)}_q Q^{(k)}_{-q}$. A compound ITO of rank Q is defined as

$$\{P_{k_1}\otimes R_{k_2}\}^{(Q)}_q = \sum_{q_1 q_2} C^{Qq}_{k_1 q_1 k_2 q_2} P^{(k_1)}_{q_1} R^{(k_2)}_{q_2}\,, \tag{3.16}$$

with $C^{Qq}_{k_1 q_1 k_2 q_2}$ being the conventional Clebsch–Gordan coefficient and q_1 and q_2 labeling the spherical basis components of the ITOs. The possible values of Q are limited by the triangular selection rule, $|k_1 - k_2| \le Q \le k_1 + k_2$.

For our case of the electric dipole couplings, the polarization vectors and dipoles in Eq. (3.73) are ITOs of rank 1. Hence,

$$\begin{aligned} a^{[2]}_{i\to f} &= \sum_{Q=0}^{2}(-1)^Q \sum_a \left\{ (\hat{\boldsymbol{\varepsilon}}\otimes\hat{\boldsymbol{e}})^{(Q)}\frac{(\boldsymbol{D}_{ia}\otimes\boldsymbol{D}_{af})^{(Q)}}{\Delta E_{fa}} \right. \\ &\left. + (\hat{\boldsymbol{e}}\otimes\hat{\boldsymbol{\varepsilon}})^{(Q)}\frac{(\boldsymbol{D}_{ia}\otimes\boldsymbol{D}_{af})^{(Q)}}{\Delta E_{ia}} \right\}, \end{aligned} \tag{3.17}$$

where the allowed values of Q can be either 0, 1, or 2. The corresponding terms define the scalar, vector, and tensor (quadrupole) contributions to the transition polarizability.

Notice that compared to our treatment, Ref. [46] defines $A^{[2]}_{i\to f}$ with the laser and the external electric fields, $\boldsymbol{\mathcal{E}}_L$ and $\boldsymbol{\mathcal{E}}_S$, and the initial and the final states, i and f swapped. The equivalence to our $A^{[2]}_{i\to f}$ can be proven by invoking the property of ITOs,

$$\langle i|T^{(k)}_{\mu}|f\rangle = (-1)^{\mu}\langle f|T^{(k)}_{-\mu}|i\rangle^{*}\,,$$

where $T^{(k)}_{\mu}$ is a spherical component μ of ITO of rank k .

To simplify Eq. (3.17), we introduce effective ITOs,

$$a^{(Q)}_{M_Q}[k] \equiv (\boldsymbol{D}\otimes\hat{R}_k\boldsymbol{D})^{(Q)}_{M_Q}\,, \tag{3.18}$$

with the resolvent operator $\hat{R}_k \equiv (E_{\gamma_k J_k} - H_0)^{-1}$, where H_0 stands for the unperturbed atomic Hamiltonian. Indeed, $\hat{R}_k$ has the spectral resolution

$$\hat{R}_k \;=\; (E_{n_k J_k} - H_0)^{-1} = \sum_{a\neq k}\frac{1}{\Delta E_{ka}}|a\rangle\langle a|\,, \tag{3.19}$$

reproducing the energy differences in the denominators of Eq. (3.17). $\hat{R}_k$ is a scalar, thus the combination $\hat{R}_k\boldsymbol{D}$ remains a rank-1 ITO.

Applying the Wigner-Eckart theorem to ITOs (3.18), Eq. (3.17) can be simplified to

$$\begin{aligned} a^{[2]}_{i\to f} \;&=\; \sum_{Q=0}^{2} w_Q(\hat{\boldsymbol{\varepsilon}},\hat{\boldsymbol{e}})\Big\{\langle f||a[f]^{(Q)}||i\rangle \\ &+\; (-1)^Q\langle f||a[i]^{(Q)}||i\rangle\Big\}\,. \end{aligned} \tag{3.20}$$

Here the multipolar polarization weights are

$$w_Q(\hat{\boldsymbol{\varepsilon}},\hat{\boldsymbol{e}}) = \quad (-1)^Q \sum_{M_Q} (-1)^{M_Q+F_f-M_{F_f}} \times \begin{pmatrix} F_f & Q & F_i \\ -M_{F_f} & -M_Q & M_{F_i} \end{pmatrix} (\hat{\boldsymbol{\varepsilon}} \otimes \hat{\boldsymbol{e}})^{(Q)}_{M_Q}, \tag{3.21}$$

where M_{F_f}, M_Q, and M_{F_i} are the magnetic quantum numbers, and selection rules fix the value of $M_Q = M_{F_i} - M_{F_f}$. Notice that the above definition includes polarization vectors for the static and laser fields.

Explicit angular reduction leads to the following reduced matrix elements

$$\langle f||a[f]^{(Q)}||i\rangle = (-1)^{2F_f-I+F_i+J_i}[F_f,F_i,Q]^{1/2} \begin{Bmatrix} Q & J_f & J_i \\ I & F_i & F_f \end{Bmatrix} \sum_{n_aJ_a} \begin{Bmatrix} Q & J_i & J_f \\ J_a & 1 & 1 \end{Bmatrix} \frac{\langle n_fJ_f||\boldsymbol{D}||n_aJ_a\rangle\langle n_aJ_a||\boldsymbol{D}||n_iJ_i\rangle}{E_{n_fJ_f}-E_{n_aJ_a}}, \tag{3.22}$$

where $[J_1,\, J_2,\, ...\, J_n] \equiv (2J_1+1)(2J_2+1)...(2J_n+1)$. One can obtain the reduced matrix elements $\langle f||a[i]^Q||i\rangle$ from the above $\langle f||a[f]^Q||i\rangle$ by simply replacing $E_{n_fJ_f}$ with $E_{n_iJ_i}$ in the energy denominators.

Now based on the above formalism, we analyze the tensorial structure of the transition polarizability. We first observe that for the Cs $6S_{1/2} \rightarrow 7S_{1/2}$ Stark-induced transition, $J_f = J_i = 1/2$ in Eq. (3.22), and Q taking a value larger than 1 would lead to zero-valued 6j symbols. Thereby, for this special case, we are limited to $Q = 0$ (scalar) and $Q = 1$ (vector) contributions. The tensor $Q = 2$ contribution vanishes identically in the second-order, but, as we show in Sec. 3.5 would appear due to hyperfine mixing. Another observation is that, in Eq. (3.22), the sum over the intermediate states does not depend on the grand total angular momenta F of

the initial and final states.

Conventionally, the Stark-induced transition polarizability $a^{[2]}_{i\to f}$ is expressed as a linear combination of the second-order scalar and vector polarizabilities, $\alpha^{[2]}$ and $\beta^{[2]}$, which are proportional to the $Q = 0$ and $Q = 1$ contributions in Eq. (3.17), respectively. As a an important generalization of the conventional formula, we introduce the second-order tensor polarizability $\gamma^{[2]}$ here (although it vanishes in the second order for our transitions of interest)

$$\begin{aligned} a^{[2]}_{i\to j} = &- \sqrt{3(2F_f+1)}w_0(\hat{\boldsymbol{\varepsilon}},\hat{\boldsymbol{e}})\alpha^{[2]} - \sqrt{2}\langle f||\boldsymbol{\sigma}||i\rangle w_1(\hat{\boldsymbol{\varepsilon}},\hat{\boldsymbol{e}})\beta^{[2]} \\ &+ \langle f||\{I\otimes I\}^{(2)}||i\rangle w_2(\hat{\boldsymbol{\varepsilon}},\hat{\boldsymbol{e}})\gamma^{[2]}\,. \end{aligned} \tag{3.23}$$

Here $\boldsymbol{\sigma}$ are the Pauli matrices. For $J_i = J_f = 1/2$, the reduced matrix elements are explicitly

$$\langle f||\boldsymbol{\sigma}||i\rangle = \sqrt{6}(-1)^{I+F_i-1/2}\sqrt{[F_f,F_i]}\begin{Bmatrix} 1/2 & F_f & I \\ F_i & 1/2 & 1 \end{Bmatrix}, \tag{3.24a}$$

$$\begin{aligned} \langle f||\{I\otimes I\}^{(2)}||i\rangle = &(-1)^{2F_i-F_f+I-J_f}\sqrt{5}\,[F_f,F_i]^{1/2}\times \\ &I(I+1)(2I+1)\begin{Bmatrix} 1 & 1 & 2 \\ I & I & I \end{Bmatrix}\delta_{J_i,J_f}\,, \end{aligned} \tag{3.24b}$$

where the $\sqrt{6}$ factor in $\langle f||\boldsymbol{\sigma}||i\rangle$ arises from $\langle S = 1/2||\boldsymbol{\sigma}||S = 1/2\rangle \equiv \sqrt{6}$. For our target transition in ^{133}Cs, $I = 7/2$ and $J_f = J_i = 1/2$, so that $\langle f||\{I\otimes I\}^{(2)}||i\rangle$ evaluates to

$$\langle F_f||\{I\otimes I\}^{(2)}||F_i\rangle = (-1)^{F_f}6\sqrt{35}\sqrt{[F_f,F_i]}\,. \tag{3.25}$$

Now, in accordance with Eq. (3.22), the expressions for $\alpha^{[2]}$, $\beta^{[2]}$, and $\gamma^{[2]}$ are

$$\begin{aligned}
\alpha^{[2]} &= -\frac{\langle f||a[f]^{(0)}||i\rangle + \langle f||a[i]^{(0)}||i\rangle}{\sqrt{3(2F_f+1)}}\,, \\
\beta^{[2]} &= -\frac{\langle f||a[f]^{(1)}||i\rangle - \langle f||a[i]^{(1)}||i\rangle}{\sqrt{2}\langle f||\boldsymbol{\sigma}||i\rangle}\,, \\
\gamma^{[2]} &= 0, \quad \text{for } J_i = J_f = 1/2\,.
\end{aligned} \tag{3.26}$$

These expressions can be further expanded as the conventional sums over intermediate states

$$\begin{aligned}
\alpha^{[2]} &= \delta_{J_i,J_f}\sqrt{\frac{1}{6}}\sum_{n_a J_a}\frac{(-1)^{J_a-J_i}}{\sqrt{3(2J_i+1)}}\langle n_f J_f||\boldsymbol{D}||n_a J_a\rangle\langle n_a J_a||\boldsymbol{D}||n_i J_i\rangle \\
&\quad\times\left[\frac{1}{E_{n_f J_f}-E_{n_a J_a}}+\frac{1}{E_{n_i J_i}-E_{n_a J_a}}\right],
\end{aligned} \tag{3.27a}$$

$$\begin{aligned}
\beta^{[2]} &= -\frac{1}{2}\sum_{n_a J_a}\begin{Bmatrix} 1 & J_i & J_f \\ J_a & 1 & 1 \end{Bmatrix}\langle n_f J_f||\boldsymbol{D}||n_a J_a\rangle\langle n_a J_a||\boldsymbol{D}||n_i J_i\rangle \\
&\quad\times\left[\frac{1}{E_{n_f J_f}-E_{n_a J_a}}-\frac{1}{E_{n_i J_i}-E_{n_a J_a}}\right],
\end{aligned} \tag{3.27b}$$

which recover the literature expressions. In evaluations of these sums over intermediate states with the initial and final state being of the $S_{1/2}$ character, the E1 selection rules fix the intermediate states to the $P_{1/2}$ and $P_{3/2}$ angular character.

3.3 Calculations of the second-order transition polarizabilities

To evaluate the transition polarizabilities, we employ several relativistic many-body methods of atomic structure. The lowest-order approximation in the electron-

electron interaction is the mean-field Dirac-Hartree-Fock (DHF) method. We use the "frozen-core" approximation, where the DHF potential is computed self-consistently for core orbitals and the valence orbitals are determined in the resulting V^{N-1} DHF potential. Notice that even at the DHF level, the intermediate states involved in calculating $\alpha^{[2]}$ and $\beta^{[2]}$, Eq. (3.27) span a countable set of bound states and an uncountable set of states in the continuum. Since this Hilbert space is infinitely large, direct numerical summations, while possible, require different numerical implementations for various many-body methods. An elegant way to handle this issue is the B-spline approach popularized by the Notre Dame group [35, 63, 64]. The approach generates a finite and numerically complete basis set that has been proven useful in approximating otherwise infinite sums. In this approach, the set of eigenfunctions is a linear combination of B-spline functions. To improve on the Notre Dame approach, we employ the dual-kinetic balance B-spline basis set [65] to mitigate a technical issue of spurious states and to improve the numerical quality of orbitals both near and far away from the nucleus.

The low-n orbitals from the set closely resemble those obtained with the conventional finite-differencing techniques. We refer to such orbitals as "physical" states. As n increases, the mapping of the basis states to physical states washes out. The boundary value of n separating the "physical" and "non-physical" parts of the pseudo-spectrum primarily depends on the cavity radius. The "physical" states must be unperturbed by the boundary conditions imposed at the cavity walls. Our B-spline basis set contains $N = 60$ basis functions of order $k = 9$ per partial wave generated in a cavity of radius $R_{\max} = 250\,\text{a.u.}$. These parameters are chosen so that the fractional differences in the DHF eigen-energies between the basis set and the finite-difference approach for physical states ($n' \leq 12$) are within 0.015%. Similarly, the basis-set values of E1 matrix elements involving physical states differ from their

finite-difference counterparts by at most 0.1%. A detailed discussion of the proper mapping of computational orbitals to the physical states can be found in Ref. [5].

To facilitate the numerical evaluation, we break the summation in Eqs. (3.27a) and (3.27b) into three terms: the "core-valence", "main", and "tail" contributions

$$\alpha^{[2]} = \alpha^{[2]}_{\rm CV} + \alpha^{[2]}_{\rm Main} + \alpha^{[2]}_{\rm Tail}\,, \tag{3.28}$$

which correspond to the summations over $2 \leq n_a \leq 5$, $6 \leq n_a \leq 12$, $13 \leq n_a \leq \infty$, respectively. Keeping in mind a detailed comparison with the earlier work [4], we kept the same boundary between the main and tail terms. The intermediate states in the main term map into many-body states of Cs and experimental results for energies and matrix elements can be safely used.

The next-level many-body approximation is the Brueckner orbitals (BO) method. BOs qualitatively describe a phenomenon where the valence electron charge causes the atomic core to become polarized, inducing a dipole and higher-rank multipolar moments within the core. As a result, the redistributed charges within the core attract the valence electron. Compared to the DHF approximation, the BO method improves the theory-experimental agreement for valence electron removal energies. We rotate our DHF finite basis set into the BO finite basis set using the numerical method of Ref. [5].

Random phase approximation (RPA) is a linear response theory implemented within the mean-field framework [66, 67] (in our case, DHF or BO). Its primary function is to account for the screening of externally applied fields by the core electrons. The main advantages of the RPA formalism are that it is an all-order method and it is gauge-independent when computing transition amplitudes. For more details about our finite-basis-set implementation of the RPA, the reader is referred to Ref. [5].

The RPA(BO) approach incorporates both the core polarization and the core screening effects. The quality of the enumerated approximations has been studied extensively in the literature (see, e.g., Refs. [68, 69]). For example, the experimental values of ground-state hyperfine structure constants A are reproduced in the RPA(BO) method at the level of a few percent for heavy alkali-metal atoms. The quality of the RPA(BO) dipole matrix elements is substantially better, see Ref. [5]. Based on this observation, we expect the RPA(BO) approximation accuracy in computing HFI-mediated corrections to the transition polarizability to be better than 10% for Cs.

To further improve the accuracy of the main term, we will also use the relativistic CCSDpTvT values of matrix elements, recently published by our group [5]. The CCSDpTvT method is an all-order relativistic many-body approach that incorporates single (S), double (D) and triple (T) excitation from the reference DHF state [5] in the coupled cluster (CC) formalism. pTvT qualifier in CCSDpTvT refers to a perturbative treatment of core triples and a full treatment of valence triples. In addition to an accurate treatment of many-body effects, the CCSDpTvT E1 matrix elements values include scaling, dressing, Breit, and QED corrections [5]. The finite basis set used in Ref. [5] is identical to that employed in our work. Therefore, we identify the CCSDpTvT many-body states with $n \leq 12$ with the physical states and we will use the CCSDpTvT matrix elements to compute the "main" contribution to transition polarizabilities.

All these methods internally compute reduced matrix elements of the electric-dipole operator in the length gauge between the DHF or BO orbitals

$$\langle n_i\kappa_i||\boldsymbol{D}||n_j\kappa_j\rangle = -\langle\kappa_i||C_1||\kappa_j\rangle \int_0^\infty rdr \times \left[P_{n_i\kappa_i}(r)P_{n_j\kappa_j}(r) + Q_{n_i\kappa_i}(r)Q_{n_j\kappa_j}(r)\right], \tag{3.29}$$

where $P_{n_i\kappa_i}(r)$ and $Q_{n_i\kappa_i}(r)$ are the large and small radial components of Dirac bi-spinors (see textbook [35] for conventions used in our work). The reduced matrix element of the normalized spherical harmonic is

$$\langle \kappa_i || C_L || \kappa_j \rangle = \sqrt{[j_i][j_j]}(-1)^{j_i+1/2} \times \begin{pmatrix} j_i & j_j & L \\ -1/2 & 1/2 & 0 \end{pmatrix} \Pi(l_i,\, l_j,\, L)\,, \tag{3.30}$$

where l_i, l_j are the orbital angular momenta and $\Pi(\cdots)$ encodes the parity selection rule,

$$\Pi(l_a,\, l_b,\, L) = \begin{cases} 1 & \text{if } \; l_b + l_a + L \; \text{ is } \; \text{even}\,, \\ 0 & \text{otherwise.} \end{cases} \tag{3.31}$$

Table 3.1 compiles our numerical results for $\alpha^{[2]}$ and $\beta^{[2]}$. DHF serves as the baseline. In order to improve the accuracy of calculations, we include many-body RPA and BO corrections. Then we correct the RPA(BO) results using a semi-empirical approach. In the semi-empirical approach, we use the NIST recommended [70] energies for the physical states ($n' = 6 - 12$) to calculate the energy differences $E_f - E_a$ and $E_i - E_a$ in Eqs. (3.27). The reduced-dipole matrix elements $\langle nS_{1/2}||D||n'P_{1/2}\rangle$ and $\langle nS_{1/2}||D||n'P_{3/2}\rangle$ for low-energy physical states with principal quantum numbers $n = 6,\, 7$ and $n' = 6,\, 7$ are obtained statistically from the experimental values in Ref. [4, 10, 71–84] For higher-energy physical states with principal quantum numbers $n' = 8 - 12$, we utilize the CCSDpTvT E1 matrix elements [5].

As shown in Table 3.1, the BO correction has a larger impact on $\beta^{[2]}$ than on $\alpha^{[2]}$, with a 10.3% correction to the final value of $\beta^{[2]}$ compared to the 2% correction to $\alpha^{[2]}$. Additionally, the RPA reduces the value of $\alpha^{[2]}$ by almost 20%, whereas

Method	$\alpha^{[2]}$	$\beta^{[2]}$
	This work	
DHF	-348.70	29.277
+BO	8.96	-2.795
+RPA(BO)	65.66	-0.121
+Semi-emp.	5.42	0.667
+CV	0.40	0.003
Final	-268.26(48)	27.031(230)
		27.083(57) [1]
Ref. [85]		27.024(80)
Ref. [4]	-268.82(30)	27.139(49)

Table 3.1: Results for the second-order scalar and vector $6S_{1/2} \rightarrow 7S_{1/2}$ transition polarizabilities. Dirac-Hartree-Fock (DHF) approximation serves as a baseline. Higher-order many-body corrections include Brueckner orbitals (BO) and random phase approximation (RPA) implemented on a BO basis set (RPA(BO)). See the description of semi-empirical correction in the main text. Core-valence (CV) correction accounts for contributions from the core orbitals.

it contributes less than 0.1% to the vector polarizability $\beta^{[2]}$. The RPA correction leads to a more accurate estimate of $\alpha^{[2]}$, which is only 2% away from our final value, based on the semi-empirical values.

The core-valence (CV) correction in Table 3.1 accounts for the contributions from the intermediate core states ($n'P_{1/2}$ and $n'P_{3/2}$ with $n' = 2 - 5$); see Eq. (3.27)). The CV corrections are small and contribute at the 0.1% level.

In Table 3.3, we tabulate the values and uncertainties for the tail ($n' > 12$) and core-valence ($n' \leq 5$) contributions in the DHF, RPA(DHF), BO, and RPA(BO) approximations. We use the same experimental values for the dipole matrix elements involving states $6P_{1/2}$, $6P_{3/2}$, $7P_{1/2}$, and $7P_{3/2}$ as in Ref. [4]. The remaining reduced matrix elements involving $n'P_J$ states with $n' = 8 - 12$ were reevaluated using the CCSDpTvT values and uncertainties in Ref. [5]. In both cases, we used the NIST-recommended energies. [70]. Since $\alpha^{[2]}_{\text{main}}$ involves the sum of products of

	n'	CCSD [4]	CCSDpTvT [5]	dif.
	8	-2.428	-2.215	$2.13[-1]$
	9	$-4.704[-1]$	$-4.042[-1]$	$6.62[-2]$
$n'P_{3/2}$	10	$-1.652[-1]$	$-1.372[-1]$	$2.80[-2]$
	11	$-7.831[-2]$	$-6.375[-2]$	$1.46[-2]$
	12	$-4.386[-2]$	$-3.489[-2]$	$8.97[-3]$
	8	$-5.484[-1]$	$-4.592[-1]$	$8.92[-2]$
	9	$-8.018[-2]$	$-5.612[-2]$	$2.41[-2]$
$n'P_{1/2}$	10	$-2.322[-2]$	$-1.374[-2]$	$9.48[-3]$
	11	$-9.220[-3]$	$-4.841[-3]$	$4.38[-3]$
	12	$-4.814[-3]$	$-2.005[-3]$	$2.81[-3]$
Total		-3.85	-3.39	0.46

Table 3.2: Results in the CCSD [4], and CCSDpTvT [5] approximations for the contributions to thescalar transition polarizability $\alpha^{[2]}$ arising from the intermediate states $n'P_{3/2}$ and $n'P_{1/2}$ with n' ranging from 8 to 12. The CCSD values of matrix elements were used by Toh et al. [4], while the CCSDpTvT values are used in our estimates. The differences between the CCSD [4] and CCSDpTvT [5] estimates are listed in the last column. The NIST-recommended energies were used in computing energy denominators in both cases. The cumulative difference between the two methods is 0.46. The notation $x[y]$ stands for $x \times 10^y$.

reduced matrix elements, the total uncertainty is determined through error propagation under summation and multiplication.

We apply a standard statistical approach to quantify the uncertainties for the tail and CV contributions to $\alpha^{[2]}$. The mean values, μ are the RPA (BO) values, listed in Table 3.1. The uncertainties are given by

$$\sqrt{\frac{1}{k-1}\sum_{i=1}^{k}(\alpha^{[2]}_{n>12}[i]-\mu_{\rm Tail})^2}\,, \tag{3.32a}$$

$$\sqrt{\frac{1}{k-1}\sum_{i=1}^{k}(\alpha^{[2]}_{n\leq 5}[i]-\mu_{\rm CV})^2}\,, \tag{3.32b}$$

where i corresponds to a specific estimate out of $k = 3$ approximations (DHF, BO, RPA(DHF)) and $\mu_{\rm Tail} = -0.40$, $\mu_{\rm CV} = 0.40$. The uncertainty of $\alpha^{[2]}_{\rm CV}$ computed using Eq. (3.32b) is 0.19, comparable to the reported value of 0.1 in Ref. [4]. We also observe that the inclusion of RPA corrections doubles both the DHF and BO estimates of $\alpha^{[2]}_{\rm CV}$, whereas $\alpha^{[2]}_{\rm CV}$ is unchanged by the BO corrections. On the other hand, both the RPA and BO corrections impact $\alpha^{[2]}_{\rm Tail}$. While the BO corrections double the DHF estimate, the RPA corrections reduce the DHF and BO (DHF) estimates by half, leaving similar outcomes for $\alpha^{[2]}_{\rm Tail}$ in both the DHF and RPA (BO) approximations.

Our uncertainty for $\alpha^{[2]}_{\rm Tail}$ is 0.41, greater than the reported value of 0.15 in Ref. [4]. This uncertainty arises from the differences in the BO and RPA (DHF) approximations. The overall uncertainty for $\alpha^{[2]}$ is computed as

$$\delta\alpha^{[2]} = \sqrt{(\delta\alpha^{[2]}_{\rm Tail})^2 + (\delta\alpha^{[2]}_{\rm CV})^2 + (\delta\alpha^{[2]}_{\rm Main})^2}\,, \tag{3.33}$$

and evaluates to 0.48, slightly larger than the Ref. [4] uncertainty of 0.30.

Non-relativistically, the vector polarizability $\beta^{[2]}$ vanishes. This can be seen from the observation that the matrix element of a rank-1 tensor between the $L = 0$ states vanishes due to the angular selection rules, while the same matrix element between the $S_{1/2}$ ($J = 1/2$) states does not. Therefore, compared to the scalar (rank-0) transition polarizability $\alpha^{[2]}$, $\beta^{[2]}$ is suppressed. Technically, this suppression arises from a cancellation of $n'P_{1/2}$ and $n'P_{3/2}$ intermediate state contributions in Eq. (3.27b). Due to this cancellation, the calculations of $\beta^{[2]}$ are generically less reliable than those for $\alpha^{[2]}$. Our computed value using the sum-over-state approach for $\beta^{[2]}$ is in agreement with the 0.18%-accurate experimental result [85], 27.024(80). However, our error bar, estimated as in the case of $\alpha^{[2]}$, is $\sim 0.9\%$ due to the impact of an order-of-magnitude cancellations in calculations of $\beta^{[2]}$. To improve the

n range	Contribution	DHF	RPA(DHF)	BO	RPA(BO)	Semi-emp.	σ
			This work				
$n' \leqslant 5$	$\alpha^{[2]}_{\rm CV}$	0.20	0.41	0.21	0.40		0.19
$n' > 12$	$\alpha^{[2]}_{\rm Tail}$	−0.43	−0.23	−0.96	−0.40		0.41
$6 \leqslant n' \leqslant 12$	$\alpha^{[2]}_{\rm Main}$					-268.26	0.16
Total	$\alpha^{[2]}$					−268.26	0.48
			Toh et al. [4]				
$n' \leqslant 5$	$\alpha^{[2]}_{\rm CV}$	0.20					0.10
$n' > 12$	$\alpha^{[2]}_{\rm Tail}$	−0.30					0.15
$6 \leqslant n' \leqslant 12$	$\alpha^{[2]}_{\rm Main}$					−268.72	0.24
Total	$\alpha^{[2]}$					−268.82	0.30

Table 3.3: Values of the main, tail, and core-valence (CV) contributions to the scalar transition polarizability $\alpha^{[2]}$ in various approximations. The evaluated uncertainties, σ, of these contributions are listed in the last column. Our total value includes a semi-empirical value for the main term and the RPA(BO) values for the tail and CV contributions. In the bottom part of the Table, we list the corresponding values from Ref. [4].

accuracy we use our computed value of $\alpha^{[2]} = 268.26(48)$ along with the measured ratio [61], $\alpha/\beta = 9.905(11)$ to determine $\beta^{[2]}$. Our resulting value is 27.083(57) to be compared with the latest reported semi-empirical value [4] of 27.139(42). While the error bars of both results overlap, the central values differ by 0.2%.

We compare our and previous determinations of β in Fig. 3.1. In the left panel, α is calculated first using the sum-over-state approach. Then β is determined by combining the determined α with the experimentally determined ratio α/β. In the right panel, β is determined by combining the experimental determinations of $M1_{hf}/\beta$ and theoretical estimates of $M1_{hf}$. The most accurate value of β among the left panel determinations is 27.139 (42), reported by Toh et al. [4], who combined semi-empirically determined α and the measured ratio [61] α/β. The most accurate estimate on the right panel is 26.957 (51) [11], evaluated using the measured [60] ratio $M1_{\rm hf}/\beta$ and the computed [11] value of $M1_{\rm hf}$. The tension arises from the two most accurate estimates due to the 0.7% difference between their center values and

their non-overlapping uncertainties. Our work partially relieves this tension because compared to the value [11], our value is about 0.5% higher while the uncertainties are still non-overlapping.

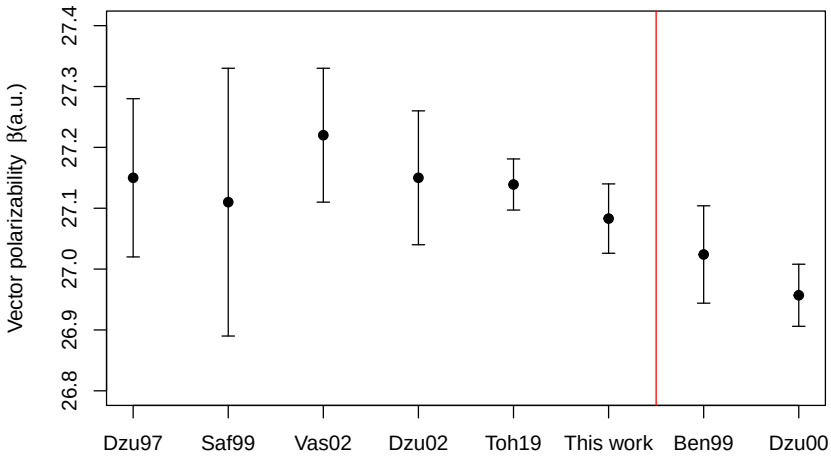

Figure 3.1: Comparison of our value of the vector transition polarizability $\beta^{[2]}$ (This work) with the literature values [4, 6–11]. The previous determinations of β are identified by the initial three letters of the first author's last name and the abbreviated publication year.

3.4 The Dalgarno-Lewis method

Alternatively, the perturbed states can be obtained by solving a two-component inhomogeneous equation

$$((h)_{\tilde{\kappa}} + (V_{\mathrm{HF}})_{\tilde{\kappa}} + \varepsilon_j)\widetilde{\psi_j} = -r \begin{pmatrix} 1 & 0 \\ & \\ 0 & 1 \end{pmatrix} \hat{C}_1^0 \psi_j \,, \tag{3.34}$$

that arises from the admixing-state representation of the Stark-induced amplitude (see Eq. (3.13)). This equation can be applied to either the initial state i or the final state f, and depends on the relativistic quantum number for the perturbed state $\tilde{\kappa}$. $\tilde{\kappa}$ can take on the values -2 and 1 for the $P_{3/2}$ and $P_{1/2}$ intermediate states, respectively. The general form of normalized spherical harmonics $\hat{C}_1^0$ in Eq. (3.34) is given by

$$C_{LM}(\hat{\boldsymbol{r}}) = \sqrt{\frac{4\pi}{2L+1}} Y_{LM}(\hat{\boldsymbol{r}})\,, \tag{3.35}$$

where Y is the conventional spherical harmonics operator, L is the rank and M is the magnetic quantum number. It should be noted that, for the purpose of comparison with the B-spline approach, this paper neglects the dependence of V_{HF} on the core orbitals, which results in a perturbed Hartree-Fock potential denoted as $\widetilde{\mathrm{HF}}$. For more information on $\widetilde{\mathrm{HF}}$, please refer to Ref. [86]. By taking the dot product with $\begin{pmatrix} \Omega^*_{\tilde{\kappa}m} \\ \Omega^*_{-\tilde{\kappa}m} \end{pmatrix}$ on both sides for Eq. (3.34) and then integrating with respect to the solid angle ($\sin\theta d\theta d\phi$), we obtain,

$$((h)_\kappa + (V_{\mathrm{HF}})_{\tilde{\kappa}} - \epsilon_j)\widetilde{\mathbf{R}(r)} = -r \begin{pmatrix} 1 & 0 \\ 0 & 1 \end{pmatrix} \mathbf{R}(r) \cdot \begin{pmatrix} \langle \tilde{\kappa}m|\hat{C}_1^0|\kappa m\rangle \\ \langle -\tilde{\kappa}m|\hat{C}_1^0|-\kappa m\rangle \end{pmatrix}. \tag{3.36}$$

For simplicity, we define

$$\widetilde{R'(r)} = \begin{pmatrix} \widetilde{P(r)}/\langle \tilde{\kappa}m|\hat{C}_1^0|\kappa m\rangle \\ \widetilde{Q(r)}/\langle -\tilde{\kappa}m|\hat{C}_1^0|-\kappa m\rangle \end{pmatrix}. \tag{3.37}$$

Then, the inhomogeneous equation simplifies to

$$[(h)_{\tilde{\kappa}} + (V_{\rm HF})_{\tilde{\kappa}} - \epsilon_j]\,\widetilde{\mathbf{R}'(r)} = -r \begin{pmatrix} 1 & 0 \\ 0 & 1 \end{pmatrix} \mathbf{R}(r)\,, \tag{3.38}$$

where $\widetilde{R'(r)}$ is the radial component for

$$\widetilde{\psi}'_j = \widetilde{\psi_j}/\langle \tilde{\kappa} m|\hat{C}^0_1|\kappa m\rangle = \sum_n \frac{|n,\,\widetilde{\kappa}\rangle\langle n,\,\widetilde{\kappa}||\mathbf{D}||\psi_j\rangle}{(E_j - E_{n,\tilde{\kappa}})\langle\tilde{\kappa}||\hat{C}_1||\kappa\rangle}. \tag{3.39}$$

Here, we applied the identity, $\langle \tilde{\kappa} m|\hat{C}^0_1|\kappa m\rangle = \langle -\tilde{\kappa} m|\hat{C}^0_1| - \kappa m\rangle$

To solve for $\widetilde{R'(r)}$ in Eq. (3.38), we first separate out the exchange potential from $V_{\rm HF}$ and move it to the right side

$$\left[(h)_{\tilde{\kappa}} + (V^{\rm dir}_{\rm HF})_{\tilde{\kappa}} - \epsilon_j\right]\widetilde{\mathbf{R}'(r)} = -r \begin{pmatrix} 1 & 0 \\ 0 & 1 \end{pmatrix} \boldsymbol{R}(r) - V^{\rm exc}_{\rm HF}\widetilde{\boldsymbol{R}'}(r)\,, \tag{3.40}$$

leaving the direct potential $V^{\rm dir}_{\rm HF}$ to the left side. The expressions of direct and exchange potentials, $V^{\rm dir}_{\rm HF}$, $V^{\rm exc}_{\rm HF}$ can be found in Ref. [86]. We begin by setting the term $V^{\rm exc}_{\rm HF}\widetilde{\boldsymbol{R}'(r)}$ zero. Next, we follow the standard procedure of variational parameters: First, we generate the inward and outward solutions for the corresponding homogeneous equation of Eq. (3.40). Next, we calculate the Wronskian from a specific grid point (the Wronskian is the same for all grid points) and eventually generate the inhomogeneous solution. For more details on the variational parameters method, please refer to Ref. [86]. We then start our iteration, feeding the solution back into the forcing term (right-hand side) of Eq. (3.40) and generating the updated values $V^{\rm exc}_{\rm HF}\widetilde{\boldsymbol{R}'(r)}$, after which we solve for $\widetilde{R'(r)}$ again. To further improve the convergence, we take the weighted sum of the forcing terms from the previous two iterations as the one for the current iteration. Specifically, we define the forcing term for the nth

iteration $F(r)^{[n]}$ as:

$$F(r)^{[n]} = hF(r)^{[n-1]} + (1-h)F(r)^{[n-2]}, \tag{3.41}$$

where $F(r)$ represents the forcing term, h stands for the iteration parameter and can take on values from zero to one, and n, $n-1$, and $n-2$ represent the nth, $n-1$th, and $n-2$th iterations, respectively.

Using $\widetilde{\psi'_j}$ representation in Eq. (3.39), the second-order scalar and vector polarizability can be rewritten as

$$\begin{aligned}
\alpha^{[2]} =& \delta_{J_i,J_f}\sqrt{\frac{1}{6}}\sum_{J_a}(-1)^{J_a-J_i}\frac{1}{\sqrt{3(2J_i+1)}}\times \\
& \left[\langle\kappa||\hat{C}_1||\tilde{\kappa}\rangle\cdot\langle\widetilde{\psi'_f}(J_a)||\boldsymbol{D}||\psi_i\rangle + \langle\tilde{\kappa}||\hat{C}_1||\kappa\rangle\cdot\langle\psi_f||\boldsymbol{D}||\widetilde{\psi'_i}(J_a)\rangle\right], \qquad (3.42a) \\
\beta^{[2]} =& \frac{1}{6}\left[\langle\kappa||\hat{C}_1||\tilde{\kappa}\rangle\cdot\langle\widetilde{\psi'_f}(J_a=\frac{1}{2})||\boldsymbol{D}||\psi_i\rangle - \langle\tilde{\kappa}||\hat{C}_1||\kappa\rangle\cdot\langle\psi_f||\boldsymbol{D}||\widetilde{\psi'_i}(J_a=\frac{1}{2})\rangle\right] + \\
& \frac{1}{12}\left[\langle\kappa||\hat{C}_1||\tilde{\kappa}\rangle\cdot\langle\widetilde{\psi'_f}(J_a=\frac{3}{2})||\boldsymbol{D}||\psi_i\rangle - \langle\tilde{\kappa}||\hat{C}_1||\kappa\rangle\cdot\langle\psi_f||\boldsymbol{D}||\widetilde{\psi'_i}(J_a=\frac{3}{2})\rangle\right]. \qquad (3.42b)
\end{aligned}$$

For a better illustration of Eq. (3.42), we list the values for the angular reduced matrix elements in Table. 3.4.

	$\langle\tilde{\kappa}\|\|\hat{C}_1\|\|\kappa\rangle$	$\langle\kappa\|\|\hat{C}_1\|\|\tilde{\kappa}\rangle$
$\tilde{\kappa}=1$	$-\frac{2}{\sqrt{6}}$	$-\frac{2}{\sqrt{6}}$
$\tilde{\kappa}=-2$	$\frac{2}{\sqrt{3}}$	$-\frac{2}{\sqrt{3}}$

Table 3.4: Angular factors in Eq. (3.42).

The results of $\alpha_{3/2}$, $\alpha_{1/2}$, $\beta_{3/2}$, and $\beta_{1/2}$ are listed in the tables above. By employing the baseline Dalgarno-Lewis approximations, we obtain the determinations

Table 3.5: Results for $\alpha_{3/2}$

	$\alpha_{3/2}$	$\frac{1}{3\sqrt{3}}\langle\widetilde{7s'(\frac{3}{2}|)}||D|||6s\rangle$	$-\frac{1}{3\sqrt{3}}\langle 7s|||D|||\widetilde{6s'(\frac{3}{2})}\rangle$
Dalgarno-Lewis	-253.01	-420.745	167.74
B-spline	-253.15	-420.81	167.66
B-spline(with CV)	-253.00	-420.74	167.74

Table 3.6: Results for $\alpha_{1/2}$

	$\alpha_{1/2}$	First term	Second term
Dalgarno-Lewis	-95.497	-180.23	84.733
B-spline	-95.541	-180.25	84.709
B-spline(with CV)	-95.493	-180.23	84.735

Table 3.7: Results for $\beta_{3/2}$

	$\beta_{3/2}$	First term	Second term
Dalgarno-Lewis	294.24	210.37	-83.869
B-spline	294.24	210.41	-83.831
B-spline(with CV)	294.24	210.37	-83.871

Table 3.8: Results for $\beta_{1/2}$

	$\beta_{1/2}$	First term	Second term
Dalgarno-Lewis	-264.96	-180.23	84.733
B-spline	-264.96	-180.25	84.709
B-spline(with CV)	-264.96	-180.23	84.735

for the second-order scalar and vector polarizabilities as

$$\begin{aligned}\beta^{[2]}_{\mathrm{Dalgarno-Lewis}} &= \beta_{3/2}+\beta_{1/2} = 294.241 - 264.963 = 29.278\\ \alpha^{[2]}_{\mathrm{Dalgarno-Lewis}} &= \alpha_{3/2}+\alpha_{1/2} = -253.007 + (-95.497) = -348.504\end{aligned}$$

where the subscripts 3/2 and 1/2 stands for the components from the $P = 3/2$ and $P = 1/2$ intermediate states, respectively. Each contribution in the Dalgano-Lewis approximation is close to the B-spline estimates with the CV corrections because the Dalgano-Lewis method is an all-order approach and even includes the contributions from positron energy levels whose length-form E1-dipole matrix elements are highly

suppressed.

3.5 Third-order hyperfine-mediated transition polarizabilites

To evaluate the hyperfine-mediated corrections to the transition polarizability, we follow the formalism developed in Refs. [50, 56, 87]. Refs. [50, 56] computed the static differential polarizabilities for transitions between levels of the hyperfine manifold attached to the $S_{1/2}$ ground state. Ref. [87] generalized the formalism to evaluating of dynamic (AC) polarizabilities. These papers focused on the characterization of clock shifts, which formally map into the evaluation of diagonal matrix elements of the transition amplitude. Here we further generalize the formalism and consider *off-diagonal* matrix elements of the transition amplitude.

The four relevant diagrams, top (T), center (C), bottom (B), and residual (R) are shown in Fig. 3.2; each diagram involves one hyperfine interaction and two E1 interactions (one with the laser, and another one with the static field). These diagrams are named after the position of the HFI operator in the string of three operators.

Explicitly,

$$\begin{aligned}
T_{i\to f} &= \sum_{ab} \frac{V_{fa}^{\mathrm{HFI}}(\hat{\boldsymbol{\varepsilon}}\cdot\boldsymbol{D}_{ab})(\hat{\boldsymbol{e}}\cdot\boldsymbol{D}_{bi})}{\Delta E_{fa}\Delta E_{ib}} + \frac{V_{fa}^{\mathrm{HFI}}(\hat{\boldsymbol{e}}\cdot\boldsymbol{D}_{ab})(\hat{\boldsymbol{\varepsilon}}\cdot\boldsymbol{D}_{bi})}{\Delta E_{fa}\Delta E_{fb}}\,, \\
B_{i\to f} &= \sum_{ab} \frac{(\hat{\boldsymbol{\varepsilon}}\cdot\boldsymbol{D}_{fa})(\hat{\boldsymbol{e}}\cdot\boldsymbol{D}_{ab})V_{bi}^{\mathrm{HFI}}}{\Delta E_{ia}\Delta E_{ib}} + \frac{(\hat{\boldsymbol{e}}\cdot\boldsymbol{D}_{fa})(\hat{\boldsymbol{\varepsilon}}\cdot\boldsymbol{D}_{ab})V_{bi}^{\mathrm{HFI}}}{\Delta E_{fa}\Delta E_{ib}}\,, \\
C_{i\to f} &= \sum_{ab} \frac{(\hat{\boldsymbol{\varepsilon}}\cdot\boldsymbol{D}_{fa})V_{ab}^{\mathrm{HFI}}(\hat{\boldsymbol{e}}\cdot\boldsymbol{D}_{bi})}{\Delta E_{ia}\Delta E_{ib}} + \frac{(\hat{\boldsymbol{e}}\cdot\boldsymbol{D}_{fa})V_{ab}^{\mathrm{HFI}}(\hat{\boldsymbol{\varepsilon}}\cdot\boldsymbol{D}_{bi})}{\Delta E_{fa}\Delta E_{fb}}\,, \\
R_{i\to f} &= -\sum_{a}\left\{V_{ii}^{\mathrm{HFI}}\frac{(\hat{\boldsymbol{\varepsilon}}\cdot\boldsymbol{D}_{fa})(\hat{\boldsymbol{e}}\cdot\boldsymbol{D}_{ai})}{(\Delta E_{ia})^2} + V_{ff}^{\mathrm{HFI}}\frac{(\hat{\boldsymbol{e}}\cdot\boldsymbol{D}_{fa})(\hat{\boldsymbol{\varepsilon}}\cdot\boldsymbol{D}_{ai})}{(\Delta E_{fa})^2}\right\}.
\end{aligned} \tag{3.43}$$

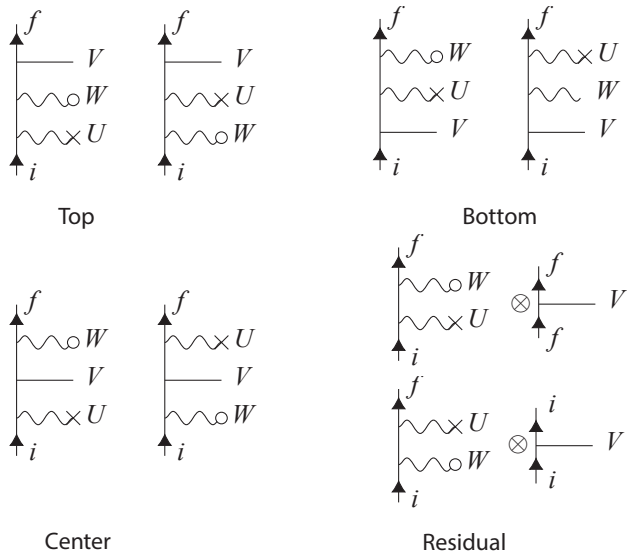

Figure 3.2: Top, Bottom, Center, and Residual (Normalization) diagrams contributing to the hyperfine-mediated corrections to transition polarizability. Here, i and f denote the initial and the final states; W, U, and V represent the interactions $-\hat{\boldsymbol{\varepsilon}} \cdot \boldsymbol{D}$, $-\hat{\boldsymbol{e}} \cdot \boldsymbol{D}$, and $V^{\rm HFI}$.

Notice that the two terms inside each combination differ by the swap of the two polarization vectors $\hat{\boldsymbol{\varepsilon}}$ and $\hat{\boldsymbol{e}}$. Otherwise, the structure of the terms is similar. Further, the bottom and top diagrams are related as $B_{f\leftrightarrow i} = T^*_{i\leftrightarrow f}$ and c.c. of the polarization vectors.

We follow Johnson [35] in our analysis of the hyperfine interaction. The HFI operator is a scalar ITO

$$V^{\rm HFI} = \sum_N \mathcal{T}^{(N)} \cdot \mathcal{N}^{(N)} \,, \tag{3.44}$$

where rank-N tensors $\mathcal{T}^{(N)}$ act in the electron space, and $\mathcal{N}^{(N)}$ — in the nuclear space. The nuclear reduced I matrix elements $\langle \gamma I || \mathcal{N}^{(N)} || \gamma I \rangle$ are expressed in terms of the conventional nuclear magnetic-dipole (M1) μ and electric-quadrupole (E2) Q

moments as

$$\langle \gamma I||\mathcal{N}^{(1)}||\gamma I\rangle = \left(\frac{(2I+1)(2I+2)}{2I}\right)^{1/2}\mu\,,$$
$$\langle \gamma I||\mathcal{N}^{(2)}||\gamma I\rangle = \frac{1}{2}\left(\frac{(2I+1)(2I+2)(2I+3)}{(2I-1)(2I)}\right)^{1/2}Q\,.$$

Here the magnetic-dipole moment $\mu \equiv g_I I \mu_N$ with μ_N being the nuclear magneton and g_I – the gyromagnetic ratio. For ^{133}Cs, $g_I = 0.73714$. As to the nuclear electric-quadrupole moment Q, the measured hyperfine constant B can be used to extract its value using theoretical values of electronic matrix elements. However, different measurements of B yield different determinations. For instance, the measured [13] hyperfine constant B in the ^{133}Cs $6P_{3/2}$ state is $-0.4934(17)$ MHz; its central value differs from a more recent result [88], $-0.5266(57)$ MHz by about 7%. Because the uncertainty in B in Ref. [13] is smaller, we simply adopt $Q = -3.55(4)$ mbarn from Ref. [13] [2]. Moreover, we find that the nuclear quadrupole contributions to transition polarizabilities are suppressed compared to those from the magnetic-dipole hyperfine interaction. We neglect even higher-rank nuclear multipoles, such as a poorly known magnetic octupole moment [13] due to their diminishing role as compared to the magnetic-dipole contribution.

The irreducible tensors of rank N, $T^{(N)}_\mu$ in Eq. (3.44), act on electronic degrees of freedom

$$T^{(N)}_\mu = \sum_i t^{(N)}_\mu(\boldsymbol{r}_i)\,, \tag{3.45}$$

where the summation is over all the atomic electrons. The one-electron operator

[2] The unit conversion from barns to a.u. is given by $Q\,(\text{a.u.}) = 3.5712 \times 10^{-8} Q\,(\text{barn})$.

are given by

$$t_{\mu}^{(N)}(\boldsymbol{r}_i) = \begin{cases} -\frac{1}{r_i^{N+1}} C_{N,\mu}(\hat{\boldsymbol{r}}_i) & \text{electric (even } k)\,, \\ \frac{-i}{r_i^{N+1}} \sqrt{\frac{N+1}{N}} \alpha \cdot \boldsymbol{C}_{N,\mu}^{(0)}(\hat{\boldsymbol{r}}_i) & \text{magnetic (odd } k)\,. \end{cases} \tag{3.46}$$

where $C_{N,\mu}$ and $\boldsymbol{C}_{N,\mu}^{[0]}$ are normalized spherical harmonics and vector spherical harmonics, respectively. Reduced matrix elements for the HFI couplings to the electric and magnetic moments are given by

$$\begin{cases} \langle n'\,\kappa' || t^{(N)} || n\,\kappa \rangle = -\langle \kappa' || C_N || \kappa \rangle \int_0^\infty \frac{dr}{r^{N+1}} (P_{n'\kappa'}(r) P_{n\kappa}(r) + Q_{n'\kappa'}(r) Q_{n\kappa}(r)) & \text{electric (even } k)\,, \\ \langle n'\,\kappa' || t^{(N)} || n\,\kappa \rangle = \langle \kappa' || C_N || -\kappa \rangle \int_0^\infty \frac{dr}{r^{N+1}} (P_{n'\kappa'}(r) Q_{n\kappa}(r) + Q_{n'\kappa'}(r) P_{n\kappa}(r)) & \text{magnetic (odd } k)\,, \end{cases} \tag{3.47}$$

where P and Q are the large and small radial components of Dirac bi-spinors, bras $|n'\,\kappa'\rangle$ and $|n\,\kappa\rangle$ specify quantum numbers of single-electron orbitals, and the reduced matrix elements $\langle \kappa' || C_N || \kappa \rangle$, $\langle \kappa' || C_N || -\kappa \rangle$ is given by Eq. (3.30).

To flesh out the tensorial structure of the transition polarizability resulting from diagrams (3.43), we use the very same re-coupling angular momentum algebra technique as in our derivation of the second-order expression, see Sec. 3.2. Since the hyperfine interaction is a scalar, the resulting tensorial structure of the transition polarizability is identical to that of the second-order polarizability (3.23):

$$\begin{aligned} a_{i\to f} &= -\sqrt{3(2F_f+1)}\, w_0(\hat{\boldsymbol{\varepsilon}}, \hat{\boldsymbol{e}})\, \alpha^{F_i \to F_f} - \sqrt{2}\, w_1(\hat{\boldsymbol{\varepsilon}}, \hat{\boldsymbol{e}})\, \langle F_f || \sigma || F_i \rangle\, \beta^{F_i \to F_f} \\ &+ \langle F_f || \{I \otimes I\}^{(2)} || F_i \rangle\, w_2(\hat{\boldsymbol{\varepsilon}}, \hat{\boldsymbol{e}})\, \gamma^{F_i \to F_f}\,, \end{aligned} \tag{3.48}$$

where the weights $w_Q(\hat{\boldsymbol{\varepsilon}}, \hat{\boldsymbol{e}})$ were defined by Eq. (3.21). In addition to the polarization vectors geometry, the weights depend on magnetic quantum numbers of the initial and final states. Notice that, unlike their second-order counterparts, now

the scalar, vector, and tensor transition polarizabilities depend on the grand total angular momenta F of the initial and final states.

The scalar and vector tensor polarizabilities, α and β, contain the second- and third-order contributions, while the tensor polarizability γ arises starting from the third order due to the hyperfine mixing. The HFI-mediated corrections are

$$\begin{aligned}
\delta\alpha^{F_i\to F_f} &= -\frac{\langle F_f||T^{(0)}+B^{(0)}+C^{(0)}+R^{(0)}||F_i\rangle}{\sqrt{3(2F_f+1)}}\,,\\
\delta\beta^{F_i\to F_f} &= -\frac{\langle F_f||T^{(1)}+B^{(1)}+C^{(1)}+R^{(1)}||F_i\rangle}{\sqrt{2}\langle F_f||\sigma||F_i\rangle}\,,\\
\delta\gamma^{F_i\to F_f} &= \frac{\langle F_f||T^{(2)}+B^{(2)}+C^{(2)}+R^{(2)}||F_i\rangle}{\langle F_f||\{I\otimes I\}^{(2)}||F_i\rangle}\,.
\end{aligned} \tag{3.49}$$

Then the various transition polarizabilities entering Eq. (3.48) are assembled as $X^{F_i\to F_f} = X^{[2]} + \delta X^{F_i\to F_f}$, where the second-order term $X^{[2]}$ is F-independent. Since $\gamma^{[2]}\equiv 0$, $\gamma^{F_i\to F_f} = \delta\gamma^{F_i\to F_f}$.

The reduced matrix elements of individual diagrams entering the above expressions are given by

$$\langle f||T^{(Q)}||i\rangle = \sum_{N,J_a,J_b} (-1)^{F_f-F_i+J_a+J_i}[F_f,F_i,Q]^{1/2}\times \begin{Bmatrix} F_f & I & J_a \\ N & J_f & I \end{Bmatrix}\begin{Bmatrix} Q & J_i & J_a \\ I & F_f & F_i \end{Bmatrix}\begin{Bmatrix} Q & J_i & J_a \\ J_b & 1 & 1 \end{Bmatrix} \times \left\{ S_T^{(J_a,J_b,N)}[fi] + (-1)^Q S_T^{(J_a,J_b,N)}[ff] \right\}, \quad (3.50)$$

$$\langle f||B^{(Q)}||i\rangle = \sum_{NJ_aJ_b} (-1)^{J_i+J_b}[F_f,F_i,Q]^{1/2}\times \begin{Bmatrix} F_i & I & J_b \\ N & J_i & I \end{Bmatrix}\begin{Bmatrix} Q & J_f & J_b \\ I & F_i & F_f \end{Bmatrix}\begin{Bmatrix} Q & J_b & J_f \\ J_a & 1 & 1 \end{Bmatrix} \times \left\{ S_B^{(J_a,J_b,N)}[ii] + (-1)^Q S_B^{J_a,J_b,N}[fi] \right\}, \quad (3.51)$$

$$\langle f||C^{(Q)}||i\rangle = \sum_{NJ_aJ_b} (-1)^{J_a-J_i+F_i-F_f+N+1}[F_f,F_i,Q]^{1/2}\times \sum_j [j]\begin{Bmatrix} J_f & J_i & j \\ F_f & F_i & Q \\ I & I & N \end{Bmatrix}\begin{Bmatrix} J_f & J_i & j \\ 1 & 1 & Q \\ J_a & J_b & N \end{Bmatrix} \times \left\{ S_C^{(J_a,J_b,N)}[ii] + (-1)^Q S_C^{(J_a,J_b,N)}[ff] \right\}, \quad (3.52)$$

$$\langle f||R^{(Q)}||i\rangle = (-1)^{2F_f-I+F_i+J_i+1}[F_f,F_i,Q]^{1/2}\begin{Bmatrix} Q & J_f & J_i \\ I & F_i & F_f \end{Bmatrix}\times \sum_{J_a}\begin{Bmatrix} Q & J_i & J_f \\ J_a & 1 & 1 \end{Bmatrix}\left\{ V[i]S_R^{J_a}[f] + (-1)^Q V[f]S_R^{J_a}[i] \right\}. \quad (3.53)$$

These contributions are expressed in terms of the reduced sums:

$$S_T^{J_a,J_b,N}[\alpha\beta]$$
$$= \sum_{n_a n_b} \frac{\langle I||\mathcal{N}^{(N)}||I\rangle\langle n_f J_f||\mathcal{T}^{(N)}||n_a J_a\rangle\langle n_a J_a||D||n_b J_b\rangle\langle n_b J_b||D||n_i J_i\rangle}{\Delta E_{\alpha a}\Delta E_{\beta b}}\,, \tag{3.54}$$

$$S_B^{(J_a,J_b,N)}[\alpha\beta]$$
$$= \sum_{n_a n_b} \frac{\langle n_f J_f||D||n_a J_a\rangle\langle n_a J_a||D||n_b J_b\rangle\langle I||\mathcal{N}^{(N)}||I\rangle\langle n_b J_b||\mathcal{T}^{(N)}||n_i J_i\rangle}{\Delta E_{\alpha a}\Delta E_{\beta b}}\,, \tag{3.55}$$

$$S_C^{J_a,J_b,N}[\alpha\beta]$$
$$= \sum_{n_a n_b} \frac{\langle n_f J_f||D||n_a J_a\rangle\langle I||\mathcal{N}^{(N)}||I\rangle\langle n_a J_a||\mathcal{T}^{(N)}||n_b J_b\rangle\langle n_b J_b||D||n_i J_i\rangle}{\Delta E_{\alpha a}\Delta E_{\beta b}}\,, \tag{3.56}$$

$$S_R^{J_a}[\alpha] = \sum_{n_a} \frac{\langle n_f J_f||D||n_a J_a\rangle\langle n_a J_a||D||n_i J_i\rangle}{(E_{n_\alpha J_\alpha} - E_{n_a J_a})^2}\,, \tag{3.57}$$

$$V[\alpha] = (-1)^{I+J_\alpha+F_\alpha} \times \sum_N \begin{Bmatrix} F_\alpha & J_\alpha & I \\ N & I & J_\alpha \end{Bmatrix}$$
$$\times \langle n_\alpha\, J_\alpha||\mathcal{T}^{(N)}||n_\alpha\, J_\alpha\rangle\langle I||\mathcal{N}^{(N)}||I\rangle\,. \tag{3.58}$$

Now based on the above expressions, we compute the hyperfine-mediated contributions to transition polarizabilities between hyperfine manifolds attached to the $6S_{1/2}$ and $7S_{1/2}$ states. We use the same many-body methods as for the second-order polarizabilities, see Sec. 3.3. The computed values are compiled in Table. 3.9.

Semi-empirical results were obtained using the NIST recommended [70] energies for the physical states, $n_{a,b}P_J$ with $n_{a,b} = 6 - 12$ and $n_{a,b}D_J$ with $n_{a,b} = 5 - 11$ and replacing electric dipole matrix elements with their experimental values [4] for the channels $(6S_{1/2}, n_{a,b}P_J)$, $(7S_{1/2}, n_{a,b}P_J)$, $n_{a,b} = 6, 7$ and their CCSDpTvT values [5] for the above channels with $n_{a,b} = 8 - 12$.

As to the hyperfine interaction, in the semi-empirical approach, we correct the

Transitions		RPA(BO)	Semi-emp
	$\delta\alpha$	$-6.779[-3]$	$-7.315[-3]$
$6S_{1/2}\,F=3 \to 7S_{1/2}\,F=3$	$\delta\beta$	$2.681[-3]$	$2.735[-3]$
	$\delta\gamma$	$-1.209[-5]$	$-1.145[-5]$
	$\delta\alpha$	0	0
$6S_{1/2}\,F=4 \to 7S_{1/2}\,F=3$	$\delta\beta$	$-1.978[-4]$	$-1.272[-4]$
	$\delta\gamma$	$-1.849[-5]$	$-1.748[-5]$
	$\delta\alpha$	0	0
$6S_{1/2}\,F=3 \to 7S_{1/2}\,F=4$	$\delta\beta$	$7.937[-4]$	$7.351[-4]$
	$\delta\gamma$	$-1.849[-5]$	$-1.748[-5]$
	$\delta\alpha$	$5.273[-3]$	$5.689[-3]$
$6S_{1/2}\,F=4 \to 7S_{1/2}\,F=4$	$\delta\beta$	$-2.086[-3]$	$-2.127[-3]$
	$\delta\gamma$	$-1.804[-5]$	$-1.706[-5]$

Table 3.9: Hyperfine-mediated corrections to the scalar, $\delta\alpha^{F_i\to F_f}$, vector, $\delta\beta^{F_i\to F_f}$, and tensor, $\delta\gamma^{F_i\to F_f}$, transition polarizabilities for the indicated transitions in ^{133}Cs. Semi-empirical values are anticipated to have better accuracy than the RPA(BO) results. The notation $x[y]$ stands for $x\times 10^y$.

RPA(BO) values of $\mathcal{T}^{(1)}$ matrix elements involving "physical" states with principle quantum numbers $6 \le n_{a,\,b} \le 12$ in the following way. The diagonal hyperfine matrix elements were extracted from the experimental values [89–91] of hyperfine constants A from the relation,

$$A = \frac{1}{IJ}\langle \mathcal{T}^{(1)}\rangle_J \langle \mathcal{N}^{(1)}\rangle_I \,. \tag{3.59}$$

Here $\langle \mathcal{T}^{(1)}\rangle_J$ and $\langle \mathcal{N}^{(1)}\rangle_I$ are the so-called stretched matrix elements expressed in terms of the reduced matrix elements

$$\langle \mathcal{O}^{(N)}\rangle_J = \begin{pmatrix} J & N & J \\ -J & 0 & J \end{pmatrix} \langle \gamma'\, J' || \mathcal{O}^{(N)} || \gamma\, J\rangle \,. \tag{3.60}$$

The off-diagonal matrix elements between the $S_{1/2}$ states were computed by evalu-

ating the geometric mean of the diagonal matrix elements [11]

$$\langle n'\,S_{1/2}|V^{\rm HFI}|n\,S_{1/2}\rangle = \sqrt{\langle n'\,S_{1/2}|V^{\rm HFI}|n'\,S_{1/2}\rangle\langle n\,S_{1/2}|V^{\rm HFI}|n\,S_{1/2}\rangle}\,, \qquad (3.61)$$

where the diagonal matrix elements come from the experimental values of the hyperfine constant A. The high accuracy of this approximation has been confirmed in Ref. [92]. The remaining off-diagonal HFS matrix elements between "physical" states were determined using the CCSDpTvT method [5]. As the nuclear quadrupole contributions were found to be suppressed, we employed the RPA(BO) method to estimate their contributions.

Our numerical results the hyperfine-mediated corrections to transition polarizabilities are listed in Table 3.9. Overall, the corrections to the polarizabilities are below the 10^{-2} a.u. level. The $\delta\alpha$ corrections are identically zero for the $F_i \neq F_f$ transitions due to the scalar nature of the underlying ITO. Otherwise, $|\delta\alpha^{F_i\to F_f}| \sim 5\times10^{-3}$ is about 5 orders of magnitude smaller than $|\alpha^{[2]}| \approx 3\times10^{2}$. As to the vector transition polarizability, $|\delta\beta^{F_i\to F_f}|$ is about 4-5 orders of magnitude smaller than $|\beta^{[2]}| \approx 3\times10^{1}$. The $|\delta\beta^{F_i\to F_f}|$ corrections to the $F_i = F_f$ transitions are an order of magnitude larger than those for the $F_i \neq F_f$ transitions. We observe that the tensor polarizability, $\gamma^{F_i\to F_f} = \delta\gamma^{F_i\to F_f}$, is in the order of 10^{-5} a.u.. Further, $\gamma^{3\to4} = \gamma^{4\to3}$ as can be proven by a direct examination of our analytical expressions. The difference between our RPA(BO) and semi-empirical estimates does not exceed 10%, indicating the uncertainty in our results.

3.6 Results and discussion

Neglecting the hyperfine-mediated tensor polarizability γ and the hyperfine-state dependence of the scalar α, and vector β polarizabilities may affect extraction of

electroweak observables from the APV experiments. Using the Stark-interference technique, in this section, we revisit the Boulder experiments [43, 61] and revise their extracted value of the ^{133}Cs anapole moment and the ratio α/β of the scalar and vector transition polarizabilities.

3.6.1 Reinterpretation of the Boulder PNC measurement

The Boulder experiment [43, 46] utilized the Stark interference technique to extract the ratio of the PNC amplitude to the vector transition polarizability, $\mathrm{Im}(\mathrm{E1}_{\mathrm{PNC}})/\beta$. The experiment used a spin-polarized ^{133}Cs beam subjected to an external static E-field, with a laser driving the nominally E1-forbidden transition between various hyperfine components of the ground $6S_{1/2}$ and the excited $7S_{1/2}$ state. The external E-field opened an E1 channel between these states by mixing the S and P states. In this case, the transition rate R is determined by a combination of the Stark-induced, parity-violating (PNC), and M1 transition amplitudes:

$$R = |A^{\mathrm{Stark}}_{i\to f} + A^{\mathrm{PNC}}_{i\to f} + A^{\mathrm{M_1}}_{i\to f}|^2\,, \tag{3.62}$$

with [46]

$$\begin{aligned} A^{\mathrm{Stark}}_{i\to f} &= \alpha \boldsymbol{\mathcal{E}}_L \cdot \boldsymbol{\mathcal{E}}_S \delta_{F_i,\,F_f}\delta_{M_{F_i},\,M_{F_f}} \\ &\quad + i\beta \boldsymbol{\mathcal{E}}_S \times \boldsymbol{\mathcal{E}}_L \cdot \langle F_f\,, M_{F_f}|\boldsymbol{\sigma}|F_i\,, M_{F_i}\rangle, \end{aligned} \tag{3.63a}$$

$$A^{\mathrm{PNC}}_{i\to f} = i\mathrm{Im}(\mathrm{E1}_{\mathrm{PNC}})\boldsymbol{\mathcal{E}}_{\mathrm{S}} \cdot \langle F_f\,, M_{F_f}|\boldsymbol{\sigma}|F_i\,, M_{F_i}\rangle, \tag{3.63b}$$

$$A^{M1}_{i\to f} = (M1)_{\mathrm{rad}}\,(\hat{\boldsymbol{k}}_L \times \boldsymbol{\mathcal{E}}_S) \cdot \langle F_f\,, M_{F_f}|\boldsymbol{\sigma}|F_i\,, M_{F_i}\rangle\,. \tag{3.63c}$$

Here we changed the notation of Ref. [46] to be consistent with that of the previous sections. $\boldsymbol{\mathcal{E}}_L = \mathcal{E}_L\hat{\boldsymbol{\varepsilon}}$ is the field of the excitation laser driving the transition with $\hat{\boldsymbol{k}}_L$ being its propagation direction. $\boldsymbol{\mathcal{E}}_S = \mathcal{E}_S\hat{\boldsymbol{e}}$ is the externally applied static electric field. α and β are the scalar and vector transition polarizabilities, introduced in the earlier sections. The PNC amplitude $E1_{\rm PNC}$ includes both the nuclear spin-dependent and spin-independent effects and $(M1)_{\rm rad}$ stands for the radial integral of the $6S_{1/2} - 7S_{1/2}$ M1 matrix element [46]. The matrix element of the Pauli matrices $\boldsymbol{\sigma}$ between the $L = 0$ states can be evaluated using the Wigner-Eckart theorem and the following reduced matrix element (see Appendix 5.4 for details)

$$\begin{aligned} & \langle (I,S)F_f||\sigma||(I,S)F_i\rangle \\ = \;& (-1)^{I+S+F_i+1}\sqrt{[F_f,F_i]}\begin{Bmatrix} S & F_f & I \\ F_i & S & 1 \end{Bmatrix}\langle S||\sigma||S\rangle. \end{aligned} \tag{3.64}$$

The Stark interference technique amplifies the feeble PNC amplitude by the much stronger $A^{\rm Stark}_{i\to f}$ amplitude - this interference appears as a cross term while squaring out the rate expression (3.62). To access this Stark-PNC interference term, the experiment [46] involved measuring the change in the transition rate R, Eq. (3.62), under various parity reversals. The reversals included flipping the direction of the applied DC E-field, flipping the sign of the x-component of the laser polarization or changing the sign of the magnetic quantum numbers [46]. The PNC amplitude was extracted from two transition rates measured under opposite parities is, R_+ and R_-. A parity reversal results in a change in the sign of the PNC amplitude $A^{\rm PNC}_{i\to f}$, while leaving the sign of the Stark-induced amplitude $A^{\rm Stark}_{i\to f}$ unaffected. The Stark-induced amplitude in Eq. (3.63a), $A^{\rm Stark}_{i\to f}$ generally depends on both the scalar and vector polarizabilities. However, in the Boulder experiment, the transitions were driven between the states of different values of F ($F_i \neq F_f$), and thereby,

only the vector polarizability contribution remained in Eq. (3.63a). Therefore, it is the vector polarizability β that enters the interference term with $E1_{\rm PNC}$. Explicitly, the PNC amplitude is extracted from the normalized difference in the two transition rates,

$$\frac{R^+ - R^-}{R^+ + R^-} \propto \frac{\mathrm{Im(E1_{PNC})}}{\beta}\,. \tag{3.65}$$

Now we specify the geometry of the Boulder experiment [43, 46]. In their setup, the ^{133}Cs atomic beam travels along the z-axis. An externally-applied magnetic field $\boldsymbol{B}$ is aligned along the beam propagation direction, defining the quantization axis. Before entering the excitation-laser interaction region, the atoms are optically pumped into the "stretched" hyperfine sub-levels of the $6S_{1/2}$ ground states, either $F_i = 3$, $M_{F_i} = \pm 3$ or $F_i = 4$, $M_{F_f} = \pm 4$. The transitions to the $7S_{1/2}$ hyperfine manifold are driven by a standing wave laser with the cavity axis aligned along the y-axis. The excitation laser field $\boldsymbol{\mathcal{E}}_L$ is elliptically polarized, $\boldsymbol{\mathcal{E}}_L = \mathcal{E}_L^z \hat{z} + \mathcal{E}_L^I \hat{x}$. Finally, a static and uniform E-field $\boldsymbol{\mathcal{E}}_S$ is aligned along the x-axis, mixing P-states with S-states in the interaction region.

Having reviewed the Boulder experiment, now we examine the effect of our newly-introduced tensor transition polarizability γ, and nuclear-spin-dependent corrections to α and β, and assess whether they affect the extraction of the PNC amplitude $E1_{\rm PNC}$. To this end, we rewrite Eq. (3.48) as:

$$\begin{aligned} A_{i\to f}^{\rm Stark} \;=\; & \alpha^{F_i\to F_f}\boldsymbol{\mathcal{E}}_L\cdot\boldsymbol{\mathcal{E}}_S\delta_{F_fF_i}\delta_{M_{F_f}M_{F_i}} + \\ & i\beta^{F_i\to F_f}(\boldsymbol{\mathcal{E}_L}\times\boldsymbol{\mathcal{E}_S})\,\langle F_f, M_{F_f}|\boldsymbol{\sigma}|F_i, M_{F_i}\rangle + \\ & \gamma^{F_i\to F_f}\,w_2(\hat{\boldsymbol{\varepsilon}},\hat{\boldsymbol{e}})\,\mathcal{E}_L\mathcal{E}_S\langle F_f||\{I\otimes I\}^{(2)}||F_i\rangle\,, \end{aligned} \tag{3.66}$$

where the polarization and state-dependent factor w_2 is explicitly, c.f. Eq. (3.21),

$$w_2(\hat{\boldsymbol{\varepsilon}}, \hat{\boldsymbol{e}}) = (-1)^2 \sum_{M_Q=-2}^{2} (-1)^{M_Q+F_f-M_{F_f}} \times \begin{pmatrix} F_f & 2 & F_i \\ -M_{F_f} & -M_Q & M_{F_i} \end{pmatrix} (\hat{\boldsymbol{\varepsilon}} \otimes \hat{\boldsymbol{e}})^{(2)}_{M_Q}, \tag{3.67}$$

with the reduced matrix element $\langle F_f || \{I \otimes I\}^{(2)} || F_i \rangle$ given by Eq. (3.24b). Notice that the selection rules for the 3j-symbol fix $M_Q = M_{F_i} - M_{F_i}$. Here the components of the rank-two compound tensor of electric field polarizations are

$$(\hat{\boldsymbol{\varepsilon}} \otimes \hat{\boldsymbol{e}})^{(2)}_{M_Q} = \sum_{\mu,\lambda} C^{2,M_Q}_{1,\mu\,1,\lambda} \hat{\boldsymbol{\varepsilon}}_\mu \hat{\boldsymbol{e}}_\lambda \,, \tag{3.68}$$

with the A_μ components of a vector $\boldsymbol{A}$ in the spherical basis expressed in terms of its Cartesian components as [62] $A_0 = A_z, A_{+1} = -(A_x + iA_y)/\sqrt{2}, A_{-1} = (A_x - iA_y)/\sqrt{2}$.

Taking into account the described geometry of the Boulder experiment, the Stark-induced transition amplitude, including the tensor contribution, can be simplified to

$$A^{\text{Stark}}_{i\to f} = \beta^{F_i\to F_f} \mathcal{E}^z_L \mathcal{E}^x_S C^{F_f M_{F_f}}_{F_i M_{F_f} \pm 1} \pm \gamma^{F_i\to F_f} \frac{\mathcal{E}^z_L \mathcal{E}^x_S}{2} U^{F_f M_{F_f}}_{F_i M_{F_f} \pm 1} \,, \tag{3.69}$$

where $\mathcal{E}^z_L$ and $\mathcal{E}^x_S$ are the z and x components of the laser and the applied DC electric fields, respectively. The coefficients $C^{F_f M_{F_f}}_{F_i M_{F_f} \pm 1}$ were introduced in Ref. [46]; these are expressed in terms of Clebsch-Gordan coefficients, see Appendix 5.4 for

details. Here we introduced a similar coefficient,

$$U^{F_f M_{F_f}}_{F_i M_{F_f} \pm 1} = (-1)^{F_f - M_{F_f}} \begin{pmatrix} F_f & 2 & F_i \\ -M_{F_f} & \mp 1 & M_{F_f} \pm 1 \end{pmatrix} \times \langle F_f || \{ I \otimes I \}^{(2)} || F_i \rangle \,, \tag{3.70}$$

specifying the dependence of the tensor contribution on the magnetic quantum numbers. The "±" signs appearing in the $C^{F_f M_{F_f}}_{F_i M_{F_f} \pm 1}$ and $U^{F_f M_{F_f}}_{F_i M_{F_f} \pm 1}$ factors indicate the allowed values of the magnetic quantum numbers for the initial state, given a fixed final state value of M_{F_f}. The "±" sign preceding γ originates from the rank-two compound tensor of the electric fields $(\hat{\boldsymbol{\varepsilon}} \otimes \hat{\boldsymbol{e}})^{(2)}_{M_Q}$ when the value of M_Q is changed from $+1$ to -1.

As discussed earlier, the transition rate R, Eq. (3.62), is expressed as a square of the sum of the Stark, PNC, and M1 transition amplitudes [46]. Our generalized Stark-induced amplitude is given by Eq. (3.69). The simplified PNC (3.63b) and M1 (3.63c) transition amplitudes read [46]

$$A^{\rm PNC}_{i \to f} = \mp {\rm lm}(E1_{\rm PNC}) \mathcal{E}^I_L C^{F_f M_{F_f}}_{F_i M_{F_f} \pm 1} \delta_{M_{F_i}, M_{F_f} \pm 1}, \tag{3.71a}$$

Here, because the laser field is elliptically polarized with the z component being real and the x component being imaginary, $\mathcal{E}^I_L = |\mathcal{E}^x_L|$. Then the generalized rates R_+

and R_- for the two transitions of opposite handedness are given by

$$
\begin{aligned}
&R_+ \equiv R(F_i, M_{F_f} - 1 \to F_f, M_{F_f}) = \\
&\beta^2 \, (\mathcal{E}_S^x \mathcal{E}_L^z)^2 \left(C^{F_f M_{F_f}}_{F_i M_{F_f} - 1} \right)^2 - \beta\gamma \, \mathcal{E}_S^x \mathcal{E}_L^{z\,2} C^{F_f M_{F_f}}_{F_i M_{F_f} - 1} U^{F_f M_{F_f}}_{F_i M_{F_f} - 1} \\
&+ 2\beta \, \mathrm{Im}(\mathrm{E1_{PNC}}) \mathcal{E}_S^x \mathcal{E}_L^z \mathcal{E}_L^I \left(C^{F_f M_{F_f}}_{F_i M_{F_f} - 1} \right)^2 \\
&- \gamma \, \mathcal{E}_L^z \mathcal{E}_S^x \mathcal{E}_L^I \mathrm{Im}(\mathrm{E1_{PNC}}) C^{F_f M_{F_f}}_{F_i M_{F_f} - 1} U^{F_f M_{F_f}}_{F_i M_{F_f} - 1} \,, \qquad (3.72a) \\
&R_- \equiv R(F_i, M_{F_f} + 1 \to F_f, M_{F_f}) = \\
&\beta^2 \, (\mathcal{E}_S^x \mathcal{E}_L^z)^2 (C^{F_f M_{F_f}}_{F_i M_{F_f} + 1})^2 + \beta\,\gamma \, (\mathcal{E}_S^x \mathcal{E}_L^z)^2 \, C^{F_f M_{F_f}}_{F_i M_{F_f} + 1} U^{F_f M_{F_f}}_{F_i M_{F_f} + 1} \\
&- 2\beta \, \mathrm{Im}(\mathrm{E1_{PNC}}) \mathcal{E}_S^x \mathcal{E}_L^z \mathcal{E}_L^I \left(C^{F_f M_{F_f}}_{F_i M_{F_f} + 1} \right)^2 \\
&- \gamma \mathcal{E}_L^z \mathcal{E}_S^x \mathcal{E}_L^I \mathrm{Im}(\mathrm{E1_{PNC}}) C^{F_f M_{F_f}}_{F_i M_{F_f} + 1} U^{F_f M_{F_f}}_{F_i M_{F_f} + 1} \,. \qquad (3.72b)
\end{aligned}
$$

Here we neglected the $A^{M1}_{i\to f}$ amplitude for reasons discussed in Ref. [46]. The values of relevant coefficients $C^{F_f M_{F_f}}_{F_i M_{F_f} \pm 1}$ and $U^{F_f M_{F_f}}_{F_i M_{F_f} \pm 1}$ are compiled in Table 3.10. The angular prefactors for the $F_i = 3$, $M_{F_f} - 1 \to F_f = 4$, M_{F_f} and $F_i = 4$, $M_{F_f} + 1 \to F_f = 3$, M_{F_f} transitions have the following properties

$$
\begin{aligned}
C^{F_f M_{F_f}}_{F_i M_{F_f} + 1} &= C^{F_f M_{F_f}}_{F_i M_{F_f} - 1} \,, \\
U^{F_f M_{F_f}}_{F_i M_{F_f} + 1} &= -U^{F_f M_{F_f}}_{F_i M_{F_f} - 1} \,. \qquad (3.73)
\end{aligned}
$$

With these identities, the rate ratio, Eq. (3.9), generalizes to

$$
\frac{R_+ - R_-}{R_+ + R_-} = \frac{\left(2 + \frac{\gamma^{F_i \to F_f}}{\beta^{F_i \to F_f}} \frac{U^{F_f M_{F_f}}_{F_i M_{F_f} + 1}}{C^{F_f M_{F_f}}_{F_i M_{F_f} + 1}} \right) \mathrm{Im}(\mathrm{E1}^{F_i \to F_f}_{\mathrm{PNC}}) \mathcal{E}_L^I}{\left(1 + \frac{\gamma^{F_i \to F_f}}{\beta^{F_i \to F_f}} \frac{U^{F_f M_{F_f}}_{F_i M_{F_f} + 1}}{C^{F_f M_{F_f}}_{F_i M_{F_f} + 1}} \right) \beta^{F_i \to F_f} \mathcal{E}_L^z \mathcal{E}_S^x} \,. \qquad (3.74)
$$

Transitions	$F_i = 3 \to F_f = 4$		$F_i = 4 \to F_f = 3$	
$M_{F_i} = M_{F_f} + 1$	$C_{3\,-3}^{4\,-4}$	$U_{3\,-3}^{4\,-4}$	$C_{4\,4}^{3\,3}$	$U_{4\,4}^{3\,3}$
	$\sqrt{\frac{7}{8}}$	$-42\sqrt{3}$	$-\sqrt{\frac{7}{8}}$	$-42\sqrt{3}$
$M_{F_i} = M_{F_f} - 1$	$C_{3\,3}^{4\,4}$	$U_{3\,3}^{4\,4}$	$C_{4\,-4}^{3\,-3}$	$U_{4\,-4}^{3\,-3}$
	$\sqrt{\frac{7}{8}}$	$42\sqrt{3}$	$-\sqrt{\frac{7}{8}}$	$42\sqrt{3}$

Table 3.10: Values of angular prefactors $C_{F_i M_{F_f} \pm 1}^{F_f M_{F_f}}$ and $U_{F_i M_{F_f} \pm 1}^{F_f M_{F_f}}$.

In the limit of vanishing values of the tensor polarizabilities $\gamma^{F_i \to F_f}$ and neglecting the dependence of β on F_i and F_f, this generalization recovers the Bolder analysis [43, 46] expression

$$\left(\frac{R_+ - R_-}{R_+ + R_-}\right)_{\text{Boulder}} = \frac{2\,\text{Im}(E1_{\text{PNC}}^{F_i \to F_f})\mathcal{E}_L^I}{\beta^{[2]}\mathcal{E}_L^z\mathcal{E}_S^x}\,. \tag{3.75}$$

Then the ratios $r_{F_i \to F_f}$ for the $F_i = 3 \to F_f = 4$ and $F_i = 4 \to F_f = 3$ transitions are

$$r_{3\to4} = \left(\frac{R_+ - R_-}{R_+ + R_-}\right)_{3\to4} = \frac{\left(2 - 12\sqrt{42}\frac{\gamma^{3\to4}}{\beta^{3\to4}}\right) \times \text{Im}(\text{E1}_{\text{PNC}}^{3\to4})\mathcal{E}_L^I}{\left(1 - 12\sqrt{42}\frac{\gamma^{3\to4}}{\beta^{3\to4}}\right)\beta^{3\to4}\mathcal{E}_L^z\mathcal{E}_S^x}\,, \tag{3.76a}$$

$$r_{4\to3} = \left(\frac{R_+ - R_-}{R_+ + R_-}\right)_{4\to3} = \frac{\left(2 + 12\sqrt{42}\frac{\gamma^{4\to3}}{\beta^{4\to3}}\right) \times \text{Im}(\text{E1}_{\text{PNC}}^{4\to3})\mathcal{E}_L^I}{\left(1 + 12\sqrt{42}\frac{\gamma^{4\to3}}{\beta^{4\to3}}\right)\beta^{4\to3}\mathcal{E}_L^z\mathcal{E}_S^x}\,, \tag{3.76b}$$

where the labels $3 \to 4$ and $4 \to 3$ specify the transitions.

Eqs. (3.76) can be further simplified to

$$r_{3\to4} = \left(\frac{R_+ - R_-}{R_+ + R_-}\right)_{3\to4} \approx \frac{2\mathrm{Im}(\mathrm{E1}^{3\to4}_{\mathrm{PNC}})}{\beta^{[2]}\mathcal{E}^x_S}\frac{\mathcal{E}^I_L}{\mathcal{E}^z_L} \times \left\{1 - \frac{\delta\beta^{3\to4}}{\beta^{[2]}} + 6\sqrt{42}\frac{\gamma^{3\to4}}{\beta^{[2]}}\right\}, \tag{3.77a}$$

$$r_{4\to3} = \left(\frac{R_+ - R_-}{R_+ + R_-}\right)_{4\to3} \approx \frac{2\mathrm{Im}(\mathrm{E1}^{4\to3}_{\mathrm{PNC}})}{\beta^{[2]}\mathcal{E}^x_S}\frac{\mathcal{E}^I_L}{\mathcal{E}^z_L} \times \left\{1 - \frac{\delta\beta^{4\to3}}{\beta^{[2]}} - 6\sqrt{42}\frac{\gamma^{4\to3}}{\beta^{[2]}}\right\}, \tag{3.77b}$$

where the terms in curly brackets include corrections to the Boulder expressions. With the results from Table 3.9, the corrections evaluate to -5×10^{-3} % and 3×10^{-3} % for the $3 \to 4$ and the $4 \to 3$ transitions, respectively. These are smaller than the Boulder experimental uncertainties in the $\mathrm{Im}(E1^{F_i\to F_f}_{\mathrm{PNC}})$ determination.

The PNC amplitudes $E1_{\mathrm{PNC}}$ include both the nuclear-spin independent and nuclear-spin dependent contributions. The largest impact of our analysis is on the extraction of the nuclear-spin-dependent part, and if neglecting polarizabilities' nuclear-spin-dependent contributions, the difference between Eqs. (3.77a) and (3.77b) yields the anapole moment contribution which can be extracted from [46]

$$2\frac{\mathrm{Im}(E1^{\mathrm{anapole}}_{\mathrm{PNC}})_{\mathrm{Boulder}}}{\beta^{[2]}} = \Big(r_{3\to4} - r_{4\to3}\Big)\mathcal{E}^x_S\frac{\mathcal{E}^z_L}{\mathcal{E}^I_L}\,. \tag{3.78}$$

Here, by considering the nuclear-spin dependent effects for polarizabilities, we define the effective ratios $r'_{3\to4}$ and $r'_{4\to3}$ and the resulting anapole moment yields

$$2\frac{\mathrm{Im}(E1^{\mathrm{anapole}}_{\mathrm{PNC}})}{\beta^{[2]}} = \Big(r'_{3\to4} - r'_{4\to3}\Big)\mathcal{E}^x_S\frac{\mathcal{E}^z_L}{\mathcal{E}^I_L}\,, \tag{3.79}$$

where $r'_{3\to4}$ and $r'_{4\to3}$ expressed in terms of the measured ratios $r_{3\to4}$ and $r_{4\to3}$ are

$$r'_{3\to4} = \left\{1 - 6\sqrt{42}\frac{\gamma^{3\to4}}{\beta^{[2]}} + \frac{\delta\beta^{3\to4}}{\beta^{[2]}}\right\} r_{3\to4}\,, \tag{3.80a}$$

$$r'_{4\to3} = \left\{1 + 6\sqrt{42}\frac{\gamma^{4\to3}}{\beta^{[2]}} + \frac{\delta\beta^{4\to3}}{\beta^{[2]}}\right\} r_{4\to3}\,. \tag{3.80b}$$

With our semi-empirical values from Table 3.9, we find that Eqs. (3.80a) and (3.80b) yield $r'_{3\to4} = 1.00005\, r_{3\to4}$ and $r'_{4\to3} = 0.99997\, r_{4\to3}$, respectively. This implies that $r'_{3\to4}$ is slightly larger while $r'_{4\to3}$ is slightly smaller. Thereby, we can expect the extracted value of $\mathrm{Im}(\mathrm{E1}^{4\to3}_{\mathrm{PNC}})/\beta^{[2]}$ to decrease by 3×10^{-5} while $\mathrm{Im}(\mathrm{E1}^{3\to4}_{\mathrm{PNC}})/\beta^{[2]}$ to increase by 5×10^{-5}. Because both $\mathrm{Im}(\mathrm{E1}^{4\to3}_{\mathrm{PNC}})/\beta^{[2]}$, and $\mathrm{Im}(\mathrm{E1}^{3\to4}_{\mathrm{PNC}})/\beta^{[2]}$ were reported [46] at about 1.6 mV/cm, this means that the anapole moment in our evaluation is slightly smaller, by about $\sim 1\times10^{-4}$ mV/cm. The reported value of the anapole moment [46], 0.077(11) mV/cm, thereby our correction of 1×10^{-4} mV/cm is below the uncertainty. This suggests that the impact due to the spin-dependent effects on polarizabilities is negligible at the current level of experimental uncertainty but may become more pronounced in future experiments.

3.6.2 The effect of hyperfine-mediated polarizabilities on the β/α ratio analysis

Ref. [61] describes an experiment in which a Stark-interference technique similar to the one discussed in the previous section was used to extract the ratio α/β. In this experiment, the Cs atomic beam was spin-polarized by an external magnetic field aligned along the y-axis. The reason for readjusting the spin-polarization direction is that, unlike the previous experimental setup, which only allows the vector polarizability β to remain, this experiment requires both α and β in order to extract their ratio. Specifically, Eq.(3.48) shows that the α contribution survives if and

only if the initial and final states have the same values for the F and M_F quantum numbers. One consequence of M_{F_i} and M_{F_f} requirement is that the $\hat{z}$-component of the vector $\langle F_f,\, M_{F_f}|\boldsymbol{\sigma}|F_i,\, M_{F_i}\rangle$ in front of the β contribution remains. However, the cross product between the electric fields $\boldsymbol{\mathcal{E}}_L \times \boldsymbol{\mathcal{E}}_S$ is along the y-axis in the laboratory frame. Therefore, to generate a non-zero dot product, the vector $\langle F_f,\, M_{F_f}|\boldsymbol{\sigma}|F_i,\, M_{F_i}\rangle$ must have a non-zero y-component in the laboratory frame.

To streamline the calculation, we define a new coordinate system (x', y', z') that maintains the same handedness as the original (x, y, z) laboratory frame. The coordinates in this new system are related to those in the laboratory frame as follows: $\hat{z}' = \hat{y}$, $\hat{y}' = \hat{x}$, and $\hat{x}' = \hat{z}$, preserving the quantization axis. As a result, the electric fields in this new reference frame are given by $\boldsymbol{\mathcal{E}}'_S = \mathcal{E}^x_S \hat{y}'$ and $\boldsymbol{\mathcal{E}}'_L = \mathcal{E}^z_L \hat{x}' + i\mathcal{E}^I_L \hat{y}'$.

The ^{133}Cs atomic beam in the Boulder experiment [61] undergoes a transition from the initial $6S_{1/2}$, $F_i = 3$, $M_{F_i} = 3$ to the final $7S_{1/2}$, $F_f = 3$, $M_{F_f} = 3$ state. This particular choice of states guarantees the non-vanishing contribution from the scalar polarizability to the Stark-induced amplitude (3.66). Then for the described experimental geometry,

$$\begin{aligned} A^{\text{Stark}}_{i\to f}(F_i, M_{F_i} \to F_f, M_{F_f}) &= i\alpha\, \mathcal{E}^I_L \mathcal{E}^x_S + i\beta\, \mathcal{E}^x_S \mathcal{E}^z_L C^{F_f,\, F_i}_{M_{F_f}, M_{F_i}} \\ &+ iw_2\, \langle F_f||\{I \otimes I^{(2)}\}||F_i\rangle\, \gamma \mathcal{E}^x_S \mathcal{E}^I_L\,. \end{aligned} \tag{3.81}$$

The transition rates for different handedness are

$$R_+ = (\alpha^{3\to3}\mathcal{E}^I_L + \beta^{3\to3}\mathcal{E}^z_L C^{F_f,\, F_i}_{M_{F_f} M_{F_i}} + \gamma^{3\to3}\mathcal{E}^I_L w_2 \langle F_f||\{I \otimes I^{(2)}\}||F_i\rangle)^2 (\mathcal{E}^x_S)^2_+\,, \tag{3.82a}$$

$$R_- = (\alpha^{3\to3}\mathcal{E}^I_L - \beta^{3\to3}\mathcal{E}^z_L C^{F_f,F_i}_{M_{F_f} M_{F_i}} - \gamma^{3\to3}\mathcal{E}^I_L w_2 \langle F_f||\{I \otimes I^{(2)}\}||F_i\rangle)^2 (\mathcal{E}^x_S)^2_-\,, \tag{3.82b}$$

where $(\mathcal{E}_S^x)_+$ and $(\mathcal{E}_S^x)_-$ stand for the magnitudes of the oppositely directed static E-fields, with $\mathcal{E}_L^z$ and $\mathcal{E}_L^I \equiv \mathrm{Im}(\mathcal{E}_L^x)$ being the magnitudes of the two components of the laser field driving the transition.

The experiment [61] adjusted two voltages $V^{\pm}$ generating the static fields $(\boldsymbol{\mathcal{E}}_S^x)_{\pm}$ until there was no modulation of the rate signal under E-field reversals. Thereby, we set the two rates (3.82) equal, $R_+ = R_-$, leading to

$$\frac{(\mathcal{E}_S^x)_- - (\mathcal{E}_S^x)_+}{(\mathcal{E}_S^x)_- + (\mathcal{E}_S^x)_+} = \frac{\beta^{3\to3}\mathcal{E}_L^z C^{F_f,F_i}_{M_{F_f},M_{F_i}} + w_2\langle F_f||\{I\otimes I^{(2)}\}||F_i\rangle\mathcal{E}_L^I\gamma^{3\to3}}{\alpha^{3\to3}\mathcal{E}_L^I}\,. \tag{3.83}$$

Then the ratio $\beta^{3\to3}/\alpha^{3\to3}$ can be extracted from the above equation. Here, the combined Clebsch-Gordan coefficients $C^{F_f,F_i}_{M_{F_f},M_{F_i}} = g_F\langle M_F\rangle$ with $\langle M_F\rangle$ being a population average over all the possible magnetic quantum numbers [61] and the gyro-magnetic ratio $g_F = -1/4$. Then, the polarizability ratio can be determined from

$$\frac{\beta^{3\to3}}{\alpha^{3\to3}} = \left(\frac{(\mathcal{E}_S^x)_- - (\mathcal{E}_S^x)_+}{(\mathcal{E}_S^x)_+ + (\mathcal{E}_S^x)_-} - \frac{w_2\langle F_f||\{I\otimes I^{(2)}\}||F_i\rangle\gamma^{3\to3}}{\alpha^{3\to3}}\right)\times\frac{\mathcal{E}_L^I}{g_F\langle M_F\rangle\mathcal{E}_L^z}\,. \tag{3.84}$$

This is a generalization of a similar equation in Ref. [61] which neglects both the F-dependence of the polarizabilities and the tensor polarizability contribution. The explicit correction due to the tensor polarizability to the experimentally determined ratio $\beta^{3\to3}/\alpha^{3\to3}$ is

$$\Delta_\gamma\frac{\beta^{3\to3}}{\alpha^{3\to3}} \approx -\frac{w_2\langle F_f||\{I\otimes I^{(2)}\}||F_i\rangle\gamma^{3\to3}}{\alpha^{[2]}}\frac{\mathcal{E}_L^I}{g_F\langle M_F\rangle\mathcal{E}_L^z}\,. \tag{3.85}$$

Here, the factors $w_2 = -\frac{i}{6}\sqrt{5/14}$ and $\langle F_i||\{I\otimes I\}^{(2)}||F_f\rangle = -42\sqrt{35}$ for $F_i = F_f = 3$ so that $w_2\langle F_f||\{I\otimes I^{(2)}\}||F_i\rangle$ evaluates to $17.5\sqrt{2}$. The Boulder group [61] utilized different ratios of the excitation laser polarization components, $\mathcal{E}_L^z/\mathcal{E}_L^I$, to

extract $\beta^{3\to3}/\alpha^{3\to3}$. Specifically, they used ratios of 0.995, 1.377, and 1.869. The measured [61] average spin polarization $\langle M_F\rangle = 2.975(3)$ approaches 3 because the majority of atoms are pumped into the $F = 3$, $M_F = 3$ hyperfine sub-level. With $\alpha^{[2]} = 286.26(47)$ and $\gamma^{3\to3} = -1.145 \times 10^{-5}$, the corrections to $\beta^{3\to3}/\alpha^{3\to3}$ evaluate to -1.4×10^{-6}, -1.0×10^{-6}, and -7.4×10^{-7} for the three enumerated $\mathcal{E}_L^z/\mathcal{E}_L^I$ ratios. Given that the extracted ratio [61] is $\beta^{3\to3}/\alpha^{3\to3} = -0.10096(11)$, the computed contributions $\Delta\gamma$ to $\beta^{3\to3}/\alpha^{3\to3}$ is about two orders of magnitude smaller than the experimental uncertainty. This demonstrates that while the $\gamma^{3\to3}$ contribution is negligible at the current level of accuracy, the hyperfine-mediated polarizabilities may become relevant in more accurate experiments.

Finally, to the best of our knowledge, all the previous literature identified the measured [61] α/β ratio with $\alpha^{[2]}/\beta^{[2]}$, neglecting the nuclear spin-dependent effects in computing the transition polarizabilities. However, because the Boulder group employed the $F_i = 3 \to F_f = 3$ transition, the measured ratio is, in fact, $\alpha^{3\to3}/\beta^{3\to3}$. Explicitly,

$$\frac{\alpha^{3\to3}}{\beta^{3\to3}} = \frac{\alpha^{[2]} + \delta\alpha^{3\to3}}{\beta^{[2]} + \delta\beta^{3\to3}}\,, \tag{3.86}$$

where we included the hyperfine-mediated corrections.

Plugging in our results for $\alpha^{[2]}$, $\delta\alpha^{3\to3}$, and $\delta\beta^{3\to3}$, together with the measured [61] ratio into Eq. (3.86), we obtain $\beta^{[2]} = 27.081(57)$. This value is about 0.002 lower than the one obtained neglecting the nuclear spin-dependent effects. This hyperfine-mediated correction is within the error bar at the current level of accuracy.

Chapter 4

Conclusion

In summary, we reevaluated the second-order scalar transition polarizability $\alpha^{[2]}$ for the $6S - 7S$ transition in ^{133}Cs, resulting in $\alpha^{[2]} = 268.26(48)$. Based on this result and the measured ratio of α to β [61], we obtained the vector polarizability β with a value of 27.083(57). This value reduces the current 0.7% discrepancy between the sum-over-state [4] and the $M1_{hf}$-based approaches [11] by 0.2%. Further, we evaluated the hyperfine-interaction (HFI) mediated corrections to transition polarizabilities, which included the newly introduced tensor part of polarizability γ. These HFI-mediated effects lead to the nuclear-spin-dependent contributions to Stark-induced transition amplitudes. Incorporating nuclear spin dependency into the transition polarizabilities leads to a slightly smaller anapole moment as deduced from the measurements of atomic parity violation by the Boulder group. Yet our computed correction is insufficient to resolve the tension with the nuclear physics data. The effects of tensor polarizability γ are also negligible for the determination of ratio α/β. However, with our hyperfine-mediated corrections to the scalar and vector transition polarizabilities, the center value of $\beta^{[2]}$ is slightly decreased to 27.081(57).

Chapter 5

Appendix

5.1 Relation between multi-electron and single-electron matrix elements

In this Appendix, we prove Eqs. (2.15, 2.16).

The operator $T^e_{k,\mu}$ in the second quantized form reads [93]

$$T^e_{k,\mu} = \sum_{i,j} :a^\dagger_i a_j: \langle i|t^e_{k,\mu}|j\rangle, \tag{5.1}$$

where i and j represent either core or virtual orbitals, $\langle i|t^e_{k,\mu}|j\rangle$ is the matrix element, and $:a^\dagger_i a_j:$ are products of creation and annihilation operators in the normal form. We would like to evaluate the expectation value of the operator in Eq. (5.1) in the many-body state $|\psi_{J,M}\rangle$, Eq. (2.14). The intermediate result for the expectation

value can be obtained using the Wick's theorem [93],

$$\begin{aligned}\langle 0_c|a^\dagger_{h'}a_{v'}a_{w'}:a^\dagger_i a_j:a^\dagger_w a^\dagger_v a_h|0_c\rangle &= \\ -\delta_{ih}\delta_{h'j}(\delta_{vv'}\delta_{ww'} &- \delta_{v'w}\delta_{w'v}) \\ +\delta_{jw}\delta_{h'h}(\delta_{vv'}\delta_{iw'} &- \delta_{iv'}\delta_{w'v}) \\ -\delta_{jv}\delta_{hh'}(\delta_{v'w}\delta_{w'i} &- \delta_{iv'}\delta_{ww'})\,, \end{aligned} \tag{5.2}$$

where $h(h')$ stands for the $4f$ hole orbital and $v(v')$ and $w(w')$ represent the $6s$ orbitals.

Then we immediately obtain

$$\langle\psi_{J,\,M}|T^e_{k,\mu}|\psi_{J,\,M}\rangle = -\langle h|t^e_{k,\mu}|h\rangle\,, \tag{5.3}$$

where $|\psi_{J,M}\rangle$ is the multi-electron state of $^{173}\mathrm{Yb}^+$, Eq. (2.14). The reason that the $6s$ orbitals do not contribute to Eq. (5.3) is that the operator is non-scalar and the $6s^2$ shell has zero total angular momentum by construction of the multi-electron state (2.14).

In general, Eq. (5.3) works for any non-scalar one-body operator. If we replace $T^e_{k,\mu}$ and $t^e_{k,\mu}$ with the z components of the angular momentum operators J_z and j_z respectively in Eq. (5.3), we obtain the magnetic quantum number of the hole state, m_h equal to $-M$.

Then, we rewrite Eq. (5.3) as follows,

$$\langle\psi_{J,\,M}|T^e_{k,\mu}|\psi_{J,\,M}\rangle = -\langle\phi_{J,\,-M}|t^e_{k,\mu}|\phi_{J,\,-M}\rangle\,, \tag{5.4}$$

where $\phi_{J,-M}$ is the orbital of the hole-state electron. This proves Eq. (2.15) of the main text.

Applying the Wigner-Eckart theorem and setting $\mu = 0$ on each side of Eq. (5.4), we obtain,

$$\langle \psi_{J,M} | T^e_{k,0} | \psi_{J,M} \rangle = (-1)^{J-M} \begin{pmatrix} J & k & J \\ -M & 0 & M \end{pmatrix} \langle \psi_J || T^e_k || \psi_J \rangle \quad , \tag{5.5}$$

$$-\langle \phi_{J,-M} | t^e_{k,0} | \phi_{J,-M} \rangle = -(-1)^{J+M} \begin{pmatrix} J & k & J \\ M & 0 & -M \end{pmatrix} \langle \phi_J || t^e_k(i) || \phi_J \rangle \quad . \tag{5.6}$$

Since $\begin{pmatrix} J & k & J \\ -M & 0 & M \end{pmatrix} = (-1)^{2J+k} \begin{pmatrix} J & k & J \\ M & 0 & -M \end{pmatrix}$, the reduced matrix elements satisfy the following identity,

$$\begin{aligned} \langle \psi_J || T^e_k || \psi_J \rangle &= (-1)^{1+2M+2J+k} \langle \phi_J || t^e_k || \phi_J \rangle \\ &= (-1)^{k+1} \langle \phi_J || t^e_k || \phi_J \rangle. \end{aligned} \tag{5.7}$$

Eq. (5.7) suggests that when evaluating the reduced matrix elements of even-k operators with multi-electron states, one needs to add an extra negative sign to the single-electron reduced matrix elements. The sign of odd-k reduced matrix elements is unaffected. This proves Eq.(2.16) of the main text.

Now we generalize these identities to the off-diagonal reduced matrix elements entering the second-order corrections. As discussed in Sec. 2.3, the dominant intermediate state is the $4f^{13}5s^2\,{}^2F_{5/2}$ state denoted as $|\psi_{J'M'}\rangle$. The many-body state $|\psi_{J'M'}\rangle$ has a similar form as Eq. (2.14) but differs in the phase factor, $(-1)^{5/2-M'}$

and the annihilation operator $a_{4f_{5/2,-M'}}$. It can be shown that the relation in Eq. (5.7) still holds for the reduced matrix element,

$$\langle \psi_J || T_k^e || \psi_{J'} \rangle = (-1)^{k+1} \langle \phi_J || t_k^e || \phi_{J'} \rangle. \tag{5.8}$$

5.2 Reduced matrix elements of hyperfine interaction

Formally, the one-electron wave function is represented by Dirac bi-spinor

$$|nj\kappa m\rangle = \begin{pmatrix} iP_{n\kappa}(r)\Omega_{\kappa,m}(\hat{r}) \\ Q_{n\kappa}(r)\Omega_{-\kappa,m}(\hat{r}) \end{pmatrix}, \tag{5.9}$$

where P and Q are the large and small components of one-electron wave function and κ is the relativistic quantum number ($\kappa = \mp j + \frac{1}{2}$ for $j = l \pm \frac{1}{2}$). The reduced matrix elements of the electronic part of hyperfine interaction are explicitly [35]

$$\langle n'\kappa' || t_k^e || n\kappa \rangle = \begin{cases} -\langle \kappa' || C_k || \kappa \rangle \int_0^\infty \frac{dr}{r^{k+1}} (P_{n'\kappa'} P_{n,\kappa} + Q_{n'\kappa'} Q_{n,\kappa}), & \text{odd k}, \\ \langle \kappa' || C_k || -\kappa \rangle \frac{\kappa'+\kappa}{k} \int_0^\infty \frac{dr}{r^{k+1}} (P_{n'\kappa'} Q_{n,\kappa} + Q_{n'\kappa'} P_{n,\kappa}), & \text{even k}, \end{cases} \tag{5.10}$$

where we suppressed j for brevity. The odd and even k sub-cases correspond to electric and magnetic interactions respectively.

5.3 Calculating the second-and third-order polarizabilities using single-electron state.

The goal of this appendix is to derive the second-order-and third-order polarizabilities using the single-electron states. The Cs atom can be treated as a [Xe] core with one valence electron. In the frozen-core Dirac-Hartree-Fock (DHF) approximation, the core orbitals are calculated using the traditional finite-difference method. Then, the valence orbitals of the ground and excited states are calculated using the DHF potential built from the core orbitals. In the second-quantized form, the Cs multi-electron state wave functions $\psi_{j,m}$ can be expressed approximately as

$$|\psi_{n_v,j_v,m_v}\rangle \equiv \psi_v = a_v^\dagger |0_c\rangle \,, \tag{5.11}$$

where $a_v^\dagger$ is the creation operator, 0_c stands for the core, and the index v specifies the valence electron orbital. Then, any one-body operator $Z = \sum_{i,j} Z_{i,j} : a_i^\dagger a_j :$ where "::" denotes the normal form of operator string acting on the multi-electron state wave function can be evaluated using the Wick's theorem

$$\begin{aligned} \sum_{i,j} \quad & Z_{ij} \quad : a_i^\dagger a_j :: a_v^\dagger : |0_c\rangle \\ = \quad & (\sum_{mb} Z_{mb} a_m^\dagger a_b a_v^\dagger + \sum_m Z_{mv} a_m^\dagger)|0_c\rangle \,. \end{aligned} \tag{5.12}$$

Here, a, b stand for core, n,m,w,v stand for the valence electrons, and i, j, stand for both valence and core orbitals. Similarly, the operator P acting on the bra $\langle 0_c|a_w$

can be written as

$$\langle 0_c|a_w P = \langle 0_c|(\sum_{an} P_{an} a_w a_a^\dagger a_n + \sum_n P_{wn} a_n)\,. \tag{5.13}$$

If we set operators $P = \hat{\boldsymbol{\varepsilon}}\cdot\boldsymbol{D}$, and $Z = \hat{\boldsymbol{e}}\cdot\boldsymbol{D}$, then the second-order Stark-induced transition amplitude can be built from a combination of these two operators, and the resolvent operator $\hat{R}_{v(w)} = \frac{1}{\epsilon_{v(w)} - H_0}$

$$a^{(2)}_{w\to v} = \langle 0_c|a_w(P\hat{R}_w Z + Z\hat{R}_v P)a_v^\dagger|0_c\rangle\,. \tag{5.14}$$

H_0 appearing in the resolvent operator is the zeroth-order one-body meanfield Hamiltonian which can be written in the normal form as

$$H_0 = \sum_i \epsilon_i : a_i^\dagger a_i :\ . \tag{5.15}$$

It follows that for valence-electron wave function $|0_v\rangle$, the matrix element $\langle 0_v|H_0|0_v\rangle$ equals the energy of the valence electron, ϵ_v; while for the hole-state wave function $a_a|0_c\rangle$, the matrix element evaluates to the energy of the hole-state obital with an additional negative sign, $-\epsilon_a$. H_0 acting on the many-body wave functions $a_m^\dagger a_b a_v^\dagger|0_c\rangle$ and $a_m^\dagger|0_c\rangle$ evaluate to

$$\begin{aligned} H_0 a_m^\dagger a_b a_v^\dagger|0_c\rangle &= (\varepsilon_m - \varepsilon_b + \varepsilon_v)|0_c\rangle\,, \\ H_0 a_m^\dagger|0_c\rangle &= \varepsilon_m|0_c\rangle\,. \end{aligned}$$

Then the resolvent operator evaluates to $\hat{R}_{v(w)} = \sum_{a\neq v(w)} \frac{|a\rangle\langle a|}{\epsilon_{v(w)} - \epsilon_a}$ similar to Eq. (3.19). By combining the evaluated re-solvent operator with the following in-

termediate results

$$\begin{aligned}\langle 0_c|a_w a_a^\dagger a_n a_m^\dagger a_b a_v^\dagger|0_c\rangle &= \delta_{ab}\delta_{wv}\delta_{mn} - \delta_{ab}\delta_{wm}\delta_{nv}\,,\\ \langle 0_c|a_n a_m^\dagger|0_c\rangle &= \delta_{nm}\,,\end{aligned}$$

the Stark-induced transition amplitude, Eq. (5.14) can be broken into three contributions: $a^{(2)}_{\rm core}$(core), $a^{(2)}_{\rm valence}$(valence), and $a^{(2)}_{\rm CV}$ (core-valence)

$$a^{(2)}_{w\to v} = \delta_{wv}a^{(2)}_{\rm core} + a^{(2)}_{\rm CV} + a^{(2)}_{\rm valence}\,, \tag{5.16}$$

where

$$\begin{aligned}a^{(2)}_{\rm core} &= \sum_{bm}\frac{P_{bm}Z_{mb}+Z_{bm}P_{mb}}{\varepsilon_b-\varepsilon_m}\,,\\ a^{(2)}_{\rm CV} &= \sum_{b}\left[\frac{Z_{wb}P_{bv}}{\varepsilon_v-\varepsilon_b}+\frac{P_{wb}Z_{bv}}{\varepsilon_w-\varepsilon_b}\right]\,,\\ a^{(2)}_{\rm valence} &= \sum_{m\neq v}\frac{Z_{wm}P_{mv}}{\varepsilon_v-\varepsilon_m}+\sum_{n\neq w}\frac{P_{wn}Z_{nv}}{\varepsilon_w-\varepsilon_n}\,.\end{aligned} \tag{5.17}$$

Note that the first term in Eq. (5.16) is the core polarizability which contributes to the static polarizability ($w = v$); while for the case of transition polarizability ($w \neq v$), this term disappears. As to the Eq. (3.43), each contribution is composed of three operators, for the third-order reductions, one of the three operators is in the middle, and the other two act on the core, $|0_c\rangle$ and $\langle 0_c|$, respectively. We list the top, bottom, and the center operators in Table 5.1.

Then, as shown in Eqs. (5.12) and (5.13), the possible ket and bra representations of the multi-electron states read

bra:

$$\sum_{na} P_{an}\langle 0_c|a_w a_a^\dagger a_n + \sum_n P_{wn}\langle 0_c|a_n\,, \tag{5.18}$$

	P	Z	U
$T^1_{v\to w}$	V	$(\hat{\varepsilon}\cdot\boldsymbol{D})$	$(\hat{e}\cdot\boldsymbol{D})$
$T^2_{v\to w}$	V	$(\hat{e}\cdot\boldsymbol{D})$	$(\hat{\varepsilon}\cdot\boldsymbol{D})$
$B^1_{v\to w}$	$(\hat{\varepsilon}\cdot\boldsymbol{D})$	$(\hat{e}\cdot\boldsymbol{D})$	V
$B^2_{v\to w}$	$(\hat{e}\cdot\boldsymbol{D})$	$(\hat{\varepsilon}\cdot\boldsymbol{D})$	V
$C^1_{v\to w}$	$(\hat{\varepsilon}\cdot\boldsymbol{D})$	V	$(\hat{e}\cdot\boldsymbol{D})$
$C^2_{v\to w}$	$(\hat{e}\cdot\boldsymbol{D})$	V	$(\hat{\varepsilon}\cdot\boldsymbol{D})$

Table 5.1: The top, bottom, and center operators expressed in the one-body operators P, Z, U. The superscript "1" or "2" specifies either the first or second term.

ket:

$$\sum_{mb} U_{mb} a_m^\dagger a_b a_v^\dagger |0_c\rangle + \sum_m U_{mv} a_m^\dagger |0_c\rangle \,. \tag{5.19}$$

As in the second-order case, the intermediate results for the expectation value can be calculated using the Wick's theorem

$$\begin{aligned}
&\langle 0_c | a_w a_a^\dagger a_n : a_i^\dagger a_j : a_m^\dagger a_b a_v^\dagger |0_c\rangle = -\delta_{ib}\delta_{aj}(\delta_{mn}\delta_{wv} - \delta_{nv}\delta_{wm}) \\
&-\delta_{jv}\delta_{ba}(\delta_{ni}\delta_{wm} - \delta_{wi}\delta_{nm}) + \delta_{jm}\delta_{ba}(\delta_{wv}\delta_{ni} - \delta_{nv}\delta_{wi}) \,, \\
&\langle 0_c | a_n : a_i^\dagger a_j : a_m^\dagger |0_c\rangle = \delta_{ni}\delta_{jm} \,, \\
&\langle 0_c | a_w a_a^\dagger a_n : a_i^\dagger a_j : a_m^\dagger |0_c\rangle = \delta_{ja}(\delta_{in}\delta_{wm} - \delta_{iw}\delta_{nm}) \,, \\
&\langle 0_c | a_n : a_i^\dagger a_j : a_m^\dagger a_b a_v^\dagger |0_c\rangle = \delta_{ib}(\delta_{jm}\delta_{nv} - \delta_{nm}\delta_{jv}) \,.
\end{aligned} \tag{5.20}$$

With the aid of the above intermediate results, the matrix elements built from

Eqs. (5.18) and (5.19) can be written as

$$
\begin{aligned}
& \sum_{namb\,ij} P_{an} Z_{ij} U_{mb} \langle 0_c | a_w a_a^\dagger a_n : a_i^\dagger a_j : a_m^\dagger a_b a_v^\dagger | 0_c \rangle \\
= \; & -\delta_{wv} \sum_{bna} P_{an} U_{nb} Z_{ba} + \sum_{ba} U_{wb} Z_{ba} P_{av} - \sum_{an} U_{wa} P_{an} Z_{nv} \\
+ \; & \sum_{an} P_{an} U_{na} Z_{wv} + \delta_{wv} \sum_{anm} P_{an} Z_{nm} U_{ma} - \sum_{am} Z_{wm} U_{ma} P_{av} \,, \qquad (5.21) \\
& \sum_{nmij} P_{wn} Z_{ij} U_{mv} \langle 0_c | a_n : a_i^\dagger a_j : a_m^\dagger | 0_c \rangle \\
= \; & \sum_{nm} P_{wn} Z_{nm} U_{mv} \,, \qquad (5.22) \\
& \sum_{namij} P_{an} Z_{ij} U_{mv} \langle 0_c | a_w a_a^\dagger a_n : a_i^\dagger a_j : a_m^\dagger | 0_c \rangle \\
= \; & \sum_{an} P_{an} U_{wv} Z_{na} - \sum_{an} Z_{wa} P_{an} U_{nv} \,, \qquad (5.23) \\
& \sum_{nmbij} P_{wn} Z_{ij} U_{mb} \langle 0_c | a_n : a_i^\dagger a_j : a_m^\dagger a_b a_v^\dagger | 0_c \rangle \\
= \; & \sum_{bm} P_{wv} U_{mb} Z_{bm} - \sum_{bm} P_{wm} U_{mb} Z_{bv} \,. \qquad (5.24)
\end{aligned}
$$

Applying operators P, Z, U showed in table 5.1 and applying Eqs. (5.21), (5.22), (5.23), and (5.24), we obtain the full expressions of the top, bottom, and center contributions: Eqs. (5.25), (5.26), (5.27); while the residual contribution $N_{v\to w}$ is handled separately. We focus on the terms with square brackets in our calculation. The remaining terms without square brackets have at least one of the following three aspects: First, it might have a factor δwv which requires initial state to be same as the final state. Next, it might contain the operator $\boldsymbol{D}_{vw}$ which is forbidden for the case, $j_v = j_w$. Last, it might include a denominator equal to 0 which violates perturbation theory so that we simply remove these terms. The sub-indices categorize the effective terms in Eqs. (3.43), and show whether those terms belong to the top, bottom, center, or residual contributions.

$$
\begin{aligned}
&T_{v\to w}\\
=&-\delta_{wv}\sum_{bna}\frac{V_{an}(\hat{\boldsymbol{e}}\cdot\boldsymbol{D}_{nb})(\hat{\boldsymbol{\varepsilon}}\cdot\boldsymbol{D}_{ba})}{(\varepsilon_a-\varepsilon_n)(\varepsilon_b-\varepsilon_n)}+\left[\sum_{ba}\frac{(\hat{\boldsymbol{e}}\cdot\boldsymbol{D}_{wb})(\hat{\boldsymbol{\varepsilon}}\cdot\boldsymbol{D}_{ba})V_{av}}{(\varepsilon_a-\varepsilon_v)(\varepsilon_b-\varepsilon_w)}\right]_{B_2}\\
&+\left[-\sum_{an}\frac{(\hat{\boldsymbol{e}}\cdot\boldsymbol{D}_{wa})V_{an}(\hat{\boldsymbol{\varepsilon}}\cdot\boldsymbol{D}_{nv})}{(\varepsilon_a-\varepsilon_n)(\varepsilon_a-\varepsilon_w)}\right]_{C_2}+(\hat{\boldsymbol{\varepsilon}}\cdot\boldsymbol{D}_{wv})\sum_{an}\frac{V_{an}(\hat{\boldsymbol{e}}\cdot\boldsymbol{D}_{na})}{(\varepsilon_a-\varepsilon_n)(\varepsilon_a-\varepsilon_n)}\\
&+\delta_{wv}\sum_{anm}\frac{V_{an}(\hat{\varepsilon}\cdot\boldsymbol{D}_{am})(\hat{\boldsymbol{e}}\cdot\boldsymbol{D}_{ma})}{(\varepsilon_a-\varepsilon_n)(\varepsilon_a-\varepsilon_m)}+\left[-\sum_{am}\frac{(\hat{\boldsymbol{\varepsilon}}\cdot\boldsymbol{D}_{wm})(\hat{\boldsymbol{e}}\cdot\boldsymbol{D}_{ma})V_{av}}{(\varepsilon_a-\varepsilon_v)(\varepsilon_a-\varepsilon_m)}\right]_{B_1}\\
&+\left[\sum_{nm}\frac{V_{wn}(\hat{\boldsymbol{\varepsilon}}\cdot\boldsymbol{D}_{nm})(\hat{\boldsymbol{e}}\cdot\boldsymbol{D}_{mv})}{(\varepsilon_v-\varepsilon_n)(\varepsilon_v-\varepsilon_m)}\right]_{T_1}+\sum_{an}\frac{V_{an}(\hat{\boldsymbol{e}}\cdot\boldsymbol{D}_{wv})(\hat{\boldsymbol{\varepsilon}}\cdot\boldsymbol{D}_{na})}{(\varepsilon_a-\varepsilon_n)(\varepsilon_v-\varepsilon_w)}\\
&+\left[-\sum_{an}\frac{(\hat{\boldsymbol{\varepsilon}}\cdot\boldsymbol{D}_{wa})V_{an}(\hat{\boldsymbol{e}}\cdot D_{nv})}{(\varepsilon_a-\varepsilon_n)(\varepsilon_v-\varepsilon_n)}\right]_{C_1}+\left[V_{wv}\sum_{bm}\frac{(\hat{\boldsymbol{e}}\cdot\boldsymbol{D}_{mb})(\hat{\boldsymbol{\varepsilon}}\cdot\boldsymbol{D}_{bm})}{(\varepsilon_w-\varepsilon_v)(\varepsilon_b-\varepsilon_m)}\right]_{N_2}\\
&+\left[-\sum_{bm}\frac{V_{wm}(\hat{\boldsymbol{e}}\cdot\boldsymbol{D}_{mb})(\hat{\boldsymbol{\varepsilon}}\cdot\boldsymbol{D}_{bv})}{(\varepsilon_w-\varepsilon_m)(\varepsilon_b-\varepsilon_m)}\right]_{T_2}-\delta_{wv}\sum_{bna}\frac{V_{an}(\hat{\boldsymbol{\varepsilon}}\cdot\boldsymbol{D}_{nb})(\hat{\boldsymbol{e}}\cdot\boldsymbol{D}_{ba})}{(\varepsilon_a-\varepsilon_n)(\varepsilon_w-\varepsilon_v+\varepsilon_b-\varepsilon_n)}\\
&+\left[\sum_{ba}\frac{(\hat{\boldsymbol{\varepsilon}}\cdot\boldsymbol{D}_{wb})(\hat{\boldsymbol{e}}\cdot\boldsymbol{D}_{ba})V_{av}}{(\varepsilon_a-\varepsilon_v)(\varepsilon_b-\varepsilon_v)}\right]_{B_1}+\left[-\sum_{an}\frac{(\hat{\boldsymbol{\varepsilon}}\cdot\boldsymbol{D}_{wa})V_{an}(\hat{\boldsymbol{e}}\cdot\boldsymbol{D}_{nv})}{(\varepsilon_a-\varepsilon_n)(\varepsilon_a-\varepsilon_v)}\right]_{C_1}\\
&+(\hat{\boldsymbol{e}}\cdot\boldsymbol{D}_{wv})\sum_{an}\frac{V_{an}(\hat{\boldsymbol{\varepsilon}}\cdot\boldsymbol{D}_{na})}{(\varepsilon_a-\varepsilon_n)(\varepsilon_w-\varepsilon_v+\varepsilon_a-\varepsilon_n)}+\delta_{wv}\sum_{anm}\frac{V_{an}(\hat{\boldsymbol{e}}\cdot\boldsymbol{D}_{am})(\hat{\boldsymbol{\varepsilon}}\cdot\boldsymbol{D}_{ma})}{(\varepsilon_a-\varepsilon_n)(\varepsilon_a-\varepsilon_m)}\\
&+\left[-\sum_{am}\frac{(\hat{\boldsymbol{e}}\cdot\boldsymbol{D}_{wm})(\hat{\boldsymbol{\varepsilon}}\cdot\boldsymbol{D}_{ma})V_{av}}{(\varepsilon_a-\varepsilon_v)(\varepsilon_a-\varepsilon_m+\varepsilon_w-\varepsilon_v)}\right]_{B_2}+\left[\sum_{nm}\frac{V_{wn}(\hat{\boldsymbol{e}}\cdot\boldsymbol{D}_{nm})(\hat{\boldsymbol{\varepsilon}}\cdot\boldsymbol{D}_{mv})}{(\varepsilon_w-\varepsilon_n)(\varepsilon_w-\varepsilon_m)}\right]_{T_2}\\
&+(\hat{\boldsymbol{\varepsilon}}\cdot\boldsymbol{D}_{wv})\sum_{an}\frac{V_{an}(\hat{\boldsymbol{e}}\cdot\boldsymbol{D}_{na})}{(\varepsilon_a-\varepsilon_n)(\varepsilon_w-\varepsilon_n)}-\sum_{an}\frac{(\hat{\boldsymbol{e}}\cdot\boldsymbol{D}_{wa})V_{an}(\hat{\boldsymbol{\varepsilon}}\cdot\boldsymbol{D}_{nv})}{(\varepsilon_a-\varepsilon_n)(\varepsilon_m-\varepsilon_m)}\\
&+\left[\sum_{bm}\frac{V_{wv}(\hat{\boldsymbol{\varepsilon}}\cdot\boldsymbol{D}_{mb})(\hat{\boldsymbol{e}}\cdot\boldsymbol{D}_{bm})}{(\varepsilon_w-\varepsilon_v)(\varepsilon_n-\varepsilon_m)}\right]_{N_1}+\left[-\sum_{bm}\frac{V_{wm}(\hat{\boldsymbol{\varepsilon}}\cdot\boldsymbol{D}_{mb})(\hat{\boldsymbol{e}}\cdot\boldsymbol{D}_{bv})}{(\varepsilon_w-\varepsilon_m)(\varepsilon_b-\varepsilon_m+\varepsilon_w-\varepsilon_v)}\right]_{T_1}.
\end{aligned}
\tag{5.25}
$$

$$
\begin{aligned}
B_{v\to w} = &-\delta_{wv}\sum_{bna}\frac{(\hat{\boldsymbol{\varepsilon}}\cdot\boldsymbol{D}_{an})V_{nb}(\hat{\boldsymbol{e}}\cdot\boldsymbol{D}_{ba})}{(\varepsilon_b-\varepsilon_n)(\varepsilon_a-\varepsilon_n)}+\left[\sum_{ba}\frac{V_{wb}(\hat{\boldsymbol{e}}\cdot\boldsymbol{D}_{ba})(\hat{\boldsymbol{\varepsilon}}\cdot\boldsymbol{D}_{av})}{(\varepsilon_a-\varepsilon_w)(\varepsilon_b-\varepsilon_w)}\right]_{T_2}\\
&+\left[-\sum_{an}\frac{V_{wa}(\hat{\boldsymbol{\varepsilon}}\cdot\boldsymbol{D}_{an})(\hat{\boldsymbol{e}}\cdot\boldsymbol{D}_{nv})}{(\varepsilon_a-\varepsilon_w)(\varepsilon_v-\varepsilon_w+\varepsilon_a-\varepsilon_n)}\right]_{T_1}\\
&+(\hat{\boldsymbol{e}}\cdot\boldsymbol{D}_{wv})\sum_{an}\frac{(\hat{\boldsymbol{\varepsilon}}\cdot\boldsymbol{D}_{an})V_{na}}{(\varepsilon_a-\varepsilon_n)(\varepsilon_v-\varepsilon_w+\varepsilon_a-\varepsilon_n)}\\
&+\delta_{wv}\sum_{anm}\frac{(\hat{\boldsymbol{\varepsilon}}\cdot\boldsymbol{D}_{an})(\hat{\boldsymbol{e}}\cdot\boldsymbol{D}_{nm})V_{ma}}{(\varepsilon_a-\varepsilon_n)(\varepsilon_a-\varepsilon_m)}+\left[-\sum_{am}\frac{(\hat{\boldsymbol{e}}\cdot\boldsymbol{D}_{wm})V_{ma}(\hat{\boldsymbol{\varepsilon}}\cdot\boldsymbol{D}_{av})}{(\varepsilon_a-\varepsilon_w)(\varepsilon_a-\varepsilon_m)}\right]_{C_2}\\
&+\left[\sum_{nm}\frac{(\hat{\boldsymbol{\varepsilon}}\cdot\boldsymbol{D}_{wn})(\hat{\boldsymbol{e}}\cdot\boldsymbol{D}_{nm})V_{mv}}{(\varepsilon_v-\varepsilon_n)(\varepsilon_v-\varepsilon_m)}\right]_{B_1}+\left[\sum_{an}\frac{(\hat{\boldsymbol{\varepsilon}}\cdot\boldsymbol{D}_{an})V_{wv}(\hat{\boldsymbol{e}}\cdot\boldsymbol{D}_{na})}{(\varepsilon_v-\varepsilon_w)(\varepsilon_v-\varepsilon_w+\varepsilon_a-\varepsilon_n)}\right]_{N_1}\\
&+\left[-\sum_{an}\frac{(\hat{\boldsymbol{e}}\cdot\boldsymbol{D}_{wa})(\hat{\boldsymbol{\varepsilon}}\cdot\boldsymbol{D}_{an})V_{nv}}{(\varepsilon_v-\varepsilon_n)(\varepsilon_v-\varepsilon_w+\varepsilon_a-\varepsilon_n)}\right]_{B_2}\\
&+(\hat{\boldsymbol{\varepsilon}}\cdot\boldsymbol{D}_{wv})\sum_{bm}\frac{V_{mb}(\hat{\boldsymbol{e}}\cdot\boldsymbol{D}_{bm})}{(\varepsilon_b-\varepsilon_m)(\varepsilon_v-\varepsilon_v)}+\left[-\sum_{bm}\frac{(\hat{\boldsymbol{\varepsilon}}\cdot\boldsymbol{D}_{wm})V_{mb}(\hat{\boldsymbol{e}}\cdot\boldsymbol{D}_{bv})}{(\varepsilon_b-\varepsilon_m)(\varepsilon_v-\varepsilon_m)}\right]_{C_1}\\
&-\delta_{wv}\sum_{bna}\frac{(\hat{\boldsymbol{e}}\cdot\boldsymbol{D}_{an})V_{nb}(\hat{\boldsymbol{\varepsilon}}\cdot\boldsymbol{D}_{ba})}{(\varepsilon_b-\varepsilon_n)(\varepsilon_a-\varepsilon_n)}+\left[\sum_{ba}\frac{V_{wb}(\hat{\boldsymbol{\varepsilon}}\cdot\boldsymbol{D}_{ba})(\hat{\boldsymbol{e}}\cdot\boldsymbol{D}_{av})}{(\varepsilon_a-\varepsilon_v)(\varepsilon_b-\varepsilon_w)}\right]_{T_1}\\
&+\left[-\sum_{an}\frac{V_{wa}(\hat{\boldsymbol{e}}\cdot\boldsymbol{D}_{an})(\hat{\boldsymbol{\varepsilon}}\cdot\boldsymbol{D}_{nv})}{(\varepsilon_a-\varepsilon_w)(\varepsilon_a-\varepsilon_n)}\right]_{T_2}\\
&+\left[\sum_{an}\frac{(\hat{\boldsymbol{e}}\cdot\boldsymbol{D}_{an})V_{na}(\hat{\boldsymbol{\varepsilon}}\cdot\boldsymbol{D}_{wv})}{(\varepsilon_a-\varepsilon_n)(\varepsilon_a-\varepsilon_n)}\right]_{C_2}+\delta_{wv}\sum_{anm}\frac{(\hat{\boldsymbol{e}}\cdot\boldsymbol{D}_{an})(\hat{\boldsymbol{\varepsilon}}\cdot\boldsymbol{D}_{nm})V_{ma}}{(\varepsilon_a-\varepsilon_n)(\varepsilon_a-\varepsilon_m)}\\
&+\left[-\sum_{am}\frac{(\hat{\boldsymbol{\varepsilon}}\cdot\boldsymbol{D}_{wm})V_{ma}(\hat{\boldsymbol{e}}\cdot\boldsymbol{D}_{av})}{(\varepsilon_a-\varepsilon_v)(\varepsilon_a-\varepsilon_m)}\right]_{C_1}\\
&+\left[\sum_{nm}\frac{(\hat{\boldsymbol{e}}\cdot\boldsymbol{D}_{wn})(\hat{\boldsymbol{\varepsilon}}\cdot\boldsymbol{D}_{nm})V_{mv}}{(\varepsilon_w-\varepsilon_n)(\varepsilon_v-\varepsilon_m)}\right]_{B_2}+\left[\sum_{an}\frac{(\hat{\boldsymbol{e}}\cdot\boldsymbol{D}_{an})V_{wv}(\hat{\boldsymbol{\varepsilon}}\cdot\boldsymbol{D}_{na})}{(\varepsilon_v-\varepsilon_w)(\varepsilon_a-\varepsilon_n)}\right]_{N_2}\\
&+\left[-\sum_{an}\frac{(\hat{\boldsymbol{\varepsilon}}\cdot\boldsymbol{D}_{wa})(\hat{\boldsymbol{e}}\cdot\boldsymbol{D}_{an})V_{nv}}{(\varepsilon_v-\varepsilon_n)(\varepsilon_a-\varepsilon_n)}\right]_{B_1}\\
&+(\hat{\boldsymbol{e}}\cdot\boldsymbol{D}_{wv})\sum_{bm}\frac{V_{mb}(\hat{\boldsymbol{\varepsilon}}\cdot\boldsymbol{D}_{bm})}{(\varepsilon_b-\varepsilon_m)(\varepsilon_w-\varepsilon_v)}+\left[-\sum_{bm}\frac{(\hat{\boldsymbol{e}}\cdot\boldsymbol{D}_{wm})V_{mb}(\hat{\boldsymbol{\varepsilon}}\cdot\boldsymbol{D}_{bv})}{(\varepsilon_b-\varepsilon_m)(\varepsilon_w-\varepsilon_m)}\right]_{C_2}. \qquad (5.26)
\end{aligned}
$$

$$
\begin{aligned}
C_{v\to w} = &-\delta_{wv}\sum_{bna}\frac{(\hat{\boldsymbol{\varepsilon}}\cdot\boldsymbol{D}_{an})(\hat{\boldsymbol{e}}\cdot\boldsymbol{D}_{nb})V_{ba}}{(\varepsilon_b-\varepsilon_n)(\varepsilon_a-\varepsilon_n)} + \left[\sum_{ba}\frac{(\hat{\boldsymbol{e}}\cdot\boldsymbol{D}_{wb})V_{ba}(\hat{\boldsymbol{\varepsilon}}\cdot\boldsymbol{D}_{av})}{(\varepsilon_a-\varepsilon_w)(\varepsilon_b-\varepsilon_w)}\right]_{C_2}\\
&+\left[-\sum_{an}\frac{(\hat{\boldsymbol{e}}\cdot\boldsymbol{D}_{wa})(\hat{\boldsymbol{\varepsilon}}\cdot\boldsymbol{D}_{an})V_{nv}}{(\varepsilon_a-\varepsilon_w)(\varepsilon_v-\varepsilon_w+\varepsilon_a-\varepsilon_n)}\right]_{B_2}\\
&+\left[\sum_{an}\frac{(\hat{\boldsymbol{\varepsilon}}\cdot\boldsymbol{D}_{an})(\hat{\boldsymbol{e}}\cdot\boldsymbol{D}_{na})V_{wv}}{(\varepsilon_a-\varepsilon_n)(\varepsilon_v-\varepsilon_w+\varepsilon_a-\varepsilon_n)}\right]_{N_1} + \delta_{wv}\sum_{anm}\frac{(\hat{\boldsymbol{e}}\cdot\boldsymbol{D}_{an})V_{nm}(\hat{\boldsymbol{\varepsilon}}\cdot\boldsymbol{D}_{ma})}{(\varepsilon_a-\varepsilon_n)(\varepsilon_a-\varepsilon_m)}\\
&+\left[-\sum_{am}\frac{V_{wm}(\hat{\boldsymbol{e}}\cdot\boldsymbol{D}_{ma})(\hat{\boldsymbol{\varepsilon}}\cdot\boldsymbol{D}_{av})}{(\varepsilon_a-\varepsilon_w)(\varepsilon_a-\varepsilon_m)}\right]_{T_2} + \left[\sum_{nm}\frac{(\hat{\boldsymbol{\varepsilon}}\cdot\boldsymbol{D}_{wn})V_{nm}(\hat{\boldsymbol{e}}\cdot\boldsymbol{D}_{mv})}{(\varepsilon_v-\varepsilon_n)(\varepsilon_v-\varepsilon_m)}\right]_{C_1}\\
&+(\hat{\boldsymbol{e}}\cdot\boldsymbol{D}_{wv})\sum_{an}\frac{(\hat{\boldsymbol{\varepsilon}}\cdot\boldsymbol{D}_{an})V_{na}}{(\varepsilon_v-\varepsilon_w)(\varepsilon_v-\varepsilon_w+\varepsilon_a-\varepsilon_n)}\\
&+\left[-\sum_{an}\frac{V_{wa}(\hat{\boldsymbol{\varepsilon}}\cdot\boldsymbol{D}_{an})(\hat{\boldsymbol{e}}\cdot\boldsymbol{D}_{nv})}{(\varepsilon_v-\varepsilon_n)(\varepsilon_v-\varepsilon_w+\varepsilon_a-\varepsilon_n)}\right]_{T_1} + (\hat{\boldsymbol{\varepsilon}}\cdot\boldsymbol{D}_{wv})\sum_{bm}\frac{(\hat{\boldsymbol{e}}\cdot\boldsymbol{D}_{mb})V_{bm}}{(\varepsilon_b-\varepsilon_m)(\varepsilon_v-\varepsilon_v)}\\
&+\left[-\sum_{bm}\frac{(\hat{\boldsymbol{\varepsilon}}\cdot\boldsymbol{D}_{wm})(\hat{\boldsymbol{e}}\cdot\boldsymbol{D}_{mb})V_{bv}}{(\varepsilon_b-\varepsilon_m)(\varepsilon_v-\varepsilon_m)}\right]_{B_1} - \delta_{wv}\sum_{bna}\frac{(\hat{\boldsymbol{e}}\cdot\boldsymbol{D}_{an})(\hat{\boldsymbol{\varepsilon}}\cdot\boldsymbol{D}_{nb})V_{ba}}{(\varepsilon_w-\varepsilon_v+\varepsilon_b-\varepsilon_n)(\varepsilon_a-\varepsilon_n)}\\
&+\left[\sum_{ba}\frac{(\hat{\boldsymbol{\varepsilon}}\cdot\boldsymbol{D}_{wb})V_{ba}(\hat{\boldsymbol{e}}\cdot\boldsymbol{D}_{av})}{(\varepsilon_a-\varepsilon_v)(\varepsilon_b-\varepsilon_v)}\right]_{C_1} + \left[-\sum_{an}\frac{(\hat{\boldsymbol{\varepsilon}}\cdot\boldsymbol{D}_{wa})(\hat{\boldsymbol{e}}\cdot\boldsymbol{D}_{an})V_{nv}}{(\varepsilon_a-\varepsilon_w)(\varepsilon_a-\varepsilon_n)}\right]_{B_1}\\
&+\left[\sum_{an}\frac{(\hat{\boldsymbol{e}}\cdot\boldsymbol{D}_{an})(\hat{\boldsymbol{\varepsilon}}\cdot\boldsymbol{D}_{na})V_{wv}}{(\varepsilon_a-\varepsilon_n)(\varepsilon_w-\varepsilon_v+\varepsilon_a-\varepsilon_n)}\right]_{N_2} + \delta_{wv}\sum_{anm}\frac{(\hat{\boldsymbol{\varepsilon}}\cdot\boldsymbol{D}_{an})V_{nm}(\hat{\boldsymbol{e}}\cdot\boldsymbol{D}_{ma})}{(\varepsilon_a-\varepsilon_n)(\varepsilon_a-\varepsilon_m)}\\
&+\left[-\sum_{am}\frac{V_{wm}(\hat{\boldsymbol{\varepsilon}}\cdot\boldsymbol{D}_{ma})(\hat{\boldsymbol{e}}\cdot\boldsymbol{D}_{av})}{(\epsilon_a-\epsilon_v)(\varepsilon_a-\varepsilon_m+\varepsilon_w-\varepsilon_v)}\right]_{T_1} + \left[\sum_{nm}\frac{(\hat{\boldsymbol{e}}\cdot\boldsymbol{D}_{wn})V_{nm}(\hat{\boldsymbol{\varepsilon}}\cdot\boldsymbol{D}_{mv})}{(\varepsilon_w-\varepsilon_n)(\varepsilon_w-\varepsilon_m)}\right]_{C_2}\\
&+(\hat{\boldsymbol{\varepsilon}}\cdot\boldsymbol{D}_{wv})\sum_{an}\frac{(\hat{\boldsymbol{e}}\cdot\boldsymbol{D}_{an})V_{na}}{(\varepsilon_w-\varepsilon_n)(\varepsilon_a-\varepsilon_n)} + \left[-\sum_{an}\frac{V_{wa}(\hat{\boldsymbol{e}}\cdot\boldsymbol{D}_{an})(\hat{\boldsymbol{\varepsilon}}\cdot\boldsymbol{D}_{nv})}{(\varepsilon_m-\varepsilon_m)(\varepsilon_a-\varepsilon_n)}\right]_{T_2}\\
&+(\hat{\boldsymbol{e}}\cdot\boldsymbol{D}_{wv})\sum_{bm}\frac{(\hat{\boldsymbol{\varepsilon}}\cdot\boldsymbol{D}_{mb})V_{bm}}{(\varepsilon_b-\varepsilon_m)(\varepsilon_w-\varepsilon_v)}\\
&+\left[-\sum_{bm}\frac{(\hat{\boldsymbol{e}}\cdot\boldsymbol{D}_{wm})(\hat{\boldsymbol{\varepsilon}}\cdot\boldsymbol{D}_{mb})V_{bv}}{(\varepsilon_w-\varepsilon_v+\varepsilon_b-\varepsilon_m)(\varepsilon_w-\varepsilon_m)}\right]_{B_2}. \qquad (5.27)
\end{aligned}
$$

With the aid of the identity $\frac{1}{(A+B)A}+\frac{1}{(A+B)B}=\frac{1}{AB}$, the newly combined top,

bottom, center, and residual-like terms denoted as T', B', C', N' read

$$
\begin{aligned}
T' &= \sum_{T_1,T_2} [...]_{T_1} + [...]_{T_2} = \sum_{ij} \left[\frac{V_{wi}(\hat{\boldsymbol{\varepsilon}} \cdot \boldsymbol{D}_{ij})(\hat{\boldsymbol{e}} \cdot \boldsymbol{D}_{jv})}{(\varepsilon_w - \varepsilon_i)(\varepsilon_v - \varepsilon_j)} + \frac{V_{wi}(\hat{\boldsymbol{e}} \cdot \boldsymbol{D}_{ij})(\hat{\boldsymbol{\varepsilon}} \cdot \boldsymbol{D}_{jv})}{(\varepsilon_w - \varepsilon_i)(\varepsilon_w - \varepsilon_j)} \right] , \\
B' &= \sum_{B_1,B_2} [...]_{B_1} + [...]_{B_2} = \sum_{ij} \left[\frac{(\hat{\boldsymbol{\varepsilon}} \cdot \boldsymbol{D}_{wi})(\hat{\boldsymbol{e}} \cdot \boldsymbol{D}_{ij})V_{jv}}{(\varepsilon_v - \varepsilon_i)(\varepsilon_v - \varepsilon_j)} + \frac{(\hat{\boldsymbol{e}} \cdot \boldsymbol{D}_{wi})(\hat{\boldsymbol{\varepsilon}} \cdot \boldsymbol{D}_{ij})V_{jv}}{(\varepsilon_w - \varepsilon_i)(\varepsilon_v - \varepsilon_j)} \right] , \\
C' &= \sum_{C_1,C_2} [...]_{C_1} + [...]_{C_2} = \sum_{ij} \left[\frac{(\hat{\boldsymbol{\varepsilon}} \cdot \boldsymbol{D}_{wi})V_{ij}(\hat{e} \cdot \boldsymbol{D}_{jv})}{(\varepsilon_v - \varepsilon_i)(\varepsilon_v - \varepsilon_j)} + \frac{(\hat{e} \cdot \boldsymbol{D}_{wi})V_{ij}(\hat{\boldsymbol{\varepsilon}} \cdot \boldsymbol{D}_{jv})}{(\varepsilon_w - \varepsilon_i)(\varepsilon_w - \varepsilon_j)} \right] , \\
N' &= \sum_{N_1,N_2} [...]_{N_1} + [...]_{N_2} = 0 \, .
\end{aligned} \tag{5.28}
$$

Note that T', B' and C' include four channels of intermediate states, (valence, valence), (valence, core), (core, valence) and (core, core). Furthermore, the resulting combination of residual terms generated from the top, bottom and center contributions denoted as N' equals 0. As to the second-order case, the residual amplitude $N_{v\to w}$ reads

$$
\begin{aligned}
N_{v\to w} &= -\Bigg[\delta_{wv} \sum_{an} \{ V_{vv} \frac{(\hat{\boldsymbol{\varepsilon}} \cdot \boldsymbol{D}_{an})(\hat{e} \cdot \boldsymbol{D}_{na})}{(\varepsilon_b - \varepsilon_m)^2} + V_{ww} \frac{(\hat{\boldsymbol{e}} \cdot \boldsymbol{D}_{an})(\hat{\boldsymbol{\varepsilon}} \cdot \boldsymbol{D}_{na})}{(\varepsilon_b - \varepsilon_m)^2} \} \\
&\quad \sum_{a} \{ -V_{vv} \frac{(\hat{e} \cdot \boldsymbol{D}_{wa})(\hat{\boldsymbol{\varepsilon}} \cdot \boldsymbol{D}_{av})}{(\varepsilon_b - \varepsilon_v)^2}) - V_{ww} \frac{(\hat{\boldsymbol{\varepsilon}} \cdot \boldsymbol{D}_{av})(\hat{\boldsymbol{e}} \cdot \boldsymbol{D}_{av})}{(\varepsilon_b - \varepsilon_w)^2} \\
&+ \quad V_{vv} \frac{(\hat{\boldsymbol{\varepsilon}} \cdot \boldsymbol{D}_{wn})(\hat{\boldsymbol{e}} \cdot \boldsymbol{D}_{nv})}{(\varepsilon_w - \varepsilon_n)^2} + V_{ww} \frac{(\hat{\boldsymbol{e}} \cdot \boldsymbol{D}_{wn})(\hat{\boldsymbol{\varepsilon}} \cdot \boldsymbol{D}_{nv})}{(\varepsilon_v - \varepsilon_n)^2} \} \Bigg] ,
\end{aligned}
$$

where the first two terms equals 0 leaving the remaining terms same as Eq. 3.53.

5.4 The calculation of combined Clesbsh-Gordan coefficients

The goal of this appendix is to derive the combined Clesbsh- Gordan coefficients. In atomic physics, the electron orbitals are generally represented in the spherical coor-

dinate system. Therefore, when evaluating a matrix element of a vector operator, it is more natural to represent the operator in helicity basis. The Pauli spin operator $\boldsymbol{\sigma}$ in the helicity basis reads

$$\boldsymbol{\sigma} = \sum_{k=-1,\,0,\,1} (-1)^k \sigma_{-k} \hat{e}_k \,, \tag{5.29}$$

where the helicity basis vectors, $\hat{e}_{-1}$, $\hat{e}_0$, $\hat{e}_1$ can be expressed in the Cartesian basis as

$$\begin{aligned} \hat{e}_{-1} &= -\frac{1}{\sqrt{2}}(\hat{x} - \hat{y}), \\ \hat{e}_1 &= \frac{1}{\sqrt{2}}(\hat{x} + \hat{y}), \\ \hat{e}_0 &= \hat{z}. \end{aligned} \tag{5.30}$$

Applying the Wigner-Eckart theorem, we obtain

$$\begin{aligned} &\langle F_f, M_{F_f} | \boldsymbol{\sigma} | F_i, M_{F_i} \rangle = (-1)^{F_f - M_{F_f}} \frac{1}{\sqrt{6}} \times \\ &(-1)^{I+S+F_i+1} \sqrt{[F_f, F_i]} \begin{Bmatrix} 1/2 & F_f & I \\ F_i & 1/2 & 1 \end{Bmatrix} \\ \times \quad &\left\{ \frac{1}{\sqrt{2}} \left[\begin{pmatrix} F_f & 1 & F_i \\ -M_{F_f} & -1 & M_{F_i} \end{pmatrix} - \begin{pmatrix} F_f & 1 & F_i \\ -M_{F_f} & 1 & M_{F_i} \end{pmatrix} \right] \hat{x} \right. \\ + \quad &\frac{i}{\sqrt{2}} \left[\begin{pmatrix} F_f & 1 & F_i \\ -M_{F_f} & -1 & M_{F_i} \end{pmatrix} + \begin{pmatrix} F_f & 1 & F_i \\ -M_{F_f} & 1 & M_{F_i} \end{pmatrix} \right] \hat{y} \\ + \quad &\left. \begin{pmatrix} F_f & 1 & F_i \\ -M_{F_f} & 0 & M_{F_i} \end{pmatrix} \hat{z} \right\} . \end{aligned} \tag{5.31}$$

Note that whether these 3-j symbols are zero-valued or not depends on the initial and final state magnetic quantum numbers M_{F_i} and M_{F_f}, and we list the non-vanishing coefficients for the three cases $M_{F_f} = M_{F_i}$, $M_{F_f}+1 = M_{F_i}$ and $M_{F_f}-1 = M_{F_i}$,

$$C^{F_f M_f}_{F_i M_{F_i}} = \begin{pmatrix} F_f & 1 & F_i \\ -M_{F_f} & 0 & M_{F_i} \end{pmatrix} (-1)^{I+S+F_i+1} \sqrt{[F_f, F_i]} \begin{Bmatrix} 1/2 & F_f & I \\ F_i & 1/2 & 1 \end{Bmatrix} \frac{1}{\sqrt{6}}, \tag{5.32a}$$

$$C^{F_f M_{F_f}}_{F_i M_{F_f}+1} = \frac{1}{\sqrt{2}} \begin{pmatrix} F_f & 1 & F_i \\ -M_{F_f} & -1 & M_{F_i} \end{pmatrix} (-1)^{I+S+F_i+1} \sqrt{[F_f, F_i]} \begin{Bmatrix} 1/2 & F_f & I \\ F_i & 1/2 & 1 \end{Bmatrix} \frac{1}{\sqrt{6}}, \tag{5.32b}$$

$$C^{F_f M_{F_f}}_{F_i M_{F_f}-1} = \frac{1}{\sqrt{2}} \begin{pmatrix} F_f & 1 & F \\ -M_{F_f} & 1 & M_{F_i} \end{pmatrix} (-1)^{I+S+F_i+1} \sqrt{[F_f, F_i]} \begin{Bmatrix} 1/2 & F_f & I \\ F_i & 1/2 & 1 \end{Bmatrix} \frac{1}{\sqrt{6}}, \tag{5.32c}$$

where $C^{F_f M_f}_{F_i M_{F_i}}$, $C^{F_f M_{F_f}}_{F_i M_{F_f}+1}$, and $C^{F_f M_{F_f}}_{F_i M_{F_f}-1}$ are the combinations of the 3j- and 6j-symbols.

Applying the Eqs. (5.32a),(5.32b), and (5.32c), Eq. (5.31) can be rewritten as

$$\begin{aligned} \langle F_f,\, M_{F_f}|\boldsymbol{\sigma}|F_i,\, M_{F_i}\rangle &= (-1)^{F_f - M_{F_f}} \left[\left(C^{F_f M_f}_{F_i M_{F_f}+1} - C^{F_f M_f}_{F_i M_{F_f}-1} \right) \hat{x} \right. \\ &+ \left. i \left(C^{F_f M_f}_{F_i M_{F_f}+1} + C^{F_f M_f}_{F_i M_{F_f}-1} \right) \hat{y} + C^{F_f M_f}_{F_i M_{F_i}} \hat{z} \right]. \end{aligned} \tag{5.33}$$

Bibliography

[1] Charles Schwartz. Theory of Hyperfine Structure. *Physical Review*, 97(2):380–395, 1 1955. ISSN 0031-899X. doi: 10.1103/PhysRev.97.380. URL https://doi.org/10.1103/PhysRev.97.380https://link.aps.org/doi/10.1103/PhysRev.97.380.

[2] NJ Stone. Table of nuclear magnetic dipole and electric quadrupole moments. *At. Data Nucl. Data Tables*, 90(1):75–176, 2005.

[3] Gladys H. Fuller. Nuclear Spins and Moments, 1976. ISSN 15297845.

[4] George Toh, Amy Damitz, Nathan Glotzbach, Jonah Quirk, I. C. Stevenson, J. Choi, M. S. Safronova, and D. S. Elliott. Electric dipole matrix elements for the $6p\ ^2P_J \rightarrow 7s\ ^2S_{1/2}$ transition in atomic cesium. pages 32–34, 2019. URL http://arxiv.org/abs/1901.00480.

[5] H. B. Tran Tan and A. Derevianko. Precision theoretical determination of electric dipole matrix elements in atomic cesium, 2023.

[6] V. A. Dzuba, V. V. Flambaum, and O. P. Sushkov. Polarizabilities and parity nonconservation in the cs atom and limits on the deviation from the standard electroweak model. *Phys. Rev. A*, 56:R4357–R4360, Dec 1997. doi: 10.1103/PhysRevA.56.R4357. URL https://link.aps.org/doi/10.1103/PhysRevA.56.R4357.

[7] M. S. Safronova, W. R. Johnson, and A. Derevianko. Relativistic many-body calculations of energy levels, hyperfine constants, electric-dipole matrix elements, and static polarizabilities for alkali-metal atoms. *Phys. Rev. A*, 60:4476–4487, Dec 1999. doi: 10.1103/PhysRevA.60.4476. URL https://link.aps.org/doi/10.1103/PhysRevA.60.4476.

[8] A. A. Vasilyev, I. M. Savukov, M. S. Safronova, and H. G. Berry. Measurement of the $6s - 7p$ transition probabilities in atomic cesium and a revised value for the weak charge Q_W. *Phys. Rev. A*, 66:020101, Aug

2002. doi: 10.1103/PhysRevA.66.020101. URL https://link.aps.org/doi/10.1103/PhysRevA.66.020101.

[9] V. A. Dzuba, V. V. Flambaum, and J. S. M. Ginges. High-precision calculation of parity nonconservation in cesium and test of the standard model. *Phys. Rev. D*, 66:076013, Oct 2002. doi: 10.1103/PhysRevD.66.076013. URL https://link.aps.org/doi/10.1103/PhysRevD.66.076013.

[10] S. C. Bennett and C. E. Wieman. Measurement of the $6s - 7p$ transition polarizability in atomic cesium and an improved test of the standard model. *Phys. Rev. Lett.*, 82:2484–2487, Mar 1999. doi: 10.1103/PhysRevLett.82.2484. URL https://link.aps.org/doi/10.1103/PhysRevLett.82.2484.

[11] V A Dzuba and V V Flambaum. Off-diagonal hyperfine interaction and parity nonconservation in cesium. *PHYSICAL REVIEW A*, 62(5), 10 2000. doi: 10.1103/PhysRevA.62.052101. URL https://link.aps.org/doi/10.1103/PhysRevA.62.052101.

[12] Alok K. Singh, D. Angom, and Vasant Natarajan. Observation of the nuclear magnetic octupole moment of ^{173}Yb from precise measurements of the hyperfine structure in the $^3P_2$ state. *Physical Review A*, 87(1): 012512, jan 2013. ISSN 1050-2947. doi: 10.1103/PhysRevA.87.012512. URL http://link.aps.org/doi/10.1103/PhysRevA.87.012512.

[13] Vladislav Gerginov, Andrei Derevianko, and Carol E Tanner. Observation of the nuclear magnetic octupole moment of ^{133}Cs. *Phys. Rev. Lett.*, 91(7): 72501, aug 2003. ISSN 0031-9007. doi: 10.1103/PhysRevLett.91.072501.

[14] S. A. Williams. Magnetic octupole moments of axially symmetric deformed nuclei. *Physical Review*, 125(1):340–346, 1962. ISSN 0031899X. doi: 10.1103/PhysRev.125.340.

[15] Vladislav Gerginov, Carol E Tanner, and W R Johnson. Observation of the nuclear magnetic octupole moment of ^{87}Rb from spectroscopic measurements of hyperfine intervals. *Canadian Journal of Physics*, 87(1): 101–104, 2009. ISSN 00084204. doi: 10.1139/P08-145.

[16] T. G. Eck and P. Kusch. Hfs of the $5\ ^2p_{\frac{3}{2}}$ state of ^{115}In and ^{113}In: Octupole interactions in the stable isotopes of indium. *Phys. Rev.*, 106:958–964, Jun 1957. doi: 10.1103/PhysRev.106.958. URL https://link.aps.org/doi/10.1103/PhysRev.106.958.

[17] Nicholas C. Lewty, Boon Leng Chuah, Radu Cazan, Murray D. Barrett, and B. K. Sahoo. Experimental determination of the nuclear magnetic octupole moment of $^{137}Ba^{+}$ ion. *Physical Review A - Atomic, Molecular, and Optical Physics*, 88(1):1–8, 2013. ISSN 10502947. doi: 10.1103/PhysRevA.88.012518.

[18] P. J. Unsworth. Nuclear dipole, quadrupole and octupole moments of ^{155}Gd by atomic beam magnetic resonance. *Journal of Physics B: Atomic and Molecular Physics*, 2(1):122–133, 1969. ISSN 00223700. doi: 10.1088/0022-3700/2/1/318.

[19] W. Dankwort, J. Ferch, and H. Gebauer. Hexadecapole interaction in the atomic ground state of ^{165}Ho. *Zeitschrift für Physik*, 267(3):229–237, Jun 1974. ISSN 0044-3328. doi: 10.1007/BF01669225. URL `https://doi.org/10.1007/BF01669225`.

[20] W. J. Childs. M1, E2, and M3 hyperfine structure and nuclear moment ratios for $^{151,153}Eu$. *Phys. Rev. A*, 44:1523–1530, Aug 1991. doi: 10.1103/PhysRevA.44.1523. URL `https://link.aps.org/doi/10.1103/PhysRevA.44.1523`.

[21] W G Jin, M Wakasugi, T T Inamura, T Murayama, T Wakui, H Katsuragawa, T Ariga, T Ishizuka, and I Sugai. Laser-rf double-resonance spectroscopy of $^{177,179}hf$. *Phys. Rev. A*, 52(1):157–164, 1995.

[22] Peter T. H. Fisk, Matthew J. Sellars, Malcolm A. Lawn, and Colin Coles. Accurate measurement of the 12.6 GHz "clock" transition in trapped $^{171}Yb^{+}$ ions. *IEEE Transactions on Ultrasolics, Ferroelectrics, and Frequency Control*, 44:344, 1997.

[23] Ye Wang, Mark Um, Junhua Zhang, Shuoming An, Ming Lyu, Jing Ning Zhang, L M Duan, Dahyun Yum, and Kihwan Kim. Single-qubit quantum memory exceeding ten-minute coherence time. *Nature Photonics*, 11(10):646–650, 2017. ISSN 17494893. doi: 10.1038/s41566-017-0007-1. URL `http://dx.doi.org/10.1038/s41566-017-0007-1`.

[24] S. Olmschenk, K. C. Younge, D. L. Moehring, D. N. Matsukevich, P. Maunz, and C. Monroe. Manipulation and detection of a trapped Yb^{+} hyperfine qubit. *Physical Review A - Atomic, Molecular, and Optical Physics*, 76(5):1–10, 2007. ISSN 10502947. doi: 10.1103/PhysRevA.76.052314.

[25] C. Figgatt, A. Ostrander, N. M. Linke, K. A. Landsman, D. Zhu, D. Maslov, and C. Monroe. Parallel entangling operations on a universal ion-trap quantum computer. *Nature*, 572:368, 2019.

[26] J. Zhang, G. Pagano, P. W. Hess, A. Kyprianidis, P. Becker, H. Kaplan, A. V. Gorshkov, Z.-X. Gong, and C. Monroe. Observation of a many-body dynamical phase transition with a 53-qubit quantum simulator. *Nature*, 551:601, 2017.

[27] K. A. Landsman, C. Figgatt, T. Schuster, N. M. Linke, B. Yoshida, N. Y. Yao, and C. Monroe. Verified quantum information scrambling. *Nature*, 567:61, 2019.

[28] K. Wright, K. M. Beck, S. Debnath, J. M. Amini, Y. Nam, N. Grzesiak, J.-S. Chen, N. C. Pisenti, M. Chmielewski, C. Collins, K. M. Hudek, J. Mizrahi, J. D. Wong-Campos, S. Allen, J. Apisdorf, P. Solomon, M. Williams, A. M. Ducore, A. Blinov, S. M. Kreikemeier, V. Chaplin, M. Keesan, C. Monroe, and J. Kim. Benchmarking an 11-qubit quantum computer. *Nature Communications*, 10:5464, 2019.

[29] N. Huntemann, C. Sanner, B. Lipphardt, Chr. Tamm, and E. Peik. Single-ion atomic clock with 3×10^{-18} systematic uncertainty. *Phys. Rev. Lett.*, 116:063001, Feb 2016. doi: 10.1103/PhysRevLett.116.063001. URL `https://link.aps.org/doi/10.1103/PhysRevLett.116.063001`.

[30] R. M. Godun, P. B. R. Nisbet-Jones, J. M. Jones, S. A. King, L. A. M. Johnson, H. S. Margolis, K. Szymaniec, S. N. Lea, K. Bongs, and P. Gill. Frequency ratio of two optical clock transitions in $^{171}\mathrm{yb}^{+}$ and constraints on the time variation of fundamental constants. *Phys. Rev. Lett.*, 113: 210801, Nov 2014. doi: 10.1103/PhysRevLett.113.210801. URL `https://link.aps.org/doi/10.1103/PhysRevLett.113.210801`.

[31] N. Huntemann, B. Lipphardt, Chr. Tamm, V. Gerginov, S. Weyers, and E. Peik. Improved limit on a temporal variation of m_p/m_e from comparisons of yb^{+} and cs atomic clocks. *Phys. Rev. Lett.*, 113:210802, Nov 2014. doi: 10.1103/PhysRevLett.113.210802. URL `https://link.aps.org/doi/10.1103/PhysRevLett.113.210802`.

[32] Christian Sanner, Nils Huntemann, Richard Lange, Christian Tamm, and Ekkehard Peik. Autobalanced ramsey spectroscopy. *Phys. Rev. Lett.*, 120: 053602, Jan 2018. doi: 10.1103/PhysRevLett.120.053602. URL `https://link.aps.org/doi/10.1103/PhysRevLett.120.053602`.

[33] K. Beloy and A. Derevianko. Second-order effects on the hyperfine structure of P states of alkali-metal atoms. *Phys. Rev. A*, 78(September): 032519, 2008. doi: 10.1103/PhysRevA.78.032519.

[34] V A Dzuba and V V Flambaum. Hyperfine-induced electric dipole contributions to the electric octupole and magnetic quadrupole atomic clock transitions. *Physical Review A*, 93(5), 2016. ISSN 24699934. doi: 10.1103/PhysRevA.93.052517.

[35] W R Johnson. *Atomic Structure Theory: Lectures on Atomic Physics*. Springer, New York, NY, 2007.

[36] K Beloy, A Derevianko, and W R Johnson. Hyperfine structure of the metastable 3_2^P state of alkaline-earth-metal atoms as an accurate probe of nuclear magnetic octupole moments. *Phys. Rev. A*, 77(1):12512, 1 2008. ISSN 1050-2947. doi: 10.1103/PhysRevA.77.012512. URL `http://link.aps.org/doi/10.1103/PhysRevA.77.012512`.

[37] M J Petrasiunas, E W Streed, T J Weinhold, B G Norton, and D Kielpinski. Optogalvanic spectroscopy of metastable states in Yb^+. *Applied Physics B*, 107(4):1053–1059, 6 2012. ISSN 0946-2171. doi: 10.1007/s00340-011-4791-x. URL `http://link.springer.com/10.1007/s00340-011-4791-x`.

[38] P Taylor, M Roberts, and GM Macfarlane. Measurement of the infrared $^2F_{7/2} -^2 D_{5/2}$ transition in a single $^{171}Yb^+$ ion. *Physical Review A*, 83(1): 013406, 1999. ISSN 1050-2947. doi: 10.1103/PhysRevA.83.013406.

[39] Ya. B Zel'dovich. Parity Nonconservation in the First Order in the Weak-Interaction Constant in Electron Scattering and Other Effects. *Journal of Experimental and Theoretical Physics (JETP)*, 36:964–966, 1959.

[40] M A Bouchiat and C Bouchiat. Parity violation induced by weak neutral currents in atomic physics. I. *J. Phys.*, 35(12):899–927, 1974.

[41] L M Barkov and M S Zolotorev. Observation of parity nonconservation in atomic transitions. *Pis'ma v ZhETF*, 27:379–383, 1978.

[42] M.C. Noecker, B.P. Masterson, and C.E. Wieman. Precision Measurement of Parity Nonconservation in Atomic Cesium: A Low-Energy Test of the Electroweak Theory. *Phys. Rev. Lett.*, 61(3):310–313, 1988. doi: 10.1103/PhysRevLett.61.310. URL `https://link.aps.org/doi/10.1103/PhysRevLett.61.310`.

[43] C. S. Wood, S. C. Bennett, D. Cho, B. P. Masterson, J. L. Roberts, Carol E. Tanner, C. E. Wieman, Vladislav Gerginov, Andrei Derevianko, and Carol E. Tanner. Observation of the nuclear magnetic octupole moment of ^{133}Cs. *Phys. Rev. Lett.*, 275(5307):1759–1763, 8 2003. ISSN 00368075. doi: 10.1103/PhysRevLett.91.072501.

[44] M S Safronova, D Budker, D DeMille, Derek F Jackson Kimball, A Derevianko, and Charles W Clark. Search for new physics with atoms and molecules. *Rev. Mod. Phys.*, 90(2):25008, 6 2018. ISSN 0034-6861. doi: 10.1103/RevModPhys.90.025008. URL `http://arxiv.org/abs/1710.01833https://link.aps.org/doi/10.1103/RevModPhys.90.025008`.

[45] W. Johnson, M. Safronova, and U. Safronova. Combined effect of coherent Z exchange and the hyperfine interaction in the atomic parity-nonconserving interaction. *Phys. Rev. A*, 67(6):062106, jun 2003. ISSN 1050-2947. doi: 10.1103/PhysRevA.67.062106. URL `http://link.aps.org/doi/10.1103/PhysRevA.67.062106`.

[46] C. S. Wood, S. C. Bennett, J. L. Roberts, D. Cho, and C. E. Wieman. Precision measurement of parity nonconservation in cesium. *Canadian Journal of Physics*, 77(1):7–75, 1999. ISSN 00084204. doi: 10.1139/p99-002.

[47] W. C. Haxton and C. E. Wieman. Atomic Parity Nonconservation and Nuclear Anapole Moments. *Ann. Rev. Nucl. Part. Sci.*, 51:261, 2001.

[48] Bertrand Desplanques, John F Donoghue, and Barry R Holstein. Unified treatment of the parity violating nuclear force. *Annals of Physics*, 124(2):449–495, 1980. ISSN 0003-4916. doi: https://doi.org/10.1016/0003-4916(80)90217-1. URL `https://www.sciencedirect.com/science/article/pii/0003491680902171`.

[49] Wick C. Haxton and Barry R. Holstein. Hadronic parity violation. *Prog. Part. Nucl. Phys.*, 71:185–203, 2013. ISSN 01466410. doi: 10.1016/j.ppnp.2013.03.009.

[50] V A Dzuba, V V Flambaum, K Beloy, and A Derevianko. Hyperfine-mediated static polarizabilities of monovalent atoms and ions. *Phys. Rev. A*, 82(6):62513, 12 2010. ISSN 1050-2947. doi: 10.1103/PhysRevA.82.062513. URL `http://link.aps.org/doi/10.1103/PhysRevA.82.062513`.

[51] Kyle Beloy. Theory of the ac stark effect on the atomic hyperfine structure and applications to microwave atomic clocks. *Ph.D. Disseration*, 2009.

[52] R G Garstang. Hyperfine structure and intercombination line intensities in the spectra of Magnesium, Zinc, Cadmium, and Mercury. *J. Opt. Soc. Am.*, 52(8):845, 1962.

[53] W.R. R. Johnson. Hyperfine quenching: review of experiment and theory. *Can. J. Phys.*, 89(4):429–437, apr 2011. ISSN 0008-4204. doi: 10.1139/p11-018. URL `http://dx.doi.org/10.1139/p11-018`.

[54] Sergey G Porsev and Andrei Derevianko. Hyperfine quenching of the metastable $^3P_{0,2}$ states in divalent atoms. *Phys. Rev. A*, 69(4):42506, 2004.

[55] S. G. Porsev and V. V. Flambaum. Effect of atomic electrons on the 7.6-eV nuclear transition in $^{229}Th^{3+}$. *Phys. Rev. A*, 81(3):032504, mar 2010. ISSN 1050-2947. doi: 10.1103/PhysRevA.81.032504. URL `http://link.aps.org/doi/10.1103/PhysRevA.81.032504`.

[56] K Beloy, U I Safronova, and A Derevianko. High-Accuracy Calculation of the Blackbody Radiation Shift in the ^{133}Cs Primary Frequency Standard. *Phys. Rev. Lett.*, 97(4):40801, 2006.

[57] E. J. Angstmann, V. A. Dzuba, and V. V. Flambaum. No Title, 2006.

[58] R. Chicireanu, K.∼D. Nelson, S. Olmschenk, N. Lundblad, A. Derevianko, and J.∼V. Porto. Differential Light Shift Cancellation in a Magnetic-Field-Insensitive Transition of ^{87}Rb. *Phys. Rev. Lett.*, 106(6):063002, oct 2011. ISSN 0031-9007. doi: 10.1103/PhysRevLett.106.063002.

[59] Andrei Derevianko. Hyperfine-induced quadrupole moments of alkali-metal-atom ground states and their implications for atomic clocks. *Phys. Rev. A*, 93(1):012503, jan 2016. ISSN 2469-9926. doi: 10.1103/PhysRevA.93.012503. URL `https://link.aps.org/doi/10.1103/PhysRevA.93.012503`.

[60] S C Bennett and C E Wieman. Measurement of the $6S - 7S$ Transition Polarizability in Atomic Cesium and an Improved Test of the Standard Model. *Phys. Rev. Lett.*, 82:2484–2487, 1999.

[61] D Cho, C S Wood, S C Bennett, J L Roberts, and C E Wieman. Precision measurement of the ratio of scalar to tensor transition polarizabilities for the cesium 6S-7S transition. *Physical Review A*, 55, 2, 1997.

[62] D. A. Varshalovich, A. N. Moskalev, and V. K. Khersonskii. *Quantum Theory of Angular Momentum*. World Scientific, Singapore, 1988.

[63] W. R. Johnson, S. A. Blundell, and J. Sapirstein. Finite basis sets for the dirac equation constructed from b splines. *Phys. Rev. A*, 37:307–315, Jan 1988. doi: 10.1103/PhysRevA.37.307. URL https://link.aps.org/doi/10.1103/PhysRevA.37.307.

[64] J Sapirstein and WR Johnson. The use of basis splines in theoretical atomic physics. , 29:5213, 1996.

[65] Kyle Beloy and Andrei Derevianko. Application of the dual-kinetic-balance sets in the relativistic many-body problem of atomic structure. *Computer physics communications*, 179(5):310–319, 2008. ISSN 0010-4655.

[66] M.Y. Amusia. *Atomic Photoeffect*. Physics of Atoms and Molecules. Springer US, 1990. ISBN 9780306435485. URL https://books.google.com/books?id=8yY6UMG2puwC.

[67] W.R. Johnson. Relativistic random-phase approximation. volume 25 of *Advances in Atomic and Molecular Physics*, pages 375–391. Academic Press, 1989. doi: https://doi.org/10.1016/S0065-2199(08)60094-9. URL https://www.sciencedirect.com/science/article/pii/S0065219908600949.

[68] W R Johnson, Z W Liu, and J Sapirstein. Transition rates for lithium-like ions, sodium-like ions, and neutral alkali-metal atoms. *At. Data Nucl. Data Tables*, 64(2):279–300, 1996.

[69] V A Dzuba, V V Flambaum, and O P Sushkov. No Title. *J. Phys. B*, 17: 1953, 1984.

[70] {NIST} Atomic Spectra Database. URL http://physics.nist.gov/cgi-bin/AtData/main_asd.

[71] George Toh, Jose A. Jaramillo-Villegas, Nathan Glotzbach, Jonah Quirk, Ian C. Stevenson, J. Choi, Andrew M. Weiner, and D. S. Elliott. Measurement of the lifetime of the $7s^2 s_{1/2}$ state in atomic cesium using asynchronous gated detection. *Phys. Rev. A*, 97:052507, May 2018. doi: 10.1103/PhysRevA.97.052507. URL https://link.aps.org/doi/10.1103/PhysRevA.97.052507.

[72] George Toh, Amy Damitz, Nathan Glotzbach, Jonah Quirk, I. C. Stevenson, J. Choi, M. S. Safronova, and D. S. Elliott. Electric dipole matrix elements for the $6p\,^2P_J \rightarrow 7s\,^2S_{1/2}$ transition in atomic cesium. *Phys.*

Rev. A, 99:032504, Mar 2019. doi: 10.1103/PhysRevA.99.032504. URL https://link.aps.org/doi/10.1103/PhysRevA.99.032504.

[73] C. E. Tanner, A. E. Livingston, R. J. Rafac, F. G. Serpa, K. W. Kukla, H. G. Berry, L. Young, and C. A. Kurtz. Measurement of the $6p^2p_{3/2}$ state lifetime in atomic cesium. *Phys. Rev. Lett.*, 69:2765–2767, Nov 1992. doi: 10.1103/PhysRevLett.69.2765. URL https://link.aps.org/doi/10.1103/PhysRevLett.69.2765.

[74] L. Young, W. T. Hill, S. J. Sibener, Stephen D. Price, C. E. Tanner, C. E. Wieman, and Stephen R. Leone. Precision lifetime measurements of cs $6p^2p_{1/2}$ and $6p^2p_{3/2}$ levels by single-photon counting. *Phys. Rev. A*, 50:2174–2181, Sep 1994. doi: 10.1103/PhysRevA.50.2174. URL https://link.aps.org/doi/10.1103/PhysRevA.50.2174.

[75] Robert J. Rafac and Carol E. Tanner. Measurement of the ratio of the cesium d-line transition strengths. *Phys. Rev. A*, 58:1087–1097, Aug 1998. doi: 10.1103/PhysRevA.58.1087. URL https://link.aps.org/doi/10.1103/PhysRevA.58.1087.

[76] Robert J. Rafac, Carol E. Tanner, A. Eugene Livingston, and H. Gordon Berry. Fast-beam laser lifetime measurements of the cesium $6p^2P_{1/2,3/2}$ states. *Phys. Rev. A*, 60:3648–3662, Nov 1999. doi: 10.1103/PhysRevA.60.3648. URL https://link.aps.org/doi/10.1103/PhysRevA.60.3648.

[77] Andrei Derevianko and Sergey G. Porsev. Determination of lifetimes of $6P_J$ levels and ground-state polarizability of Cs from the van der waals coefficient C_6. *Phys. Rev. A*, 65:053403, Apr 2002. doi: 10.1103/PhysRevA.65.053403. URL https://link.aps.org/doi/10.1103/PhysRevA.65.053403.

[78] Jason M. Amini and Harvey Gould. High precision measurement of the static dipole polarizability of cesium. *Phys. Rev. Lett.*, 91:153001, Oct 2003. doi: 10.1103/PhysRevLett.91.153001. URL https://link.aps.org/doi/10.1103/PhysRevLett.91.153001.

[79] Nadia Bouloufa, Anne Crubellier, and Olivier Dulieu. Reexamination of the 0_g^- pure long-range state of Cs_2: Prediction of missing levels in the photoassociation spectrum. *Phys. Rev. A*, 75:052501, May 2007. doi: 10.1103/PhysRevA.75.052501. URL https://link.aps.org/doi/10.1103/PhysRevA.75.052501.

[80] J. F. Sell, B. M. Patterson, T. Ehrenreich, G. Brooke, J. Scoville, and R. J. Knize. Lifetime measurement of the cesium $6P_{3/2}$ state using ultrafast laser-pulse excitation and ionization. *Phys. Rev. A*, 84:010501, Jul 2011. doi: 10.1103/PhysRevA.84.010501. URL https://link.aps.org/doi/10.1103/PhysRevA.84.010501.

[81] Yichi Zhang, Jie Ma, Jizhou Wu, Lirong Wang, Liantuan Xiao, and Suotang Jia. Experimental observation of the lowest levels in the photoassociation spectroscopy of the 0_g^- purely-long-range state of Cs_2. *Phys. Rev. A*, 87:030503, Mar 2013. doi: 10.1103/PhysRevA.87.030503. URL https://link.aps.org/doi/10.1103/PhysRevA.87.030503.

[82] B. M. Patterson, J. F. Sell, T. Ehrenreich, M. A. Gearba, G. M. Brooke, J. Scoville, and R. J. Knize. Lifetime measurement of the cesium $6P_{3/2}$ level using ultrafast pump-probe laser pulses. *Phys. Rev. A*, 91:012506, Jan 2015. doi: 10.1103/PhysRevA.91.012506. URL https://link.aps.org/doi/10.1103/PhysRevA.91.012506.

[83] Maxwell D. Gregoire, Ivan Hromada, William F. Holmgren, Raisa Trubko, and Alexander D. Cronin. Measurements of the ground-state polarizabilities of cs, rb, and k using atom interferometry. *Phys. Rev. A*, 92: 052513, Nov 2015. doi: 10.1103/PhysRevA.92.052513. URL https://link.aps.org/doi/10.1103/PhysRevA.92.052513.

[84] Amy Damitz, George Toh, Eric Putney, Carol E. Tanner, and D. S. Elliott. Measurement of the radial matrix elements for the $6s\,^2s_{1/2} \rightarrow 7p\,^2p_J$ transitions in cesium. *Phys. Rev. A*, 99:062510, Jun 2019. doi: 10.1103/PhysRevA.99.062510. URL https://link.aps.org/doi/10.1103/PhysRevA.99.062510.

[85] S. Bennett and C. Wieman. Erratum: Measurement of the 6S $\rightarrow$7S Transition Polarizability in Atomic Cesium and an Improved Test of the Standard Model [Phys. Rev. Lett. 82, 2484 (1999)]. *Phys. Rev. Lett.*, 83(4): 889–889, jul 1999. ISSN 0031-9007. doi: 10.1103/PhysRevLett.83.889. URL http://link.aps.org/doi/10.1103/PhysRevLett.83.889.

[86] J. J. Boyle and M. S. Pindzola. *Many-Body Atomic Physics*. Cambridge University Press, 8 1998. ISBN 9780521470063. doi: 10.1017/CBO9780511470790. URL https://www.cambridge.org/core/product/identifier/9780511470790/type/book.

[87] P. Rosenbusch, S. Ghezali, V. A Dzuba, V. V Flambaum, K. Beloy, and A. Derevianko. ac Stark shift of the Cs microwave atomic clock tran-

sitions. *Phys. Rev. A*, 79(1):13404, jan 2009. ISSN 1050-2947. doi: 10.1103/PhysRevA.79.013404.

[88] Dipankar Das and Vasant Natarajan. High-precision measurement of hyperfine structure in the D lines of alkali atoms. *J. Phys. B*, 41(3):35001, 2008.

[89] G Belin, L Holmgren, and S Svanberg. Hyperfine interaction, zeeman and stark effects for excited states in cesium. *Physica Scripta*, 14(1-2):39, jul 1976. doi: 10.1088/0031-8949/14/1-2/008. URL https://dx.doi.org/10.1088/0031-8949/14/1-2/008.

[90] E. Arimondo, M. Inguscio, and P. Violino. Experimental determinations of the hyperfine structure in the alkali atoms. *Rev. Mod. Phys.*, 49:31–75, Jan 1977. doi: 10.1103/RevModPhys.49.31. URL https://link.aps.org/doi/10.1103/RevModPhys.49.31.

[91] M. Auzinsh, K. Bluss, R. Ferber, F. Gahbauer, A. Jarmola, M. S. Safronova, U. I. Safronova, and M. Tamanis. Level-crossing spectroscopy of the 7, 9, and $10D_{52}$ states of ^{133}Cs and validation of relativistic many-body calculations of the polarizabilities and hyperfine constants. *Phys. Rev. A*, 75:022502, Feb 2007. doi: 10.1103/PhysRevA.75.022502. URL https://link.aps.org/doi/10.1103/PhysRevA.75.022502.

[92] A. Derevianko, M. S Safronova, and W. R Johnson. Ab initio calculations of off-diagonal hyperfine interaction in cesium. *Phys. Rev. A*, 60(3): R1741–R1742, sep 1999. ISSN 1050-2947. doi: 10.1103/PhysRevA.60.R1741.

[93] I. Lindgren and J. Morrison. *Atomic many-body theory*. Springer series on atoms + plasmas. Springer, 1986. ISBN 9783540166498. URL https://books.google.com/books?id=aQjwAAAAMAAJ.